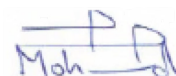Federal State Autonomous Educational Institution of Higher Education

«PEOPLES' FRIENDSHIP UNIVERSITY OF RUSSIA»

(RUDN)

Federal State Budgetary Institution of Science

«Institute of Organic Chemistry. N. D. Zelinsky,

Russian Academy of Sciences» (IOC RAS)

As a manuscript

Osman Mohamed Ezeldin Abdalla

THE ROLE OF CARBON AND NANOCOMPOSITE HYBRID MATERIALS AS A SUPPORT FOR TRANSITION METAL SULFIDE-BASED CATALYSTS IN HIGHER ALCOHOLS SYNTHESIS FROM SYNGAS

Specialty

1.4. 4. Physical chemistry

1.4.14. Kinetics and Catalysis

THESIS

For a PHD degree in chemical sciences

Scientific Supervisors:

Sheshko Tatiana Fedorovna
Associate Professor (PhD)

Kogan Victor Mironovich
Prof., D. Sc. in Chemistry (Catalysis)

Moscow 2022

Федеральное государственное автономное образовательное учреждение высшего образования
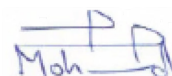
"РОССИЙСКИЙ УНИВЕРСИТЕТ ДРУЖБЫ НАРОДОВ"

(РУДН)

Федеральное государственное бюджетное учреждение науки

"ИНСТИТУТ ОРГАНИЧЕСКОЙ ХИМИИ ИМ. Н.Д. ЗЕЛИНСКОГО

РОССИЙСКОЙ АКАДЕМИИ НАУК" (ИОХ РАН)

На правах рукописи

Осман Мохамед Изелдин Абдалла

РОЛЬ УГЛЕРОДА И НАНОКОМПОЗИТНЫХ ГИБРИДНЫХ МАТЕРИАЛОВ В КАЧЕСТВЕ НОСИТЕЛЕЙ ДЛЯ КАТАЛИЗАТОРОВ НА ОСНОВЕ СУЛЬФИДОВ ПЕРЕХОДНЫХ МЕТАЛЛОВ В СИНТЕЗЕ ВЫСШИХ СПИРТОВ ИЗ СИНТЕЗ-ГАЗА

Специальность

1.4. 4. Физическая химия

1.4.14. Кинетика и катализ

ДИССЕРТАЦИЯ

на соискание ученой степени

кандидата химических наук

Научные руководители:

Шешко Татьяна Федоровна
Кандидат химических наук, доцент

Коган Виктор Миронович
Доктор химических наук, профессор

МОСКВА – 2022

TABLE OF CONTENTS

INTRODUCTION

Relevance of the research topic

Conversion of biomass- or coal-based syngas to higher alcohols by using the carbon monoxide hydrogenation process is estimated as one of the alternative routes to produce fuels and fuel additives. HA are employed as octane performance enhancers or directly as liquid fuel for internal combustion engines (ICE) [1] and have the possibility to substitute other hazardous compounds used as octane number improvers in ICE fuel.[2] In this sense, the utilization of these alcohols as components of alternative fuel systems or alternative fuels directly addresses greenhouse gas emissions, toxicity, and other global climate challenges. Catalytic systems for the higher alcohols synthesis commonly rely on molybdenum disulfide because of its high activity and high sulfur tolerance for the water-gas shift reaction (WGS). [3-4] Other catalytic systems are prone to sulfur poisoning, which is a major issue when employing sulfur-rich syngas from biomass or coal. In addition to being resistant to sulfur poisoning, [5] the MoS_2-based catalytic system may produce large amounts of C_{1+} - C_{5+} alcohols when modified by alkali metals and promoted by group VIII metals (Co, Ni, Fe, Rh). [6-8]

Promoted and modified MoS_2 catalysts supported on carbon materials have higher catalytic activity than those based on metal oxides (Al_2O_3, SiO_2, MgO, ZrO_2) according to several publications. [9-11] Amajority of these studies interpret the activity of carbon materials as a result of weak interaction between carbon and the K-CoMoS active phase, as well as of low acidity compared to metal oxides, which has a positive effect on the selectivity towards alcohols. In literature, higher alcohols are alcohols that have more than two carbon atoms.[4]

TMS-based catalysts with high activity and selectivity can be synthesized using a variety of supports that affect the morphology, electron properties, and dispersion of the formed active phase. In fine chemical industry, activated carbons (AC) are broadly used as a catalyst support due to their specific properties, such as high stability at high reaction pressures and temperatures, [13-15] a larger surface area and

porosity, resistance to acidic and basic conditions, and minimal interaction between the support material and active phase. [16-17] In addition, because of the delocalized π electronics, electronic conductivity is an important property of AC. [18] Normal activated carbons, being microporous (<2nm), cause pore plugging due to the formation of coke and deactivation of the sulfided catalyst, which results in the transport limitation during the catalytic reaction. [19] Internal diffusion issues can be avoided by using mesoporous supports with pore diameters ranging from 2–50 nm. A majority of HAS research has been conducted using microporous AC supported catalysts with significantly smaller surface areas (350–820 m^2 g^{-1}) than commercially available activated carbons (950 m^2 g^{-1} and higher), and long-term activity of these supported catalysts does not meet commercial levels. The support's textural properties, such as pore volume, surface area, and average pore diameter, can significant influence the extent of adsorption, morphology, reduction and selectivity properties of the active phase. [20]

Degree of development of the research topic

Several catalytic systems for the higher alcohols synthesis (HAS) from syngas are known, from which the most promising are those based on MoS_2 promoted by cobalt or nickel and modified with alkali metals. [21-24] Syngas conversion on unpromoted MoS_2 yields mainly hydrocarbons, whereas MoS_2 modified with potassium and heavier alkali metals give mainly alcohols. The second transition metal deactivates the sulfur-edge but promotes activity of the M-edge resulting in the increased selectivity towards alcohols. [25] Modification with alkali metals causes a decrease in the number of MoS_2 slabs, which in turn leads to an increase in the catalyst affinity for sulfur and a decrease in Lewis acidity, preventing hydrogenation and hydrodeoxygenation.[6]

The most important properties of active carbons (AC) as catalyst supports compared to oxide supports (Al_2O_3, SiO_2, TiO_4…etc.) are facile recovery of the active metal by combustion of the carbon support, neutral nature (no strong acidic or basic sites), and cost efficiency. [25] Several studies examined the effect of textural characteristics of supports on the active phase of K-modified CoMoS and on catalytic

performance in HAS. Some of these studies experimented with microporous materials such as metal oxides and multi-walled carbon nanotubes (MWCNT), while others utilized microporous activated carbons. [4]

Overall goal

- **General Objectives**

  ➤ To study the influence of textural characteristics of supports and catalysts on catalytic performance of supported-K-CoMoS$_2$ catalysts for higher alcohol synthesis from synthesis gas.

  ➤ To integrate beneficial characteristics of Al$_2$O$_3$ and carbon by using carbon coated alumina (prepared by pyrolysis) as a support for higher alcohol synthesis from synthesis gas over K-modified CoMoS$_2$ catalysts.

  ➤ To develop the catalytic activity of K-modified CoMoS$_2$/Al$_2$O$_3$ by coating alumina using graphene nanosheets for higher alcohol synthesis.

  ➤ To enhance selectivity of higher alcohols over K-modified CoMoS$_2$ catalysts by using several types of novel powder and fiber commercial activated carbons supports prepared from natural sources.

  ➤ To study effects of distribution of the active phase inside of support pores, catalysts acidity, as well as of the particles size and length of catalysts on catalytic activity of K-modified CoMoS$_2$ catalysts for higher alcohol synthesis from synthesis gas.

- **Specific objectives**

  ➤ To coat γ-Al$_2$O$_3$ by carbon and graphene nanosheets with a thickness of 5-7 nm with a view to integrate the beneficial properties of Al$_2$O$_3$ and carbon in one support (CCA).

  ➤ To characterize the supported K-CoMoS$_2$ catalysts using N$_2$ adsorption and desorption isotherms, X-ray fluorescence technique, field-emission

scanning electron microscopy (FE-SEM), energy dispersive x-ray technique (EDX), transmission electron microscopy technique (TEM), and X-ray Photoelectron Spectroscopy (XPS)

➢ To study catalytic activity of supported sulfided catalysts in higher alcohols synthesis from synthesis gas using a fixed-bed flow reactor catalytic system under optimum conditions.

➢ To compare the obtained results aiming at raising the selectivity of higher alcohols to be used in internal combustion engines as a fuel or as octane number improvers.

Scientific novelty

The beneficial characteristics of Al_2O_3 and carbon (mesoporous carbon prepared by pyrolysis and graphene) have been integrated. Carbon mesoporous materials were used as a support for HAS from syngas over K-CoMoS$_2$ catalysts. The first use of nanostructured graphene-coated alumina as a support for K-CoMoS$_2$ catalysts to produce higher alcohols from syngas has been reported. The effect of different carbon-containing materials, used as supports for transition metal sulfide (TMS) based catalysts, on catalytic properties for synthesis gas conversion to alcohols has been studied.

The most essential finding of this study is an unusual correlation between catalytic activity and the micro- and mesopore structure of the catalyst support. It was found that catalysts supported on microporous materials possessed higher catalytic activity in HAS synthesis from syngas than those supported on mesoporous materials. We explained this phenomenon by the combined effect of catalyst acidity and distribution of the active phase inside the pores. Catalysts containing large agglomerates of the MoS_2-based active phase supported on less acidic materials exhibit higher activity than catalysts supported on more acidic mesopore structured materials due to the differences in active phase-support interactions.

In order to increase the selectivity of higher alcohols synthesis from syngas over K-modified $CoMoS_2$ catalysts, the role of novel powder and fiber ACs as supports for HAS from syngas over K-modified $CoMoS_2$ catalysts has been studied. Fiber ACs have shown a filamentous morphology with a strip axial arrangement and a few longitudinal grooves with many irregular particles distributed on the fiber surfaces, thus leading to tangled MoS_2 slabs with the highest CO conversion and alcohols yield.

Theoretical and practical significance

This work makes a certain contribution to both applied and basic research aimed at creating suitable supported $K-CoMoS_2$ catalytic systems that are stable and selective for production of higher alcohols from syngas. A detailed analysis of the obtained experimental data showed the rationality of integrating the beneficial characteristics of alumina and graphene and using the synthesized graphene coated alumina as a support for HAS from syngas over $K-CoMoS_2$ catalysts. The established correlations between textural characteristics and catalytic performance can be utilized for furthering research focused on the improvement of catalysts for HAS systems. The results obtained for catalytic activity confirm the promise of using such systems in large scale processes. The work was carried out in accordance with the work plan of the Department of Physical and Colloidal Chemistry, RUDN, in cooperation with the Laboratory for Catalysis by Transition Metal Sulfide Catalysts at the Zelinsky Institute of Organic Chemistry of RAS.

Methodology and research methods

Studies on catalytic activity of supported sulfided catalysts in the higher alcohols synthesis from synthesis gas were carried out on a fixed-bed flow reactor. The gaseous products were analyzed using a LHM-80 GC with a Thermal Conductivity Detector (TCD) and two one-meter packed columns (molecular sieves CaA (Ar, CH4, CO) and Porapak Q (CO_2, C_{2+})); the liquid products were analyzed using a Crystal-2000M GC with a flame ionization detector (FID) and a 50 m HP-FFAP capillary column. Quantachrome Nova 1200e at 77 K and N_2 adsorption and desorption

isotherms techniques were used to study the support and catalyst textural characteristics. The analytical method of UV spectrometry of pyridine adsorption was used to determine the acid-base properties of the supports and sulfided catalysts. A Shimadzu EDX-7000 X-ray fluorescence spectrometer was used to analyze the elementary composition of the sulfided catalysts. A scanning electron microscope (SEM) was used to demonstrate the surface morphology of the supports and sulfided catalysts. A transmission electron microscope (TEM) was used with two different LaB6 cathodes, one with an accelerating voltage of 200 kV and the other of 300-kV (FEI Company, USA) to characterize the morphology of the sulfided catalysts. X-ray photoelectron spectroscopy (XPS) was employed to evaluate the chemical species present on the surface of the K-CoMoS$_2$ supported catalysts.

Summarized statements of the thesis for the defense

- Results of the catalytic tests of supported K-modified CoMoS$_2$ catalysts in relation to higher alcohols synthesis from syngas; investigation of the influence of different types of carbon containing materials on catalytic performance.
- Results of improving K-modified CoMoS$_2$/Al$_2$O$_3$ catalytic activity by coating alumina with carbon and graphene nanosheets in the higher alcohol synthesis from syngas.
- Results of the catalytic performance of the K-modified CoMoS$_2$ catalyst supported on novel fiber and powder activated carbons in the higher alcohols synthesis from syngas.
- Evolution of the effect of textural characteristics of supports and sulfided catalysts' on the catalytic performances.

Reliability

The accuracy and reliability of the results are guaranteed by the use of modern analytical methods and state-of-the-art instruments available with the Peoples' Friendship University of Russia and Zelinsky Institute of Organic Chemistry of the

Russian Academy of Sciences. Also, the reproducibility of the results and their uniformity with each other, as well as with the literature reviews ensure the reliability of the results.

Author's personal contribution

The author actively participated in writing of the research proposal and planning of the experiments, particularly in the collection and analysis of the appropriate literature on the research topic. The author independently conducted all catalytic tests, analyzed the reaction products by GC methods, took active part in the discussion of the obtained results, such as physicochemical and catalytic characteristics of the samples, and in their presentation and interpretation. The author prepared the thesis, contributed at most to the publications, and presented the abstracts at the international conferences.

Approbation of the work

The obtained results of the current study within the framework of the dissertation research were presented and discussed at a few international scientific conferences: 6th International Conference on Chemical Materials and Process (ICCMP 2020), Warsaw, Poland, July 2-4, 2020, (online); 1st International Electronic Conference on Catalysis Sciences, MDPI, USA, November 10-30, 2020, (online); 7th Edition of International Conference on Catalysis, Chemical Engineering and Technology–2021 (CCT 2021), Tokyo, May 17 – 18, 2021, (online); Catalysis for a Sustainable World Conference, RUDN, December 22-24, 2020; 11th Edition of the International Conference on Catalysis, Chemical Engineering and Technology, Japan, May 16-17, 2022, (online). 12th Russian Conference (with international participation): Actual Problems of Petrochemistry, Moscow, Russia, 2021. The Sixth International Scientific Conference "Advances in Synthesis and Complexing". RUDN University, September 26-30, 2022.

Completeness of the materials presentation

Based on the research results within the structure and scope of the dissertation, 15 printed works were published, including 4 in the journals indexed in the Scopus and WoS databases, and 11 abstracts in the collections of international scientific conferences, three of which are indexed in the RSCI.

Structure and scope of the dissertation

The thesis consists of the table of contents, lists of tables (17), figures (57) and abbreviations, the introduction, literature review, materials and methods, results and discussion, conclusion, recommendations, research outcomes, and references. The dissertation material is presented on 138 pages. The list of literary sources includes 165 references.

1. LITERATURE REVIEW

1.1. Background

For the last decades, the demand for renewable energy has been increasing intensively due to the crude-oil squeeze and the alert of global warming. Between the alternatives for fossil fuels to generate heat, biomass is considered as an abundant neutral carbon source, of which its conversion to heat does not bar the balance of the atmosphere's air contents. Energy sources, security, and alternative energy are considered as the most important obstacles confronting humanity as population numbers increase. In addition, it is necessary to reduce injurious environmental impacts related to the energy generation to help save our planet.[26] The need for energy has dramatically risen and it is rapidly increasing. Air emission in 2008 was evaluated as 150 x 1012 W with 87% from combustion and burning of fossil fuels (radioactive elements, natural gas, crude oil, or coal).[27] The manufacturing sector (mining, construction, agriculture, and industrialization) accounts for about 38 % of energy consumption.[28] The transportation section is the second-largest consumer, (about 21% of total energy consumption). Petro-fuels are considered the main source of transportation fuels.[29] It was expected that global energy consumption will rise by 55% from 1998 to 2020, which is almost 20% of the overall energy consumed.[30] The energy resources which can be replaced without harming the environment and are not depleted when used are known as renewable energy which is produced from natural resources such as biomass, tides, wind, sunlight, etc.[31] Recently, renewable energy resources have become one of the most important alternatives that reduce the exhausting of fossil energy reserves. Since the last century, a 14% of energy in the world is produced from alternative and renewable sources, most of it results from the biomass conversion into energy.[32]

1.1.1. Biomass

The accurate definition of biomass is the mass of biological organisms in an ecosystem or area at a particular time, such as animal or plant matter using for the

production of chemicals, fibres, energy, etc.[33] It contains lignin, cellulose, hemi-cellulose, and a small amount of other materials.[34] It usually is in liquid or solid state and formed of hydrogen, oxygen, co-polymer of carbon and includes small amounts of inorganic elements, sulfur, and nitrogen.[35] Moreover, there are some other sources of biomass such as: agricultural product residues, wood from fire- and insect-killed forest stands, dung from ranch livestock processes, sheathes derived from cellulose, pulping alcohol-liquors, refined-cook oils, natural rubber products, coffee molds, remains of agricultural harvests, waste of wood manufacturing, waste residues from incineration or landfill, and forest harvesting residues.[36-37]

1.1.2. Renewable energy resources and biomass availability in Russia

Although Russia is among the largest oil-producing countries, it can be classified as the developer of alternative and renewable energy sources due to the large area suitable for cultivation, as well as the state's policy in this sector, which seems more attractive to investors.[38] The availability depends on a number of technological, economic, regulatory, and environmental factors like the type of biomass, transport costs, production costs, and the utilized conversion technology, which in turnover set the desired biomass resource, contest with other markets and rate bands, and governments policy with regard to, for example, energy crop, waste processing, and production.[39] The important key success factor of an essential future role for biofuels (especially biogas) in Russia is the availability of biomass. Biomass is a type of renewable, eco-friendly, clean energy, and abundant. Bioenergy is one of the most promising sectors of the economy is already developing in some regions of Russia. The expediency of development in this industry caused by the presence of decentralized energy supply zones, waste management needs, necessity and expediency of energy sector upgrading.[40] Like any other branch of power supply, bioenergy needs reliable resource assessments and projections. In Russia, detailed assessments of biomass energy potential earlier were carried out only on a national scale.[41] In 2015, within the framework of

developing geographic information system "Renewable Energy Sources of Russia" data on the different types of wastes used for bioenergy was collected, the calculations of gross, technical and economic bioenergy potentials were made, databases and maps of the resource distribution were developed for the territory Russia. For today resources of sewage sludge, municipal solid wastes, the main areas of animal husbandry wastes, the main cultivated agricultural crops of Russia: grains (with a separate species), oilseeds, vegetables and potatoes – were analyzed for each region of the Russian Federation.[42] Scientifically based quantitative evaluations and convenience of it is visual display as maps allow to highlight the lead in biomass potential regions. With the socio-economic and environmental features of the territory it forms the basis for decision making. These estimates are used by public authorities for planning strategy of national energy development.[42]

In 2015, Russia has ranked as the fifth-largest hydroelectricity producer country, where hydropower occupied approximately 15% of total electricity generation.[42] Moreover, the percentage of renewable energy was small with the exception of large hydropower. According to British Petroleum (BP) estimates, it reached about 0.05% of the total electricity generation in 2015 (Fig. 1.1).
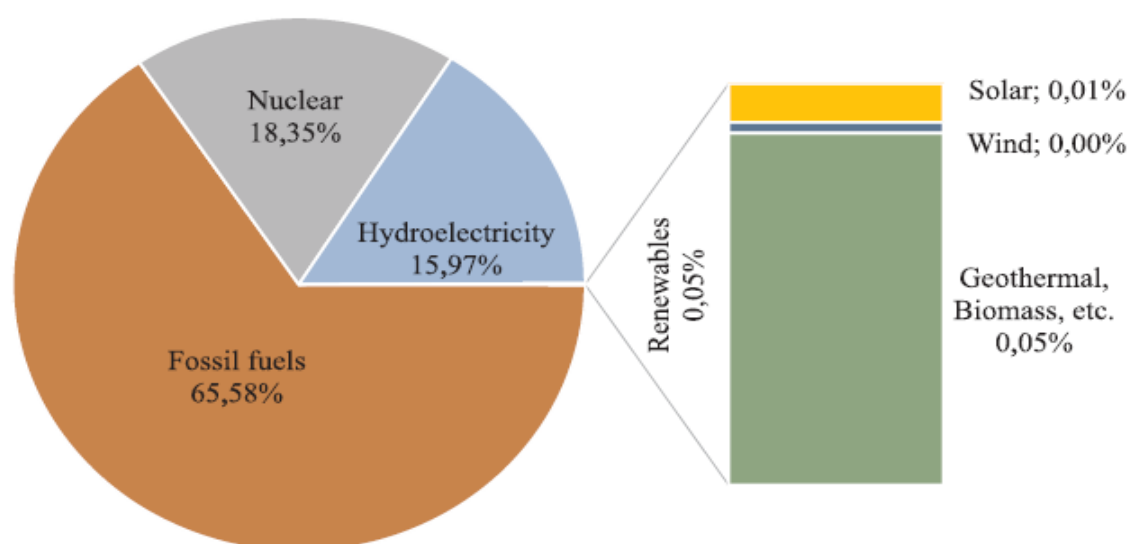

Figure 1.1. Energy sources for electricity generation in Russia, 2015.[43]

The estimates of Russian organizations are more hopeful, but not dramatically according to the statistics service of the Russian Federation (Rosstat). However, renewable energies (except hydropower, which is more than 25 MW of set up capacity) accounted for 0.19% of the whole electricity generation in 2015.[44]

According to the statistics from 2010, if bioenergy is used to the fullest, it may be equal to 30% of the total electricity and heat consumption in Russia.[45] Recently, electricity and heat demand can be satisfied in almost all areas in the Northern and South-Caucasian federal regions. In these districts, bioenergy potential coincides with 100% of the total heat and electricity consumption, which can be demonstrated by high bioenergy resources of these districts with a moderate climate and improved agriculture (Fig. 1. 2).
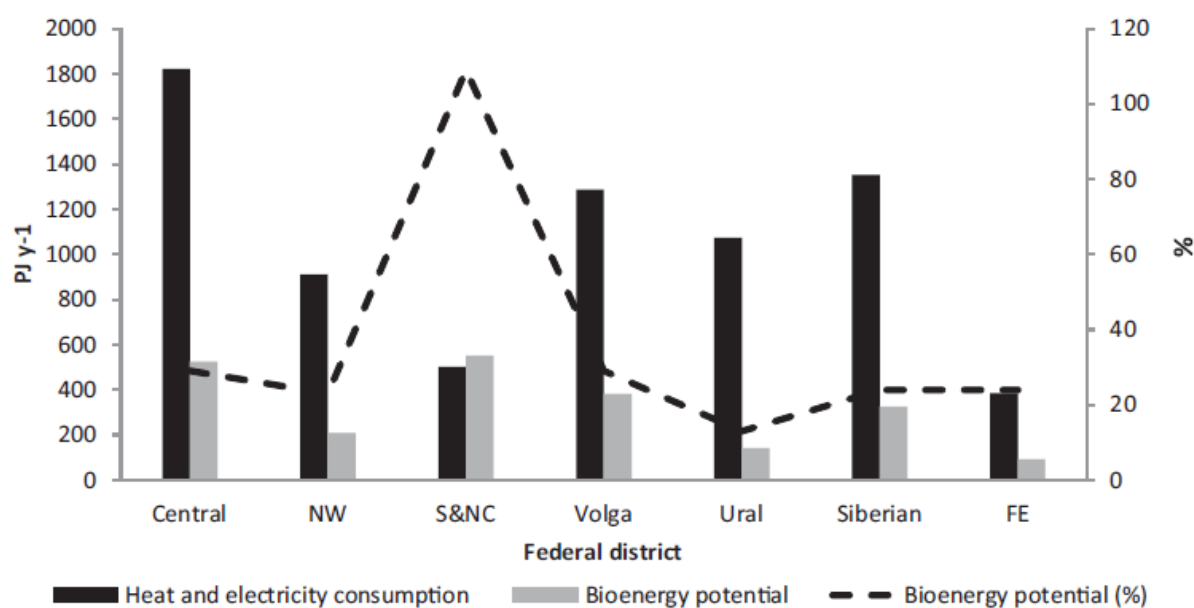
Figure 1.2. Bio-energy resources and total electricity and heat consumption by the Federal **regions** of Russia.[46]

In the Volga and Central Federal **regions**, it is possible to substitute about 28%, and in the North-western Federal **regions**, 23% can be replaced. In Far Eastern federal districts and the Siberian, which include regions not connected to the integrated energy system of Russia, it is possible to substitute 24% of today's

electricity and heat consumption. The Ural Federal district showed the lowest potential for the replacement (about 12.7%), which is distinguished by the high level of power consumption due to the high level of industrial development, The promising strategy for the bioenergy resources of Russia is to use them locally for heat and electricity generation.[39,47-48]

1.1.3. Energies from biomass conversion

The utilization of renewable raw materials is increasingly a focus and the application of biomass as a fuel is now commonplace.[49] Bark, waste from the wood industry, from roadside maintenance and from landscaping, as well as agricultural wastes such as straw or palm fibres serve as fuel. Although the composition of biomass is extremely heterogeneous, all materials have one thing in common:[50] in most cases their water content has to be significantly reduced before they can be used for energy.[30] Conversion of biomass to energy can be done using different processes such as thermo-chemical, bio-chemical/biological, and mechanical extraction (with esterification). Factors like type and quantity of biomass feedstock, end-uses of the energy; environmental standards, and economic conditions influence the choice of conversion.[32] Fig. 1.3 explains different processes involving intermediate energy carriers, and final energy products, and the thermo-chemical conversion of biomass.[51] Combustion, pyrolysis, and gasification are considered as the most important methods for biomass conversion (Fig. 1.3.):
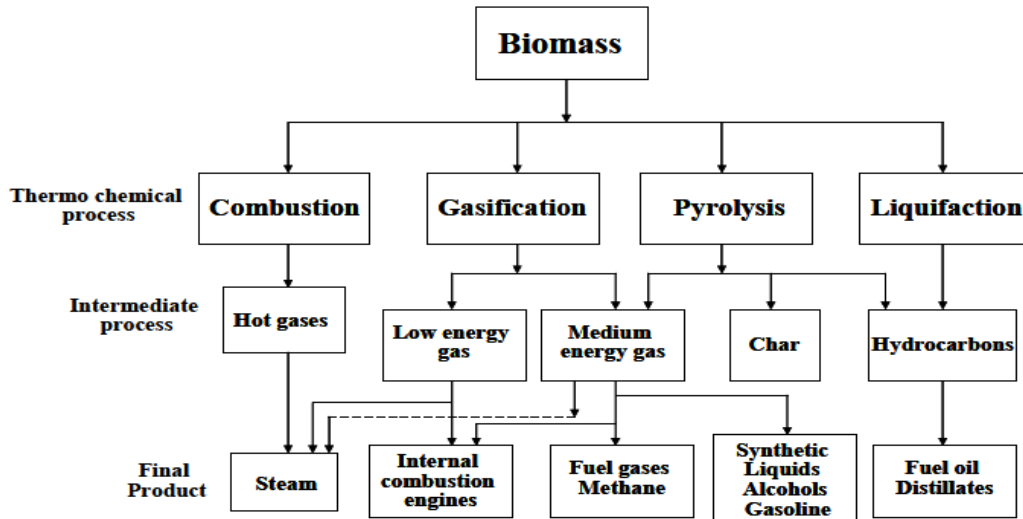
Figure 1.3. Thermo-chemical conversion of biomass into energy.[49]

1.1.3.1. Biomass combustion

Combustion of biomass is a combination process that depends on successive homogeneous and heterogeneous reactions. The essential processes are drying, devolatilization, gasification, char combustion, and oxidation of gas-phase. The time used for each reaction depends on the temperature, fuel properties, and size, and on combustion conditions. Batch combustion of a small particle displays a distinct separation between the char combustion phase and a volatile with time. For the design of combustion systems, the high content of volatiles (80% to 85%) necessities to be respected. For big particles, the phases overlap to a certain extent. However, even for logwood furnaces systems, a certain separation of distinct combustion regimes with time can be observed. Since automatic combustion systems are operated continuously, the sequential reactions occur altogether at various places in the furnace.[50] As a result of the combustion process, different types of pollutants can be produced (Fig. 1.4): (i) Unburnt pollutants such as unburnt carbon, CXHY, HCN, CO, PAH, H_2, soot, N_2O, NH_3, and tar; (ii) Pollutants from full combustion: CO_2, H2O, and NO_X (NO and NO_2); (iii) contaminants such as ash particles, HCl, SO_2, Pb, Cu, Cd, Zn, etc, PCDD/F, and Ash.
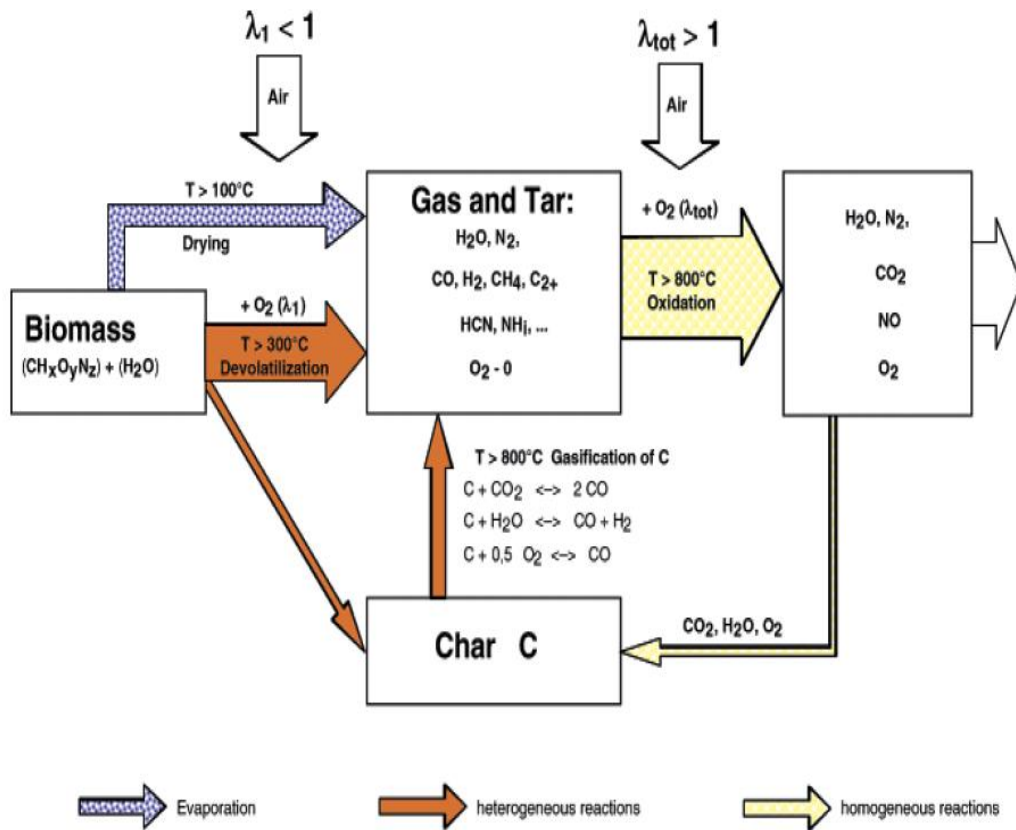
Figure 1.4. Biomass combustion processes, products and pollutants.[50]

1.1.3.2. Biomass gasification

Gasification is defined as the indirect combustion of liquid and solid biomass by converting them to syngas.[28,52-53] It's an alternative process for classic combustion, in which the emission of dust and toxic gases can be reduced.[54] Gasification is classified as non-catalytic and catalytic processes, in terms of gasification agents, and plasma-assisted processes.[55] Common types of gasification equipment, aka gasifiers, are introduced with working principles, through which the advantages and weaknesses of technology are briefly discussed in [56]. The reactions are carried out in a gasification medium such as pure oxygen , air, steam, or a mixture of these gases at temperatures (500–1400 $^{\circ}$C), and atmospheric or elevated pressures up to 480 psia.[32] The major reactions involved in the gasification process are as follows:[57-59]

$$CO + 3H_2 \rightarrow CH_4 + H_2O \qquad \text{Methane reaction} \qquad \Delta H = -206 \; MJ/Kgmole \qquad \text{Eq. 1.1}$$

$$C + 2H_2 \rightarrow CH_4 \qquad \text{Methane reaction} \qquad \Delta H = -75 \; MJ/Kgmole \qquad \text{Eq. 1.2}$$

$$C + O_2 \rightarrow CO_2 \qquad \text{Complete oxidation} \qquad \Delta H = -365 \; MJ/Kgmole \qquad \text{Eq. 1.3}$$

$$C + H_2O \rightarrow CO_2 + H_2 \qquad \text{WGS reaction}^* \qquad \Delta H = +131 \; MJ/Kgmole \qquad \text{Eq. 1.4}$$

$$C + \frac{1}{2}O_2 \rightarrow CO \qquad \text{Partial oxidation} \qquad \Delta H = -111 \; MJ/Kgmole \qquad \text{Eq. 1.5}$$

$$C + CO_2 \rightarrow 2CO \qquad \text{Boudouard} \qquad \Delta H = +173 \; MJ/Kgmole \qquad \text{Eq. 1.6}$$
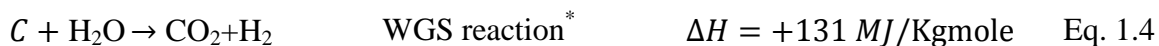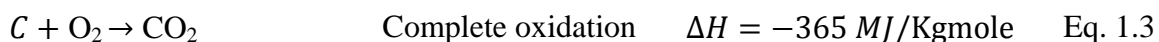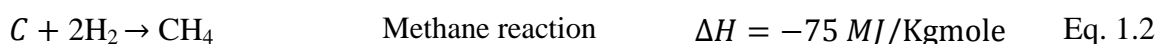
WGS reaction* represents water-gas-shift reaction

All these reactions are in equilibrium, which means that the gas products from the gasification process consist of a mixture of methane, carbon dioxide, carbon monoxide, water vapor, and hydrogen. Gasification produces a medium or low heating gas value. Low heating value gas (about 5 MJ/N-m^3) is burned directly for drying and space heating. It is also used as fuel for gas turbines and gas engines. Medium heating value gas is used as a feedstock to produce considerable liquid fuels like Fischer-Tropsch and alcohols fuels.[60, 61-62]. The types of gas products with the gasifying agents and calorific values (CV) are represented in Table 1.1.

Table 1.1. Types of product gases, their calorific values and gasifying agents[62]

Product gases	Calorific value	Gasifying agent
High CV	40 MJ / Nm^3	Using hydrogenation and hydrogen
Medium CV	16 MJ / Nm^3	Using steam and oxygen
Low CV	5 MJ / Nm^3	Using steam/air and air

1.1.3.3. Biomass pyrolysis

Biomass pyrolysis is considered a promising process of producing valuable biochemical for bioenergy. The petrochemicals that can be obtained by this process from lignocellulosic biomass include furfural, phenolic compounds, and acetic acid. The last product is mostly produced from the partial degradation of cellulose and lignin and the degradation of hemicellulose.[63] Phenolic compounds are the

degradation products of lignin, whereas, Furfural is a typical degradation product of hemicellulose. The mechanism of formation of the above chemicals during pyrolysis of lignocellulosic biomass and presents experimental data for the production of the chemicals via pyrolysis of different lignocellulosic feedstocks under various conditions have been discussed in.[64-65] The gaseous products form pyrolysis of biomass contain water vapor, hydrogen, hydrocarbon gases, carbon dioxide, carbon monoxide, and tars. On the other hand, the by-products of pyrolysis that are not vaporized are referred to as char and consist mainly of fixed ash and carbon.[64]

1.1.4. Production of synthesis gas from biomass

Syngas is a mixture of CO and H_2 that results from all the reactions discussed above, it can be used directly as fuel, besides it is directly used in ceramic fuel cells. Molten carbonate fuel, owing to the presence of carbon monoxide, is totally dissonant with low-temperature fuel cells such as solar-powered electrochemical cells (SPFCs).[65]

Syngas has been used as industrial and domestic fuel, but its low energy/unit volume makes it unattractive if it has to be pumped to a distant consumer.[67] For these applications, the gas can be enriched by transforming it into methane or dimethylamine, or higher alcohols (higher alcohol synthesis (HAS)) or long hydrocarbons (Fischer-Tropsch Synthesis (FTS)) (See Fig. 1.5), All the above reaction are carried out over selective catalysts.[68] These are the ground for many processes of coal gasification. Moreover, the preceding syngas is dangerously poisonous and toxic owing to CO it contains.
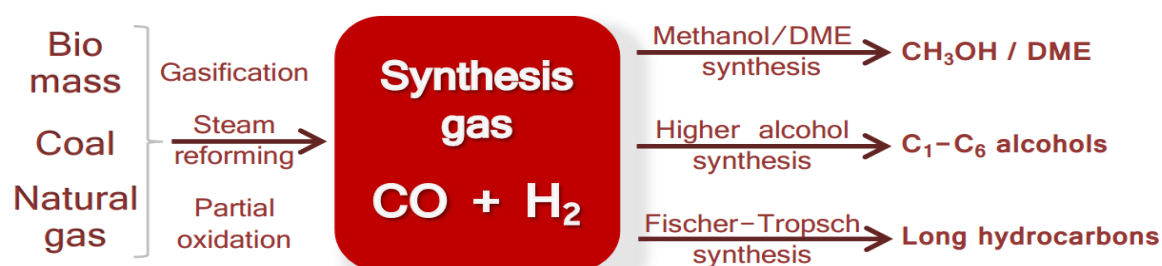
Figure 1.5. Production processes of syngas from biomass and the catalytic reactions of syngas.[68]

The most important benefit of syngas it's considered as feedstock for the synthesis of a huge number of petrochemicals.[69] A lot of these have an C:H ratio basically bigger than that of syngas. That's why, and for its use in low-temperature fuel cells, a hydrogen-enriching step may be needed. This is known as a shift reaction.[70] The contaminants produced with the syngas (see the first reactions in Fig. 1.5) are represented in Table 1.2; they must be removed to permissible limits before the gas can be used.

Table 1.2. The contaminants produced with syngas and their potential issues[71]

Contaminant	Potential issue	Example
Tars	Clogging of filters	Refractive aromatics
Particles	Erosion	Fluid bed material, Ash, char,
Nitrogen Compounds	Emissions	HCN, NO$_x$, NH$_3$
Sulfur, Chlorine	Catalyst poisoning, emissions, corrosion	H$_2$S and HCl

Table 1.3 shows the comparison of synthesis gas from different technologies of biomass gasification. The difference in synthesis gas compositions is attributed to the effect of different characteristics such as the feedstock, type of gasifier, oxidant used, pressure, composition, and temperature.[72-73]

Table 1.3. Comparison between different gasifier operating conditions and the composition of synthesis gas[72]

Gasifier Type	BCL/FER CO[a]	Purox[b]	Shell[c]	MTCI[d]	BFB Range	CFB Range
Reactant 1	Air	O_2 or Air	O_2	--	O_2 or Air	Air
Temperature (°C)	600-1000	1300-1400	1400	790-815	650-950	800-1000
Pressure (bar)	1	1	30	1	1-35	1-19
Feedstock _Inlet conditions_	Wood	MSW	Coal	Pulp	Various	Various
Input (kg/kg feed	0.08	--	0.98	--	0.4-2.2	1.25-1.7
Throughput (tonne/day)	24	181-195	2155	7	4.5-181	9-108
Gas output (m^3/h)	800	33960	$1.48*10^5$	--	335-8793	1181-12500
Heating	18	7.92	9.51	16.7	4-13	4-7.5
H_2 to CO ratio	0.3	0.6	0.36	4.6	0.2-1.6	0.6-1.0
Exit temperature (°C)	820	--	240	--	300-800	600-900

BFB- Bubbling fluidized bed; CFB- Circulating fluidized bed; [a] Indirectly heated CFB with separate combustor; [b] Fixed bed; [c] Fixed bed Fluid bed - Entrained Flow (no circulation); [d] Indirectly heated BFB with separate combustor.

1.2. Higher Alcohol Synthesis (HAS) from syngas

Higher alcohols synthesis (HAS) means the process of production of alcohols that possess two or more carbon atoms, attracting considerable benefit owing to their wide range of applications such as the polymer and chemical industries. They can be widely used as intermediates and feedstock for the production of specialty products and commodities.[73-77] Analogously, Linear-chain fatty alcohols (C_{6+}–C_{22+}) are also synthesized in considerable volumes, nearly equally, from fossil-derived natural resources to accomplish the requirements for the preparation of detergents and surfactants. Regarding the energy sector, HA, in particular isobutanol and ethanol, avail as additives for petro gasoline to increase the motor octane number (MON), which determines the combustion quality in internal combustion engines (ICE).[78-79] The importance of HA in this application is also expected to dramatically increase in the near future owing to the rising need

for fuels of the growing world population, and the phasing-out of the expensive popular ON improver (methyl-tret-butyl ether (MTBE).[80] Moreover, ethanol can work as a hydrogen transporter alternative to less energy-dense and more toxic methanol in fuel cell technologies.[80]

$C_{2+}OH$ and $C_{3+}OH$ are specially synthesized by the fermentation of sugars obtained from starch or sugarcane,[81-84] whereas heavier alcohols are particularly produced by the hydration of the corresponding alkene (fractionated from petroleum) over acid catalysts.[85] Two additional processes for HAS are based on the syngas conversion, a gaseous mixture mostly composed of H_2O, H_2, CO, and CO_2, which is obtained from coal and natural gas. They have reached commercialization, but their contribution to the overall market is considered as limited. The Syngas generation pathways and conversion routes are concluded in Fig. 1.6.
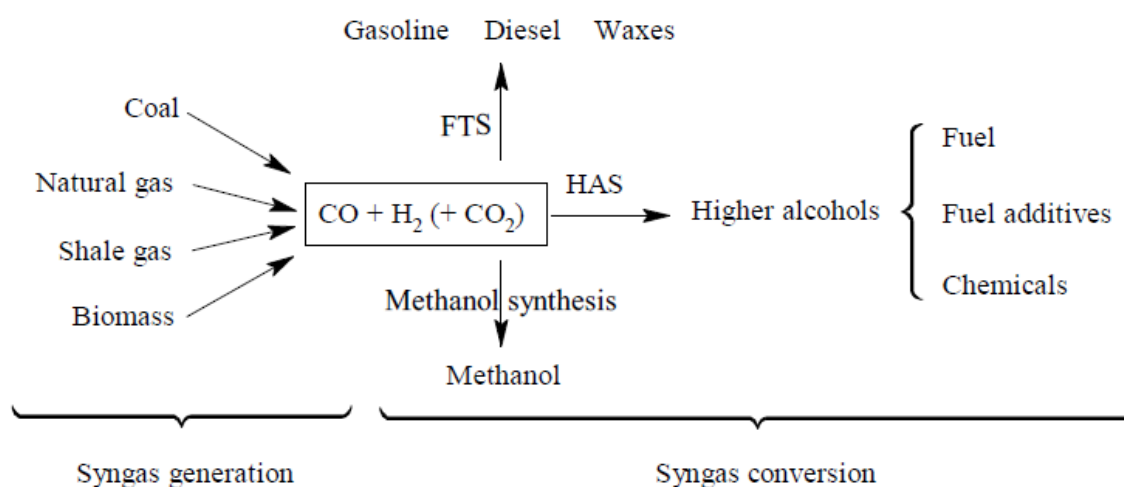
Figure 1.6. Syngas generation pathways and conversion routes.[86]

Synthesis of alcohols from syngas remains an economically attractive method for making fuels and primary materials. Vehicles known as flexible fuel vehicles (FFV) can run on pure ethanol, pure gasoline, and any mixture of both. Pure ethanol vehicles are being commercialized in Brazil.[87] A mixture of gasoline and ethanol (E85 has 85% of ethanol) is commercialized in Europe and the USA. Today, most engines can operate with at least 10% ethanol blended into the

gasoline (E10).[88] Many regions around the world allow a mixture of alcohols to be blended with gasoline, in the range from methanol to octanol (boiling point lower than 210 °C). However, due to its toxicity, the methanol content should preferably be below.

1.3.   Catalysts for HAS from syngas

A wide variety of heterogeneous catalysts were used in the direct conversion of syngas into HA. In general, HAS catalysts classify into four categories: TMS-based, Rh-based, modified MS systems (Methanol synthesis), and modified FTS catalysts. The publications in each category has fluctuated during the years, with revivals of certain materials triggered by the development of nanotechnology tools. Currently, ZnCu- and ZnCr-oxide catalysts are used at the industrial scale.[89] These catalytic systems produce predominantly methanol and small amounts of i-butanol, whereas the most commercialized alcohol used as fuel is ethanol.[90] Another disadvantage of ZnCu- and ZnCr-oxide catalysts is their dramatically low resistance to sulfur poisoning, which is a problem when using sulfur-containing syngas derived from coal and biomass. Transition metal sulfide-based catalysts (TMS) not only are resistant to sulfur[88] but even require sulfur to stay in their active sulfide phase, and can produce high amounts of C1-C5 alcohols when modified by potassium. These systems are promising catalysts for the production of alcohols for industrial purposes.

1.4. TMS catalysts for HAS from syngas

The TMS catalysts have been used in hydrodenitrogenation, hydrodesulfurization, and hydrogenation reactions for over 45 years in petroleum industry.[91] MoS_2 is a layered molecule, where one layer consists of a slab of molybdenum atoms between two slabs of sulfur atoms (S-Mo-S layer). The Mo^{4+} is bonded with six sulfur ligands (S^{2-}) in a trigonal prism order. The layers are bonded by van der-Waals forces (Fig. 1.7). These make MoS_2 similar to graphite. It is notable to mention that the slabs of industrially used MoS_2-based catalysts are

usually not perfect and flat, but partially crystalline, showing adisordered droop morphology.[92]
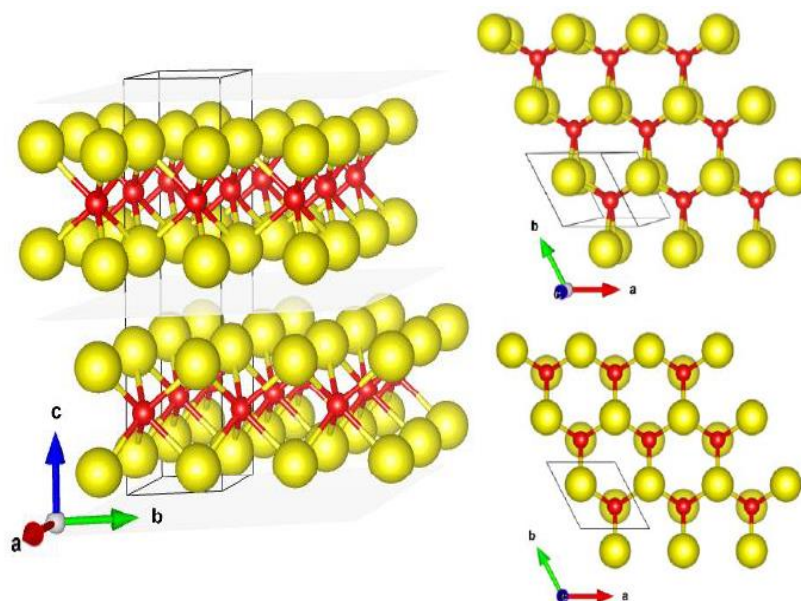
Figure 1.7. Crystal structure of 2H-MoS$_2$ and its typical layered structure. Mo and S are represented in red and yellow, respectively. Proportional atom placement in the molybdenum disulfide monocular layer is shown in the right-upper picture, whereas their positions relative the second layer are illustrated in the right-lower picture.[92]

The MoS$_2$ when modified with alkali metal (mainly potassium) was using as a catalyst for HAS from syngas. The TMS-based catalysts were first developed by Dow and Union Carbide companies to convert synthesis gas to alcohols.[93] (K)MoS$_2$-based catalyst is more applicable for HAS because of the active phase impedance to WGS reaction and sulfur poisoning. Ultra-desulfurization is demanded to decrease the sulfur content (less than few ppb) because sulfur makes the large scale processes more expensive and complicated.[94] Developed TMS-based catalysts became a solution to the affair of creating efficacious production. This economizes the charge of desulfurization for separation of H$_2$O and feed gas.[94] MoS$_2$-based catalysts not only are resistant to sulfur but even require sulfur to stay in their active sulfided phase.[95] Furthermore, these catalysts are also more resistant to the carbonization and CO$_2$ action [97] Rising the temperature of reaction increases the selectivity for HA and hydrocarbons, whereas decreases the

selectivity of MeOH.[97] Syngas conversion on unpromoted MoS_2 yields mainly hydrocarbons, whereas MoS_2 promoted by potassium yields mainly alcohols. Besides, promotion of the catalysts by second transitional metal like Co, Ni, Fe, and Nb increases the catalytic activity. However, to summarize the catalytic performances of MoS_2-based catalysts in HAS from synthesis gas and how we can develop the active phase morphology to increase the production yield of commercial targeted products, three roles should be addressed: (i) effect of promoters (Co, Ni, Fe, and Nb); (ii) Effect of alkali metal; (iii) effect of supports.

1.4.1. The role of second transition metal promoters

In order to shift the product distribution towards higher alcohols, group VIII promoters such as Co, Ni, Fe, and Nb are frequently added to the catalyst.[22,98-100] These promoters work as electron density acceptors on the S-edge of the MoS_2–crystallites, which deactivates the sulfur-edge and decreases adsorption of hydride hydrogen, also leading to increase selectivity towards alcohols at the cost of hydrocarbon selectivity.[100] Several published works have discussed and develop the role of VIII promoters in MoS_2-based catalysts;[24,100-102] Maximov et al.[6] and Permyakov et al.[24] investigated modified and unmodified Bimetallic (Co, Ni, Nb, and Fe) MoS_2 by the DFT method. Besides, they compared the electronic and geometric structures of active sites in terms of CO and adsorption of H-hydrogen. They conclude that the CO conversion on $NbMoS_2$ and MoS_2 catalysts particularly proceeds on the sulfur-edge that has 2 coordinative vacancies per metal atom. Adding of Fe, Co or Ni to the S-edge deactivates it. The promoter atoms in active sites on the sulfur-edge stop hydride hydrogen formation which leads to a decrease of the hydrogenation reaction. The CO adsorption energy on the second metal-edge decreased in the order Fe > Co > Ni.

Maximov et al.[6] also studied the effect of group VIII promoter nature on MoS_2/Al_2O_3 catalysts (Modified and unmodified by alkali metal) in HAS from syngas. Besides they established relationships between promoter nature, hydrocarbon chain length and selectivity of the formed alcohols. They concluded

that electronic structures of the promoter atoms of the active sites were found to strongly influence catalytic performance of HAS. On the other hand, promotion of the S-edge by Co, Ni, or Fe suppresses the hydrogenation reaction, which led to a decrease in the synthesis gas conversion. In contrast, promotion of the metal-edge by Fe, Co, or Ni results in double vacancies, which supports synthesis gas conversion. They supposed that the reaction can occur either on multiple vacancies on the edge of the alkali modified (Me)MoS$_2$ catalyst or on the non-promoted sulfur-edge of the alkali MoS$_2$ catalyst.

Serval studies [6,24,103] confirmed that the activity of molybdenum disulfide-based catalysts is associated with the presence of coordinated unsaturated sites (CUS) on the S- and M-edges. Fig. 1.8 shows the structure of the active site of the MoS$_2$-based catalyst with vacancies on molybdenum and sulfur atoms. [6]
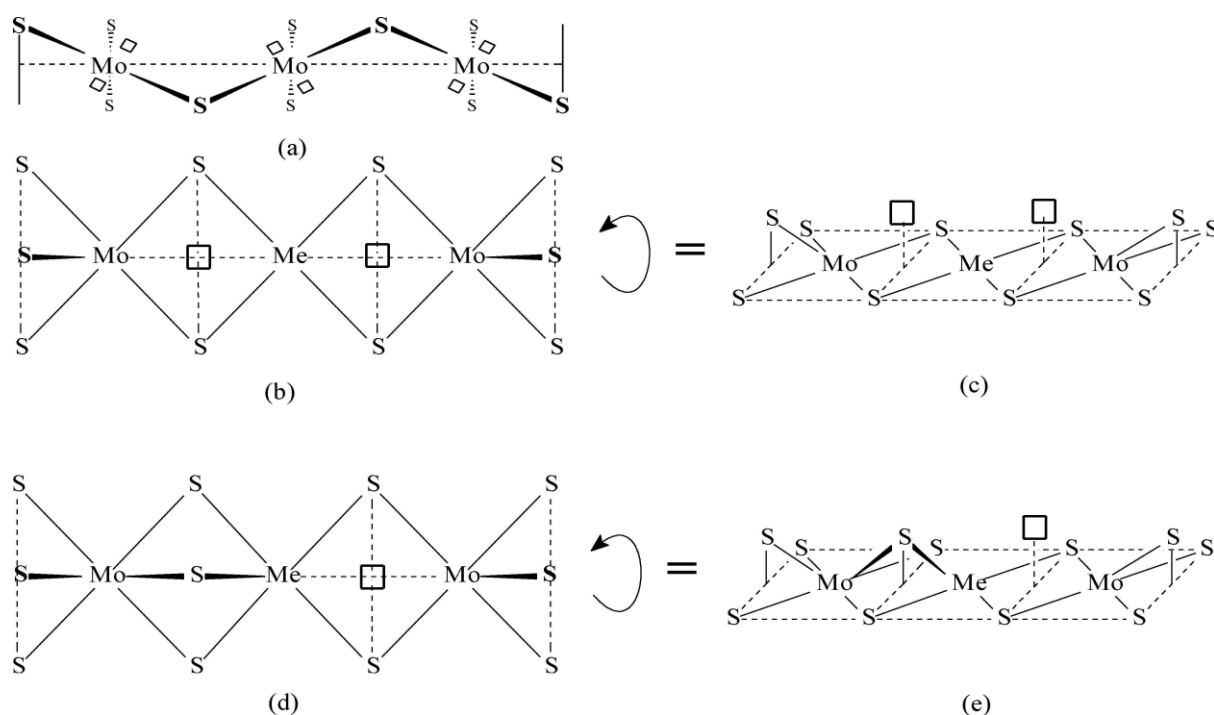
Figure 1.8. The active site of the MoS$_2$-based catalyst structure with vacancies on molybdenum atoms. Coordination vacancies are indicated as empty squares. (a) Active site (non-promoted) on the sulfur-edge, front view. (b) Active site on the M-edge, side view. (c) Me-promoted active site (M-edge) with a double vacancy, top view. (d) Active site on the M-edge, side view. (e) Me-promoted active site (M-edge) with a single vacancy, top view. Me = Mo, Fe, Co, Ni.[6]

The sulfur-edge of MoS_2-based catalyst contains considerable numbers of vacancies (Scheme 1a) in the stable state (thermodynamically), whereas M-edge contains small numbers of vacancies, if any.[24] Based on experimental and computational studies, it was suggested that the M-edge of the unpromoted catalyst does not display activity in HAS from syngas. Their DFT calculations show that adsorption of carbon monooxide and dissociative adsorption of hydrogen occur on the sulfur-edge at (K)MoS sites with the formation of hydride hydrogen.[6] The authors believe that CO intermediate fragments are reduced by hydride hydrogen. In the case of MoS_2 promoted with Co, Ni, or Fe and other metals from G VIII, a mixture of $MeMoS_2$ phase will be composed. Herein, promoter atoms replace some of molybdenum atoms on the crystallite edges.[104] Promotion of the S-edge by the same atoms leads to the formation of (K)MeMoS sites that are not competent for activating adsorption of hydride hydrogen. It leads to inhibition of the CO hydrogenation reaction and promotes higher alcohols synthesis.

Fig. 1.8 b, c represent double sulfide vacancies which are formed on the M-edge at (Co, Ni, or Fe) MoS and its alkali modified sites; these vacancies can participate in syngas conversion. According to experimental data of [6], the sulfur affinity of double vacancies on the M-edge of Fe-promoted sites was extremely higher than for Ni and Co counterparts. These results corroborate the results obtained by [24].

1.4.2. The role of alkali metals

Cobalt (nickel) promoted MoS_2-based catalysts are common industrial catalysts for hydrotreating exceedingly used since 1960.[105-108] According to analytical predictions [109-112] there are no major alternative catalytic systems to substitute them fully over next 25 years. Modification of the catalysts by alkali metals (particularly potassium) shifts selectivity from hydrocarbons to higher alcohols which are used as green fuels and octane number improvers. However, their large scale application needs respectable interest for selectivity towards alcohols.[113] Modification of $Co(Ni)MoS_2$ systems by potassium reduces metal

atoms of active sites and increases average particle length and average stacking numbers in MoS_2-crystallites (Fig. 1.9)[114-116]
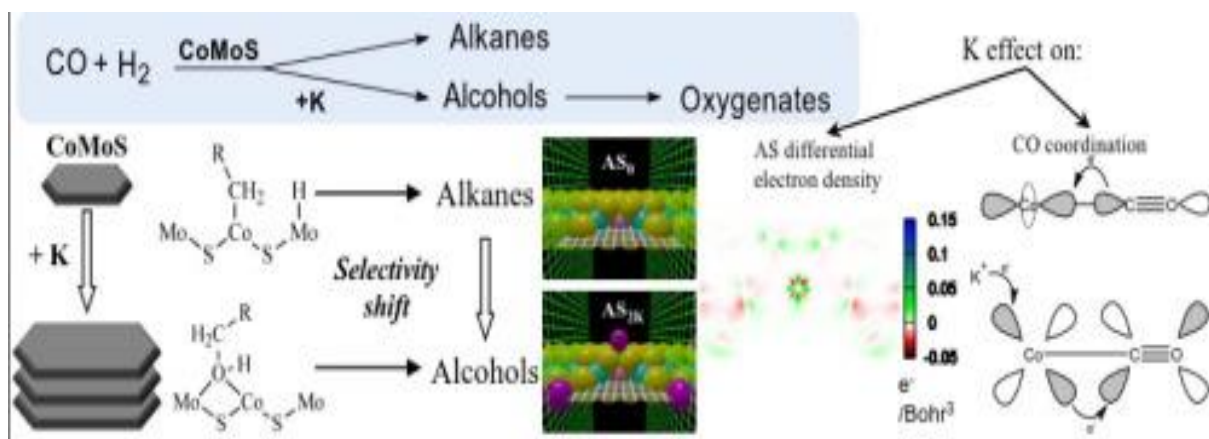
Figure 1.9. The role of potassium atoms in syngas conversion over K-CoMoS$_2$ catalysts aiming to shift the selectivity from hydrocarbons to higher alcohols.[114]

According to the results obtained from quantum chemical calculations of methanol [117-118] and carbon monoxide [119] hydrogenation over MoS_2 catalysts, the C–O split followed by H_2O formation and CH_4 was preferable to carbon chain growth in terms of kinetics and thermodynamics. Moreover, a series of studies have discussed the hypothetical mechanism of syngas conversion over alkali promoted molybdenum disulfide catalysts.[3,22,120-122] Alkali metals (particularly K) play an important role in the suggested reaction mechanisms. The physical and chemical analysis of catalysts in these publications confirmed that potassium is part of the active sites composition (AS); that is why the adsorption of CO molecules increases and hydrogenation (HYD) activity decreases. The most important stage in the HAS is the hydrocarbon chain growth due to the insertion of a new carbon monoxide molecule into the C-M bond in the adsorbed K-intermediate, which produces linear primary alcohols. However, the potassium localization in the molybdenum disulfide crystallites has not been systematically studied so far.

Several studies [3,122-123] have concluded that distribution of K atoms on the catalyst's surface changed in the route of the reaction between potassium atoms spread under the MoS_2 surface and CO and H_2, which can be explained by the intercalation of K atoms into the molybdenum disulfide structure. The intercalation of K metals in molybdenum disulfide crystallites is well known and has been systematically studied elsewhere [123-125]. Moreover, the expected increase of the interlayer distance due to the potassium intercalation was not observed in the published articles what explains the potassium placement in the K-modified MoS_2 catalytic system.[123,125] This behaviour has been explained by the localization of potassium atoms near the edges of molybdenum disulfide crystallites rather than in the interlayer space.[116,126] Adding of potassium simplified an increase in the Fermi level and in the d-orbitals energy of metals. Although the Fermi level increases faster, exceeding the energy growth of metal d-orbitals (Fig. 1.10), this led to reduction of the metal atoms and filling of the metal d-levels.[12]
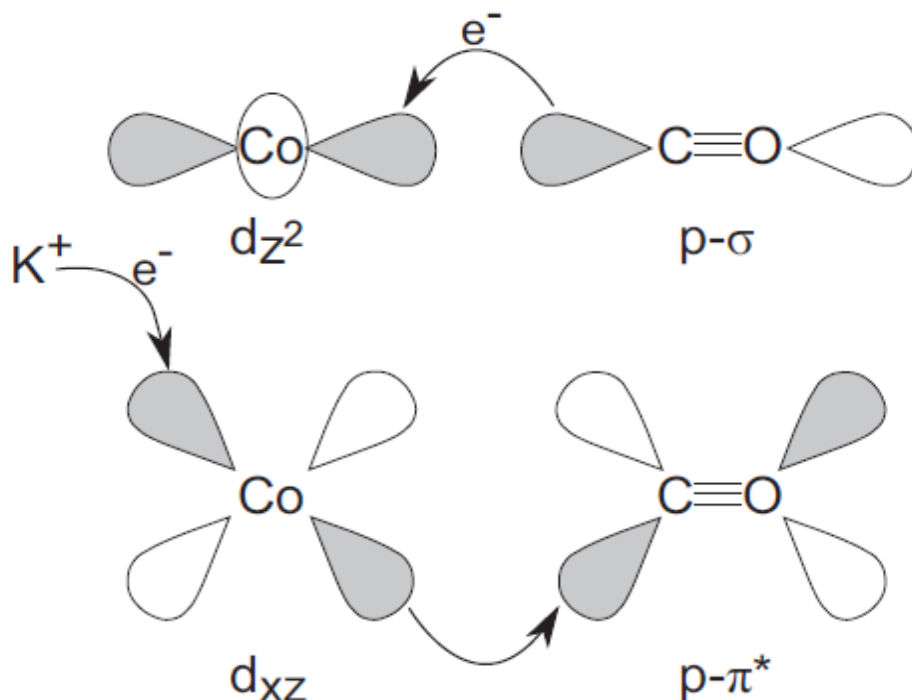

Figure 1.10. Model of electron back donation from Co of the active site to adsorbed CO.[12]

1.4.3. The role of supports

In fact, supports play an important role in the preparation of highly active and selective modified-CoMoS$_2$ catalysts as it impacts electron properties of the formed active phase, morphology, and dispersion. The active phase-support interaction plays a critical role in catalytic hydrogenation processes on heterogeneous catalysts owing to the effect of possible hydrogen spillover. [15,127] H$^+$ formed by dissociative adsorption on the active phase migrates onto the carrier where the reaction continues. In general, the support alters the electron-accepting or electron-donating properties of metal species, their reducibility and dispersion, and promotes the oxygen or hydrogen donation or exchange, as well as stabilizes the active phase and promoters.[11, 128-131]

In HAS from syngas over K-CoMoS catalysts, the catalysts supported on carbon materials show higher catalytic activity than those based on metal oxides (Al$_2$O$_3$, SiO$_2$, MgO, ZrO$_2$), according to several research.[9-11] The majority of these studies interpret the activity of carbon materials as a result of the weak interaction between the carbon and the K-CoMoS active phase, as well as the low acidity compared to metal oxides, which has a positive effect on the selectivity towards alcohols. TMS-based catalysts with high activity and selectivity can be synthesized using a variety of supports that affect the morphology, electron properties, and dispersion of the formed active phase.[114] In the fine chemical industry, activated carbons (AC) are broadly used as a catalyst support due to their specific properties, such as high stability at high reaction pressures and temperatures,[13-15] larger surface area and porosity, resistance to acidic and basic conditions, and minimal interaction between support material and active phase.[16, 17] In addition, because of the delocalized π electronics, electronic conductivity is an important property of AC.[18] Normal activated carbons being microporous (<2nm) causes pore plugging due to the formation of coke and deactivation of the sulfided catalyst, which results in transport limitation in the catalytic reaction.[19] Internal diffusion issues can be avoided by using mesoporous supports with pore diameters ranging from 2–50nm.

The majority of HAS research has been conducted using microporous AC supported catalysts with significantly smaller surface areas ($350–820 m^2/g$) than commercially available activated carbons ($950 m^2/g$ and higher), and the long-term activity of these supported catalysts does not meet commercial levels. Depending on the support's textural properties, such as pore volume, surface area, and average pore diameter, the extent of adsorption, morphology, reduction, and selectivity properties of the active phase can be significantly influenced.[20,23] The authors investigated the role of microporous and mesoporous activated carbons in the production of alcohols from syngas using trimetallic TMS catalysts and discovered that mesoporous AC has higher activity than microporous AC. Rather than surface area or pore volume, they believe that CO conversion and alcohol yield are related to the textural properties of the support, such as pore size and microporosity. There is less dispersion on mesoporous MWCNTs than on microporous ACs, the researchers found. There has been an ever-increasing interest in the use of shaped carbon materials with regular structures, including activated carbons, as catalyst support for syngas conversion.[14,15,132] More than a thousand ACs are available commercially, with different porosities, typically made from different source materials [132] for particular applications.

Anashkin et al.[25] studied the influence of various metal oxide supports (Al_2O_3, SiO_2, TiO_2, ZrO_2) on HAS from syngas over $K-CoMoS_2$ catalysts. It has been concluded that the $K-CoMoS/MO_x$ selectivity towards alcohols also relies on the characteristics of the support and tends to decrease in the sequence $SiO_2 > Al_2O_3 > TiO_2 > ZrO_2$ and that SiO_2 and Al_2O_3 supported catalysts allow obtaining $C_{1+}– C_{4+}$ alcohol mixtures. Another research [133] demonstrated application of the K-modified bimetallic promoted MoS_2-based catalyst supported on the large pore ordered mesoporous carbon in HAS with high product selectivity. The authors showed improved homogenous species dispersion on the MWCNT support using the XRD analytical method of the previous catalysts. They ascribed this phenomenon to the improved textural features of the ordered mesoporous carbon-supported catalyst whose catalytic performance was equivalent to that of its

MWCNT counterpart at greater metal loadings in the active phase. Carbon-based materials compared to conventional alumina used as catalyst supports offer the following advantages: stability at high pressure and temperature, resistance to basic and acidic compounds, and a weak interaction between the metal species (active phase) and the support.
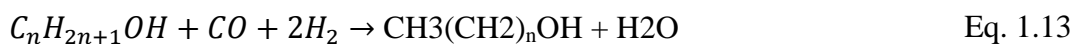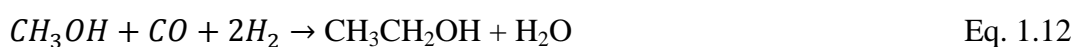
Nonetheless, due to particular commercial characteristics, Al_2O_3 retains its placement as an important support for large-scale heterogeneous catalysts because of its developed mesoporous surface, durability, thermal stability, and high packed density. Therefore, it is advisable to integrate the good characteristics of both types of the supports. To this end, carbon-coated alumina was synthesized as a support for heterogeneous catalysts.[134-136] The method of preparing carbon deposition over alumina and carbon wt. % was found to be crucial factors impacting catalytic performance. According to [114], carbon-coated alumina (CCA) prepared by pyrolysis of organic materials at high temperature in inert gas has beneficial properties as a support for K-CoMoS$_2$ catalysts in HAS from syngas. Carbon on the CCA surface reduces the number of surface hydroxyl groups, while maintaining textural characteristics of alumina, and decreases the interaction between alumina and the metal species.

Graphene prepared as a nanosheet exhibits excellent mechanical strength, high electrical conductivity, and extraordinarily high thermal conductivity. Furthermore, it has a high aspect ratio because of the several micrometer and nanometer thickness of sheets.[137-139] Therefore, it can be effectively utilized as an alternative for amorphous carbon for coating alumina, which is expected to increase supporting efficiency of alumina in HAS from syngas based on TMS catalysts. The most popular methods of GCA (graphene-coated alumina) preparation are plasma spraying, complex CVD, and sol–gel techniques.[140] The latter has been considered the best method, compared to the counterparts, to prepare GCA because it is a well-established and low cost technique for producing

ceramics.[140-143] However, no systematic study on the GCA application for TMS catalysts has been published so far.

1.5. Reaction mechanism for HAS from syngas over K-CoMoS catalyst

According to the reaction conditions and used catalysts, alcohols are produced from syngas by the following reactions: (I) variants of FTS, (ii) a step-wise carbon monoxide insertion and then a condensation reaction (iso-synthesis), (iii) homologation of $C_{1+}OH$ and other smaller alcohols to synthesize higher alcohols, (iv) synthesis of alcohols with one molecule each of $CO + H_2$ following by hydrogenation of the resulting aldehyde (oxo-synthesis), including the hydroformylation of alkenes. The final product includes linear and branched alcohols involving primary and secondary alcohols. Moreover, carbonyl compounds and esters are also synthesized. The equations bellow (Eq. 1.7 to 1.17) represent the chemical reactions included in the synthesis of higher alcohols from synthesis gas:

$CO + H_2O \rightarrow CO_2 + H_2$ $\hspace{4cm}$ Eq. 1.7

$CO + 2H_2 \rightarrow CH_{3OH}$ $\hspace{4cm}$ Eq. 1.8

$C + H_2 \rightarrow CO_2$ $\hspace{4cm}$ Eq. 1.9

$CO + H_2 \rightarrow HCHO$ $\hspace{4cm}$ Eq. 1.10

$2CH_3OH \rightarrow CH_3CH_2OH + H_2O$ $\hspace{3cm}$ Eq. 1.11

$CH_3OH + CO + 2H_2 \rightarrow CH_3CH_2OH + H_2O$ $\hspace{1.5cm}$ Eq. 1.12

$C_nH_{2n+1}OH + CO + 2H_2 \rightarrow CH3(CH2)_nOH + H2O$ $\hspace{1cm}$ Eq. 1.13

$CH_3OH + CO \rightarrow CH_3CHO + H_2O$ $\hspace{2.5cm}$ Eq. 1.14

$3CH_3OH \rightarrow (CH_3)_2CHO + H_2O$ $\hspace{3cm}$ Eq. 1.15

$2CH_3CHO \rightarrow CH_3COOCH_2CH_3$ $\hspace{3cm}$ Eq. 1.16

$(CH_3)_2CO + H_2 \rightarrow (CH_3)_2CHOH + H_2O$ $\hspace{2cm}$ Eq. 1.17

Dorokhov et al. (2016) proposed a reaction network of CO conversion on K-CoMoS-catalyst AS (Fig. 1.11) based on a computational and experimental data. According to the calculations, carbon monoxide adsorbs onto active sites more

substantially than hydrogen. This confirmed that hydrogen adsorbs after carbon monoxide. Then, CO inserts into a metal– hydrogen bond, followed by reductive elimination that leads to form an adsorbed aldehyde. Hydrogenation of the aldehyde adsorbed on the active site results in alcohol synthesis but does not require chain growth and C–O bond split. The C–O bond would break, if hydrogenation does not happen. The K-intermediate may be participated in chain growth or hydrocarbons formation (Fig.1.11). The hydrogenolysis of the carbon-oxygen bond intermediate progresses through a transition state, including the fivefold coordinated C atom, and is liable to steric impediments. The carbon in the C_{1+} hydrogenolysis intermediate state is surrounded by three H atoms, one Cobalt atom, and one O atom, in contrast carbon in the C_{2+} hydrogenolysis intermediate state is surrounded by the alkyl substitutions, 2H atoms, one Cobalt atom, and one O atom. High polarity of the C–O bond supports its nucleophilic hydrogenolysis followed by HC formation or chain growth. Potassium prevents the C–O bond nucleophilic hydrogenolysis by reducing of Lewis acid sites.[12]
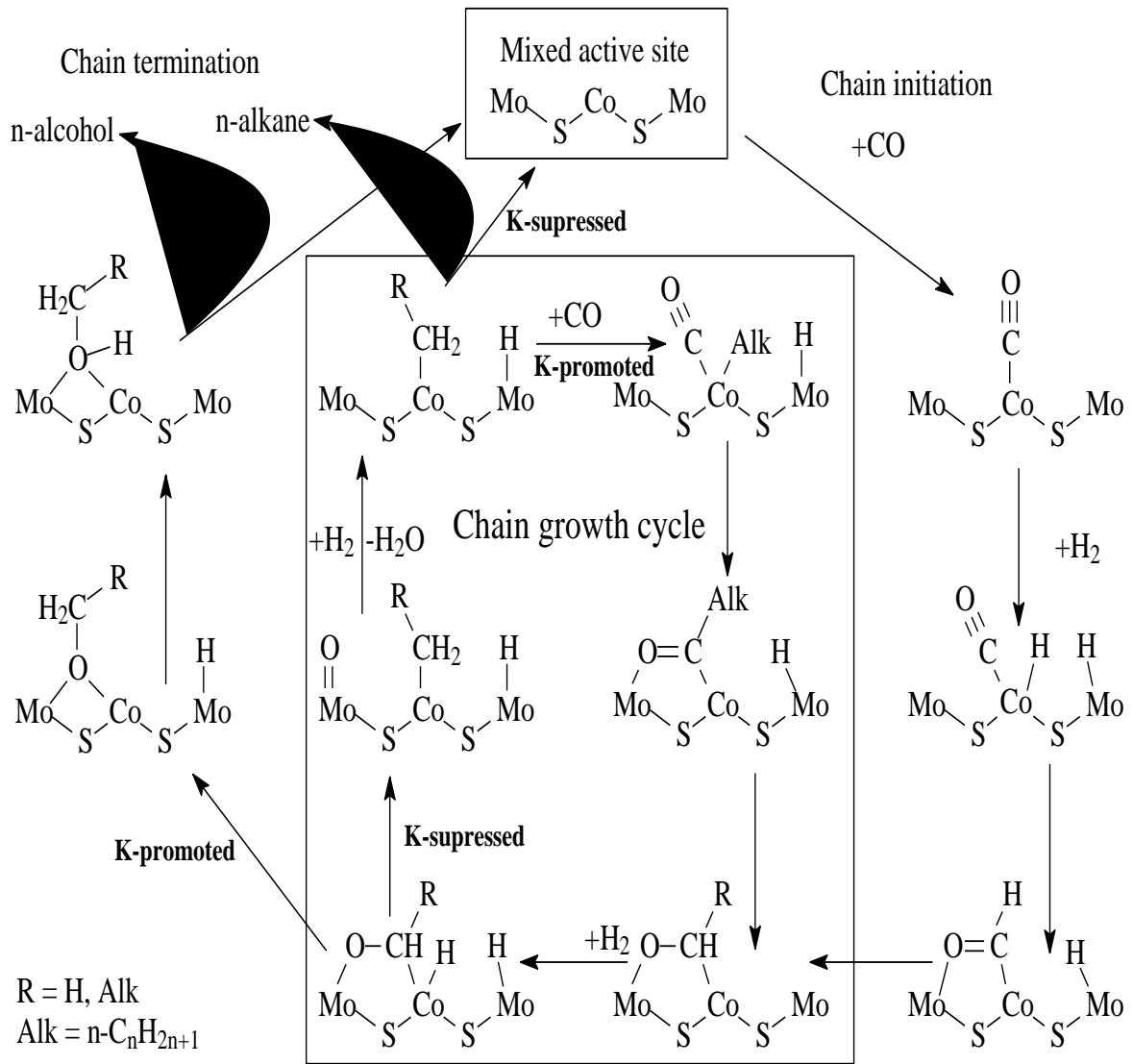
Figure. 1.11. Reaction mechanism of syngas conversion over K-CoMoS active site.[12]

2. MATERIALS AND METHODS

2.1. Preparation of supports and catalysts

2.1.1. Supports

In current investigation several types of materials were used as supports for K-modified K-CoMoS$_2$ catalysts for HAS from synthesis gas, supports are shown in Table 2.1.

Table 2.1. Types of supports under study

Support Abbreviation	Description
Al$_2$O$_3$	γ-Al$_2$O$_3$, obtained from Sigma Chemical Co. (St. Louis, MO, USA)
CCA	Carbon coated alumina Prepared by Pyrolysis
GCA	Graphene coated alumina prepared by combined sol–gel and sonochemical techniques.
AG-3	Powder activated carbons
BAW	
DAC	
OBK-1	
AHM	Fiber activated carbons
TCA	

2.1.1.1. Alumina and carbon covered alumina materials

a. Alumina

The γ-Al$_2$O$_3$ was obtained from Sigma Chemical Co. (St. Louis, MO, USA), crushed and sieved to obtain a particle size fraction of 0.2–0.5 mm. It was calcinated at 550 ^{o}C for 6 h before preparation of the catalyst.

b. Carbon coated alumina (CCA)

CCA was prepared by impregnating 4g γ-Al_2O_3 with about 15mL of a mixture of glycerol and 2-propanol (1:1) followed by pyrolysis under nitrogen (flow rate 1 L/min) at 200 ^{o}C for 40 min and 600 ^{o}C for 1 h, using a heating rate of 10 ^{o}C min^{-1}. The coke content was determined by Thermogravimetric analysis (TGA) using a NETZSCH STA 4449 F3 Jupiter apparatus. Thermogravimetric and differential Thermogravimetric curves for the CCA were recorded in flowing air from room temperature to 600 ^{o}C (heating rate 10 ^{o}C/min).[114] The amount of carbon in CCA is given in Table 2.2. The carbon loading on the CCA support is close to the 1.7% that has been reported to be the optimum loading for alcohol production.[114]

c. Graphene coated alumina (GCA)

Nanostructured GCA was synthesized according to [144] using combined sol–gel and sonochemical techniques. The aluminum-containing sol and alumina nanopowders were prepared from obtainable nonahydrate $Al(NO_3)_3 \times 9H_2O$. (GHOST 3757-75, Russian Federation), it was introduced as an aluminum source without any further purification. The first aluminum nitride aqueous solution (0.05 mol/l) was prepared at 80–85 ^{o}C with magnetic stirring. Sol was formed and stabilized using Dodecylamine "DDA" from MERCK Schuchardt at a molar ratio DDA/Al = 1 at 87.5 ^{o}C. 2,4-Pentanedione (Hacac) was taken as a complexing agent at a molar ratio Hacac/Al = 1. An Al-containing sol was evaporated at 94 ^{o}C until a gel, and then heated at 500 ^{o}C in a muffle furnace for 1 h. As a result, finally, Al_2O_3 nanopowder was prepared.

On the other hand, a synthetic graphite powder with particle sizes between 600–800 mm (from Processing Science manufacture, Russia) was utilized as a carbon species. The graphene was prepared from graphite using a sonochemical technique in one-step procedure. The powder graphite sample was added to the DDA solution in the ethanol–aqua mixture with potassium hydroxide addition. The ratio aqua/ethanol was 1/2; in base media (pH= 10). Deionized aqueous solutions were

prepared by a reverse osmosis Raifil system; specific conductivity <1 µS/cm. Then the mixture of solutions was exposed to ultrasonic radiation (Sonoswiss SW1H, 200W) at 60 ^{o}C for 1 h. The obtained graphene was separated from the reaction medium by decanting and left to stand for 22 hours. Hybrid nanostructures graphene was prepared from light and medium graphene suspension fractions. The graphene suspension fraction was added to the Al-containing solution on a magnetic stirrer at 87 ^{o}C. The mixture was stirred at 87 ^{o}C for 35 min and then the temperature was raised by 5 ^{o}C and the sol evaporated until the gel form. The hybrid gel was calcined in a muffle furnace for 3 hours at 500 ^{o}C. Linear sizes of the sheets ranged from a few nanometers to several microns at a thickness of 5–7 nm. Data on the catalyst samples supported on carbon coated alumina materials with the different carbon content are given in Table 2.2.

Table 2.2. Weight percentage of amorphous carbon and graphene in carbon coated materials

Catalyst	Carbon in CCA (wt. %)	Graphene (wt. %)
CCA	1.7	-
GCA1	-	1.7
GCA2	-	1.2
GCA3	-	0.4

2.1.1.2. Activated carbons

a. Powder activated carbons

Activated carbon AG-3 (commercial trademark АГ-3) was obtained from weakly coking coal crude and coal semi-coke with coal tar pitch binder by preparation of dough, granulation, carbonization, and gas-vapor activation. Activated carbon BAW (commercial trademark БАУ) was manufactured from irregular shaped charcoal grit via gas-vapor activation at 850–900 ^{o}C. Activated carbon DAC (commercial trade mark ДАС) was obtained from anthracite (hard

coal) by preparation of dough, granulation, carbonization, and gas-vapor activation. Activated carbon OBK-1 (commercial trade mark УПС-1) was manufactured based on carbonaceous composition prepared from gas-vapor activation at 850-900°C.[145]

b. Fiber activated carbons

Fabric active sorption (TCA) is an elastic sorbent obtained by heat treatment of technical fabric, which was previously impregnated with chemical compounds. It was formed as canvases with dimensions: length 20 m, width 0.55 m, thickness 0.6 mm. Non-woven activated material (AHM) was produced by heat treatment of a nonwoven needle-punched material based on viscose fibers and mtilon fibers. The parameters of the active layer are aerodynamic resistance 10 Pa, surface density 120 g m^{-2}, thickness 1.0-3.5 mm[145].

2.1.2. Alkali-modified CoMoS$_2$ catalysts

The catalyst precursors were prepared by incipient wetness impregnation. Ammonium heptamolybdate tetrahydrate (Alfa Aesar, chemically pure 99%; 5 mmol, 0.48 g) was dissolved in a mixture of 1 mL of NH$_4$OH (20%) solution and 1.5 mL of distilled water, then mixed with 0.40 g (10 mmol) of KOH (analytical grade, 98%). The produced solution was added to a mixture of cobalt acetate (Alfa Aesar, tetrahydrate, chemically pure 98%; 2.5 mmol) and 1.05 g (5 mmol) of citric acid in 1 mL of distilled water. The impregnated supports (3 g) were dried in flowing air (1 L/min) for 2 h at 60 $^{\circ}$C and then for 5 h at 100–110 $^{\circ}$C. The catalyst precursors were sulfided in an autoclave using crystalized (elemental) sulfur (1:4 catalyst: sulfur) at 360 $^{\circ}$C under H$_2$ at 6.0 MPa for 1 h. The supported catalysts are denoted as Cat-Al$_2$O$_3$, Cat-CCA, Cat-GCA, Cat-AG-3, Cat-BAW, Cat-DAC, Cat-OBK-1, Cat-AHM, and Cat-TCA, where Cat denotes the active phase K-CoMoS$_2$.

2.2. Physical characteristics of supports and catalysts

Textural characteristics for supports and catalysts were studied via N_2 adsorption and desorption isotherms measured using a Quantachrome Nova 1200e (Anton Paar, Graz, Austria) instrument at 77 K, approximately 0.1 g of each sample, and calibrated sample cells. Oxidic samples were kept under argon flow for 3 h and sulfided samples were kept under hydrogen flow for 3 h before degassing. The oxidic samples were degassed at 110 ^{o}C for 4 h at 10–4 mm Hg and the sulfided samples at 250 ^{o}C for 4 h at 10–4 mm Hg. The specific surface area was determined using the BET equation. The total pore volume was characterized at a relative pressure p/p0 = 0.99. The mesopore size distribution and volume (considering the adsorption film thickness on the mesopore surface) were calculated from the desorption branch of the isotherm using the Barrett, Joyner, and Halenda (BJH) method.[146] The micropore volume was determined using the t-plot method [147] and by comparing the total pore and mesopore volumes.

The surface morphology of both supports and catalysts was studied using a Hitachi SU8000 Field-Emission Scanning Electron Microscopy (FE-SEM). The samples were mounted on 25 mm aluminum specimen stubs using conductive adhesive tape. Uncoated samples were studied to avoid metal coating surface effects. Secondary electron images were acquired at 10 kV accelerating voltage and 8-10 mm working distance.

A LaB6 Tecnai G2 20F Transmission Electron Microscope (TEM) (Thermo Fisher Scientific, Waltham, MA, USA) operated at 200 kV and a FEG Tecnai G2 30F TEM (ThermoFisher Scientific, Waltham, MA, USA) operated at 300 kV were used to characterize the morphology of the sulfided catalysts, dispersed on continuous or Quantifoil™ (Großlöbichau, Germany) R1.2/1.3 microgrid carbon film on copper TEM grids by dry dipping or ethanol suspension. Average slab length and average degree of stacking were evaluated from representative TEM images by manually measuring 300–400 individual slabs using the Fiji software package imageJ program.

2.3. Elemental composition

The elemental composition of the catalysts was determined using an EDX-7000 X-ray fluorescence (XRF) (Shimadzu, Kyoto, Japan) spectrometer with a Rh tube anode operated between 8–200 mA and 15–50 kV. All samples were crushed before measurements. The spectra were processed using the method of fundamental parameters.

2.4. Acidic properties

Analysis of acid–base properties of the supported catalysts was performed by determining how much pyridine is adsorbed from a pyridine solution in octane. The pyridine concentration was determined using an SF-103 single-beam scanning UV spectrophotometer (Aquilon, Moscow, Russia). Fig. 2.1 shows the calibration spectra; the adsorption maximum is at 252 nm regardless of the pyridine concentration. Fig. 2.2 shows the calibration line, with R = 0.999.
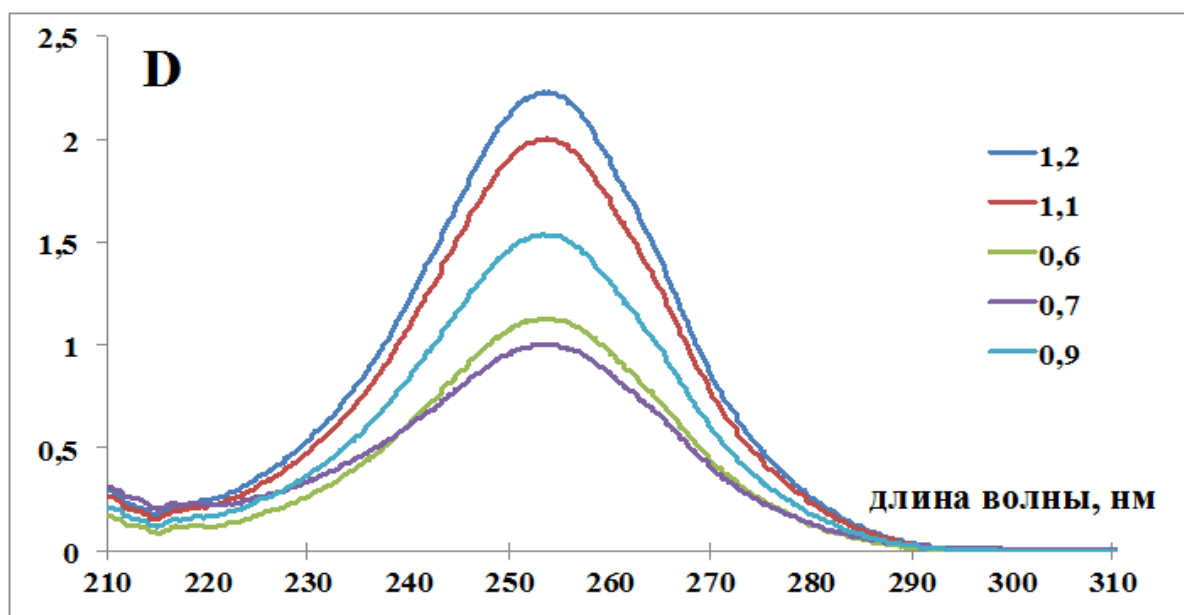

Figure 2.1. UV absorption spectra of pyridine in octane. Legend shows the concentration in mol L^{-1}.

The concentration is calculated according to the formula in accordance with the Bouguer-Lambert-Beer law D = E C x, where A is the optical absorption, C is the concentration of the solution (mol L^{-1}), x is the optical path length (cell thickness). Gibbsian adsorption (G, mol g^{-1}) was calculated using Equation (2.1):

$$G = \frac{(C_0 - C_\tau)V}{m} = \frac{(D_0 - D_\tau)V}{m\varepsilon l} \qquad \text{Eq. 2.1}$$

where V is the volume of the solution (10 mL); m is the mass of the sample (0.1 g); D_0 and D_t are the optical density at the maximum absorption of pyridine before and after adsorption; l is the thickness of the cuvette (1 cm); ε " is the molar absorption coefficient (extinction, " pyridine = 2106 L mol^{-1} cm^{-1}" octane = 1104 L/(molcm)).
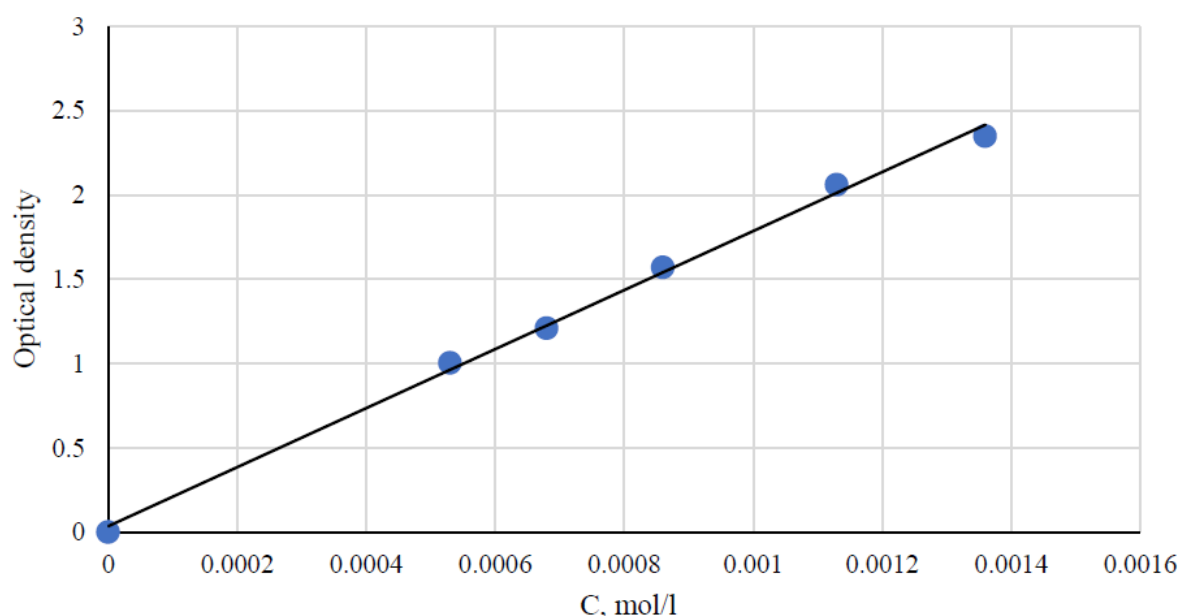

Figure 2.2. Calibration dependence of the UV signal (D) of the solution on the concentration of pyridine (mol L^{-1}) at 252 nm. y = 1749.8x + 0.0359; R² = 0.997.

2.5. X-ray photoelectron spectroscopy (XPS)

The sulfided catalysts were analyzed by XPS using Kratos Axis Ultra DLD spectrometer with monochromatic AlK* source (h* = 1486.6 eV, 150 W). The individual spectral regions were analyzed to determine the binding energy (BE) of the peaks, identify the chemical state of the elements and calculate the relative

ratios of the elements on the catalyst surface. The BE values were referred to the positions of Au $4f_{7/2}$ peak at 83.96 eV and Cu $2p_{3/2}$ peak at 932.62 eV. To the survey photoelectron spectra, narrow spectral regions (Al 2p, S 2p, Mo 3d, C 1s, O 1s, Co 2p) were recorded. The collected spectra were processed by a mixed Gaussian (30 %) – Lorentzian (70 %) method with the use of CasaXPS software program. A Shirley background subtraction was applied for atomic concentrations calculation. The decompositions of the S 2p and Mo 3d XPS spectra were performed using the appropriate oxide and sulfided references as supported monometallic catalysts. Atomic concentrations of each element for every sulfided catalyst were determined. Relative concentrations of each species, cobalt oxide Co^{2+}, Co_9S_8, CoMoS, molybdenum oxide Mo^{6+}, MoSxOy and MoS_2, for every sulfided catalyst were determined. For example, the relative amount of Co in the CoMoS phase was determined using the following equation:

$$[\text{CoMoS}]\ (\%) = \frac{A_{\text{CoMoS}}}{A_{\text{CoMoS}} + A_{\text{Co}_9\text{S}_8} + A_{\text{Co}^{2+}}} \times 100 \ , \qquad \text{Eq. 2.2}$$

where AX represents the peak area of species x.

The effective Co content (wt. %) in the CoMoS phase was determined as follows:

$$C_{\text{CoMoS}} = [\text{CoMoS}] \times C(\text{Co})_{\text{T}} , \qquad \text{Eq. 2.3}$$

where $C(\text{Co})_T$ represents the effective concentration of cobalt on catalyst surface determined by XPS (at.%).

The promoter ratio in the CoMoS phase slab was calculated using the following relations:

$$\left(\frac{\text{Co}}{\text{Mo}}\right)_{\text{slab}} = \frac{C_{\text{CoMoS}}}{C_{\text{MoS}_2}} \qquad \text{Eq. 2.4}$$

where C_{CoMoS} and C_{MoS2} are absolute concentrations of Co and Mo in the CoMoS and MoS_2 species, respectively (at %).

The promoter ratio in the slab edge of the active phase was calculated as follows:

$$\left(\frac{Co}{Mo}\right)_{edge} = \frac{(Co/Mo)_{slab}}{D} \qquad \text{Eq. 2.5}$$

where D is the dispersion of the active phase particles obtained using TEM measurements.

The signal at 169.0 eV (characteristic of sulfates) was almost absent indicating that the sulfided catalysts were not reoxidised during the transfer from the sulfiding reactor to the XPS chamber.

2.6. Catalytic experiments

Syngas conversion was carried out in a fixed-bed flow reactor (Fig. 2.3) using 3 g of sulfide catalyst, P = 5.0 MPa, T = 300–360 °C, mass flow rate 760 L h^{-1}(gcat)$^{-1}$, and a feed gas composition of CO:H$_2$:Ar = 45%:45%:10%. The catalysts were evaluated for 4h at each temperature (steps of 20 ^{0}C) at T = 300–360 °C. Every 4 h gaseous products were analyzed using a LHM-80 GC with a Thermal Conductivity Detector (TCD) and two one-meter packed columns (molecular sieves CaA (Ar, CH$_4$, CO) and Porapak Q (CO$_2$, C^{2+})). Argon was used as an internal standard for gas chromatography (GC). The liquid products (alcohols, aldehydes, esters, etc.) were analyzed using a Crystal-2000M GC with a flame ionization detector (FID) and a 50 m HP-FFAP capillary column. Carrier gas was high purity helium for both GCs. The conversion of CO (X) was calculated as follows.[6] (Eq. 2.6):

$$X_C(\%) = 1 - \frac{n_{CO}^{After\ reaction}}{n_{CO}^{In\ feed}} \times 100 \qquad \text{Eq. 2.6}$$

Where X_C = syngas conversion and n_{CO}^{feed} and $n_{CO}^{Afterreaction}$ = CO content.

The selectivity in this reaction is calculated on a CO_2-free basis approximation, because the CO_2 is mainly formed in the course of water gas shift or Boudouard reactions and is considered as a by-product, constantly affecting selectivity of target products. That is why CO_2 was excluded from selectivity balance calculations. CO_2-free selectivity was calculated according to Eq. 2.7:

$$S_i^{CO_2-free}(\%) = \frac{S_i}{1 - S_{CO_2}} \times 100 \qquad \text{Eq. 2.7}$$

where $S_i^{CO_2-free}$ — CO_2 free selectivity to i component; S_i – selectivity to i component; S_{CO_2} – CO_2 selectivity.
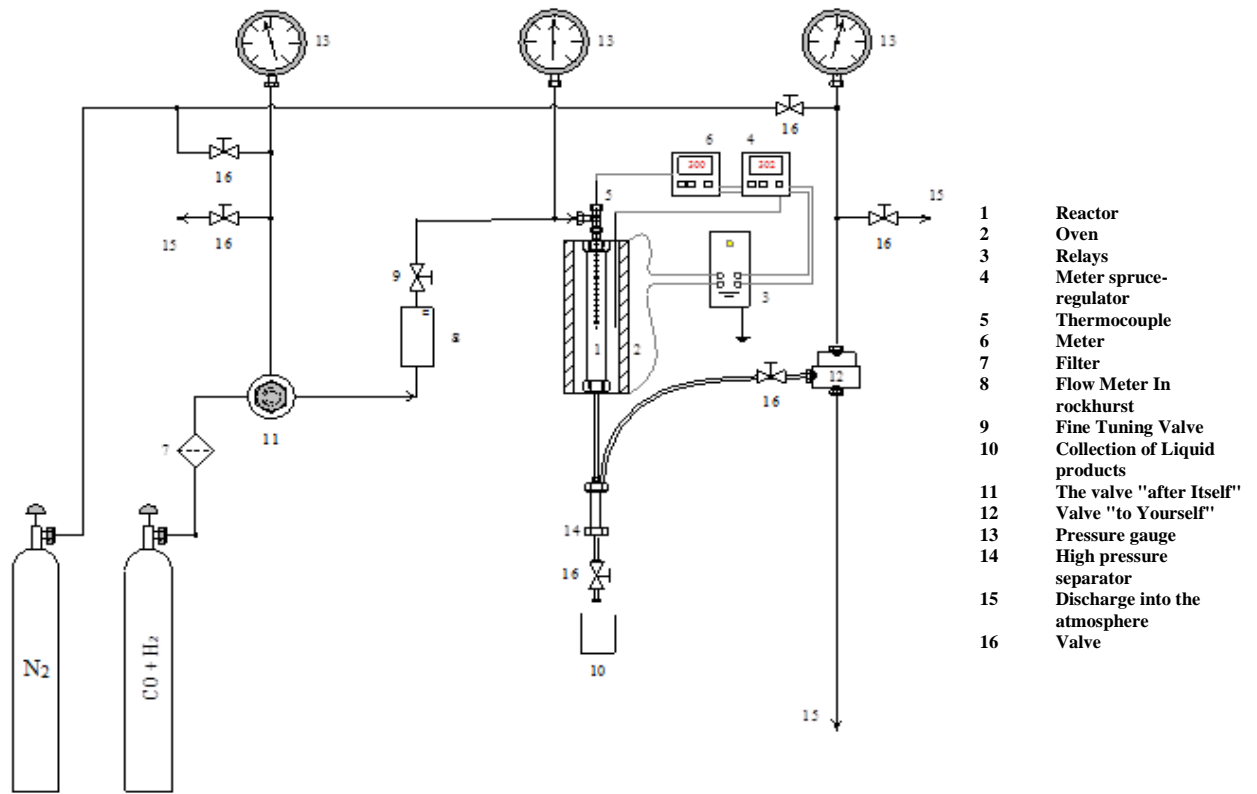
The carbon chain growth factor α_i was calculated using Eq. 2.8:[6]

$$\alpha_i = \frac{\sum_{k>i} \frac{Y_k}{k}}{\sum_{k\geq i} \frac{Y_k}{k}} \qquad \text{Eq. 2.8}$$

where α_i – chain growth factor for the intermediate with i number of carbon atoms; Y_k – yield of the component with the k number of carbon atoms.

The factor α_1 is the probability of CO insertion to an intermediate containing one carbon atom with the formation of an intermediate with two carbon atoms; α_2 that of the next step of CO addition to the intermediate with two carbon atoms, etc.

Figure 2.3. Scheme of fixed-bed flow reactor

1	Reactor
2	Oven
3	Relays
4	Meter spruce-regulator
5	Thermocouple
6	Meter
7	Filter
8	Flow Meter In rockhurst
9	Fine Tuning Valve
10	Collection of Liquid products
11	The valve "after Itself"
12	Valve "to Yourself"
13	Pressure gauge
14	High pressure separator
15	Discharge into the atmosphere
16	Valve

3. RESULTS AND DISCUSSION

3.1. Development of catalytic activity of K_{10}-Modified $Co_{3.7}Mo_{10}S/Al_2O_3$ catalyst by coating alumina using graphene

The comparative study of the catalytic behavior of K-modified $CoMoS_2$-catalysts supported on Al_2O_3, carbon covered alumina (CCA) and graphene coated alumina (GCA containing 0.4, 1.2, and 1.7% of graphene) in synthesis gas conversion to higher alcohols has been carried out. Due to particular commercial characteristics, alumina retains its placement as an important support for large scale heterogeneous catalysts because of its developed mesoporous surface, durability, thermal stability, and high packed density, besides, the good properties of carbon materials as catalyst supports. Therefore, it is advisable to integrate the good characteristics of both types of the supports. To this end, carbon-coated alumina was synthesized as a support for heterogeneous catalysts.[134-136]

A search of catalysts for HAS involves studying various factors such as the nature of the support, textural characteristics, optimum composition of the active phase, morphology, diversity, etc.[8] Al_2O_3, carbon coated alumina (C=1.7%) and graphene nanostructured coated alumina with different wt. % (0.4, 1.2, and 1.7%) were selected as supports to prepare K-Modified $CoMoS_2$ catalysts by simultaneous dry impregnation of the metal precursors.

**Table 3.1.** Textural characteristics of the supports and catalysts

Sample	S_{total}, m^2/g	S_{micro}, m^2/g	S_{meso}, m^2/g	Average pore diameter (nm)
K-CoMoS$_2$/Al$_2$O$_3$	91.00	0.00	91.00	13.64
K-CoMoS$_2$/CCA	73.00	0.00	89.80	14.18
K-CoMoS$_2$/GCA1	119.84	0.00	76.79	13.17
K-CoMoS$_2$/GCA2	94.40	4.06	90.34	13.03
K-CoMoS$_2$/GCA3	80.74	2.24	78.50	14.01

The textual characteristics of alumina improved after coating by carbon and graphene nanosheets of different wt. % because its total surface area increased after coating by 1.7 % of graphene, whereas the pore diameter were almost stable because graphene was prepared as two-dimensional sheets of varying thicknesses (5–7 nm).[148-149] The presence and amount of carbon influences the total surface area (Table 3.1). The observed microporous structures in Cat-GCA2 and Cat-GCA3 return to the micropore structures in graphene nanosheets. We believe that the absence of micropores in the case of Cat-GCA1 is due to the fact that the sheets of graphene in the case of Cat-GCA2 (1.2%) and GCA3 (0.4%) form windows on the surface of alumina. Because the graphene amount in GCA1 is greater than in Cat-GCA2 and Cat-GCA1, these windows are closed and therefore the microporous structures disappeared from the surface. The targeted and measured compositions of supported-K-CoMoS$_2$ catalysts are shown in Table 3.2.

Table 3.2. Elemental compositions of supported catalysts

| Catalyst	Targeted composition (wt. %)			Measured composition (wt. %)		
	K	Mo	Co	K	Mo	Co
K-CoMoS$_2$-Al$_2$O$_3$	10	12	3.7	9.5	10.8	4. 7
K-CoMoS$_2$-CCA	10	12	3.7	8.0	13.8	3.6
K-CoMoS$_2$-GCA1	10	12	3.7	9.6	12.9	5.2
K-CoMoS$_2$-GCA2	10	12	3.7	11.8	14.1	3.6
K-CoMoS$_2$-GCA3	10	12	3.7	11.8	13.1	3.8

The prepared GCA materials were characterized and identified using XRD, HRTEM, and EELS datum.[148] The surface morphology of K-CoMoS$_2$/sup characterized by SEM is shown in Fig. 3.1.
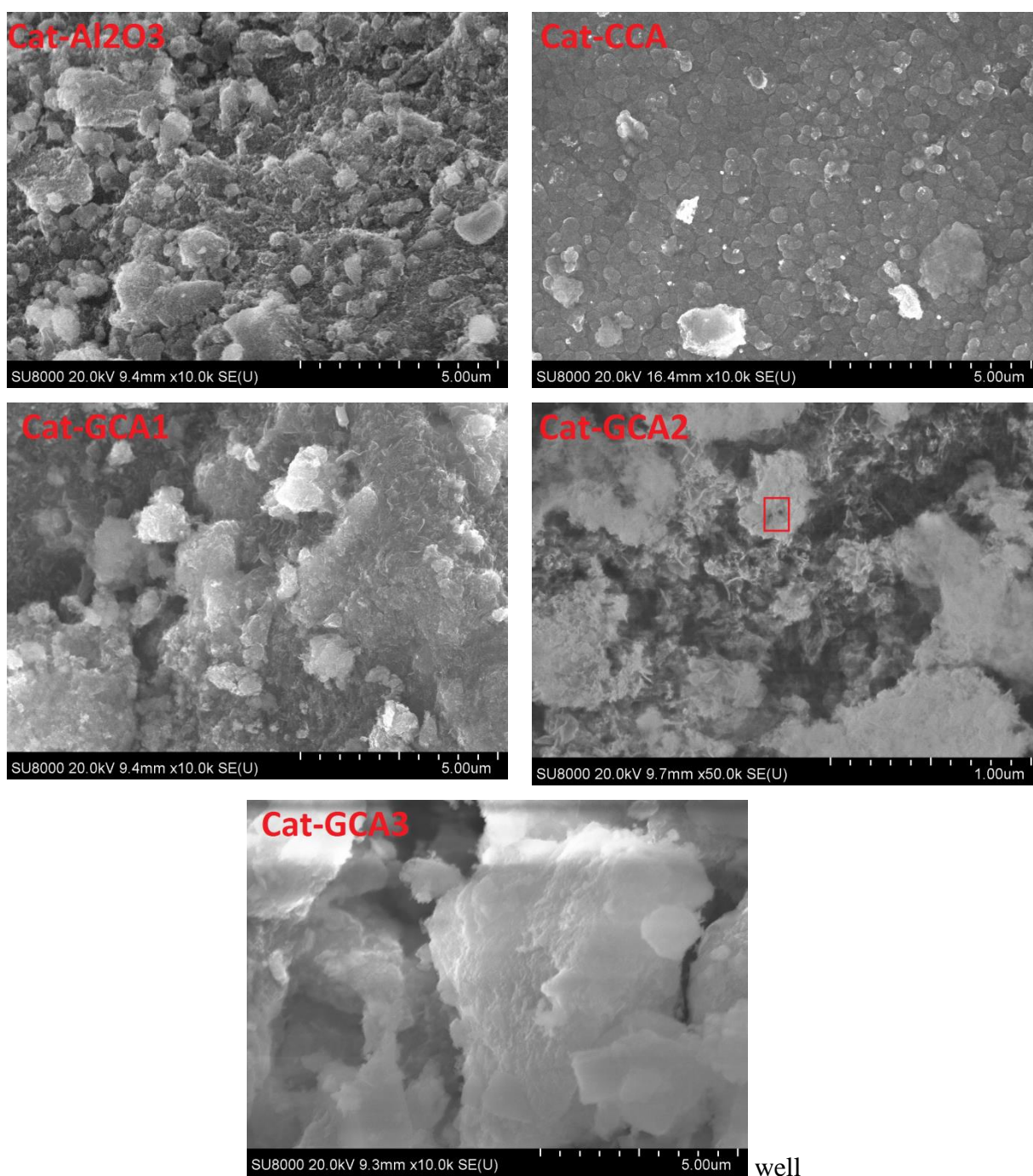
Figure 3.1. SEM images of the K-CoMoS$_2$ catalyst supported on Al$_2$O$_3$, CCA, GCA1, GCA2, and GCA3.

Fig. 3.1 shows that surface morphologies of the catalysts under study are formed as agglomerated flower-like structures. In Cat-CCA, Al$_2$O$_3$ is well crystallized with a partial coating by amorphous carbon prepared by pyrolysis and a small agglomeration of the impregnated active phase. In Cat-GCAs, the coating was not well visible because graphene is transparent. The images of Cat-CCA and Cat-GCAs (Fig. 3.1) show a large number of bulges protruding above the surface

of the partial coating. The EDX maps for the composition of the main elements of the supported K-CoMoS$_2$ catalysts (S, Mo, Co, K, C, O) are shown in Fig. 3.2.
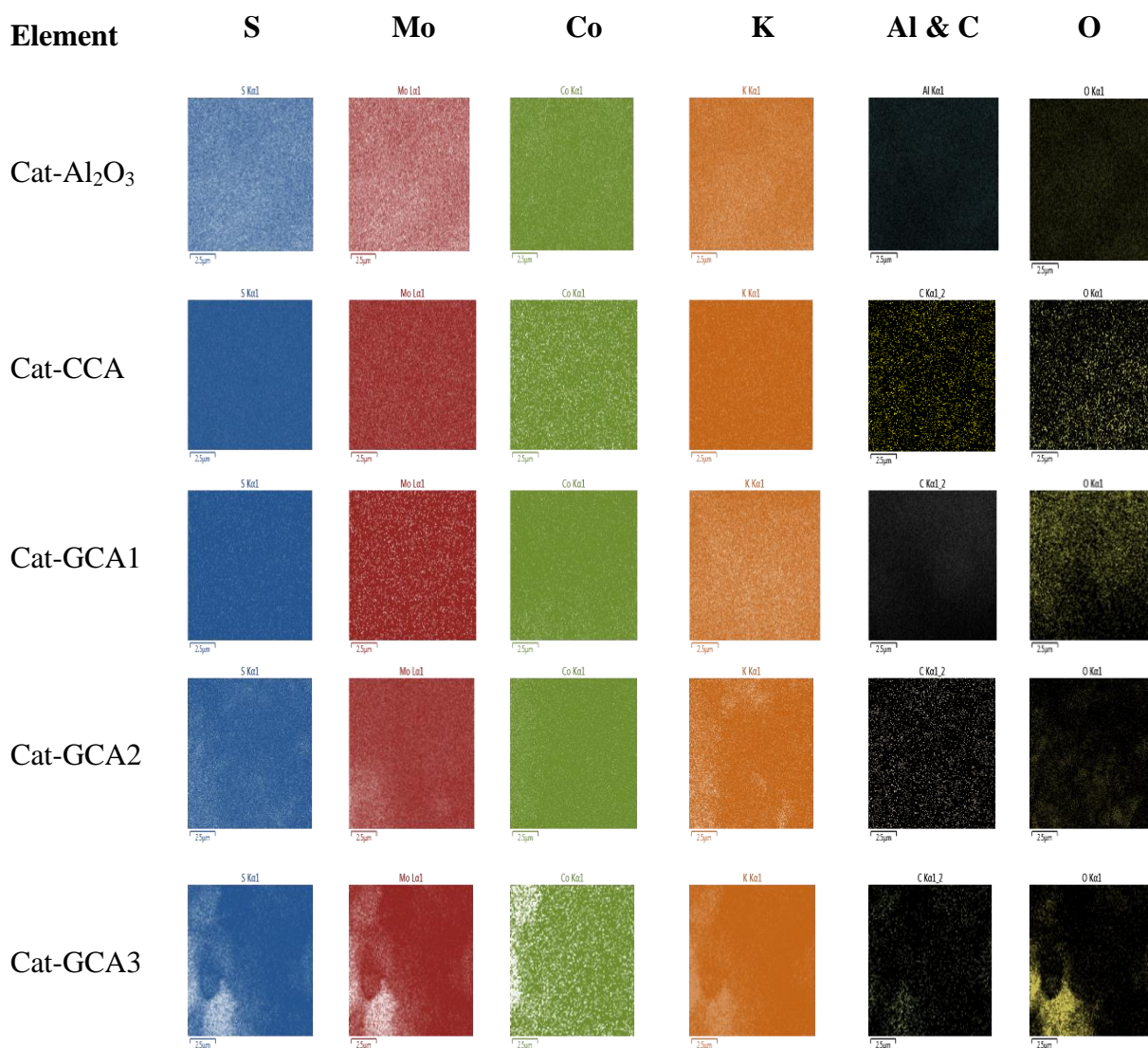
**Figure 3.2.** EDX mapping of K-CoMoS$_2$ supported on Al$_2$O$_3$, CCA, GCA1; GCA2, GCA3.

Element distribution maps (Mo, Co, K, and S) produced on the supported K-CoMoS$_2$ catalysts surface entirely coincide, indicating that the components constitute a single phase. Thus, all metals are in close contact with each other, and molybdenum basically acts as a "sulfur protector" with some other phases of CoS$_x$. A larger agglomeration with lower dispersion of Mo and sulfur (MoS$_2$) was observed in Cat-GCA3, that is why we can expect lower catalytic activity of Cat-GCA3 in HAS from syngas. TEM was used to examine the morphology and structure of the sulfided catalysts. The morphology of the K-modified CoMoS$_2$

catalysts supported on Al_2O_3 and CCA in high magnification is shown in Fig. 3.3, whereas the catalysts supported on GCA1, GCA2 and GCA3 in lower and higher magnifications are presented in Fig. 3.4.


K-CoMoS$_2$/Al$_2$O$_3$	K-CoMoS$_2$/CCA
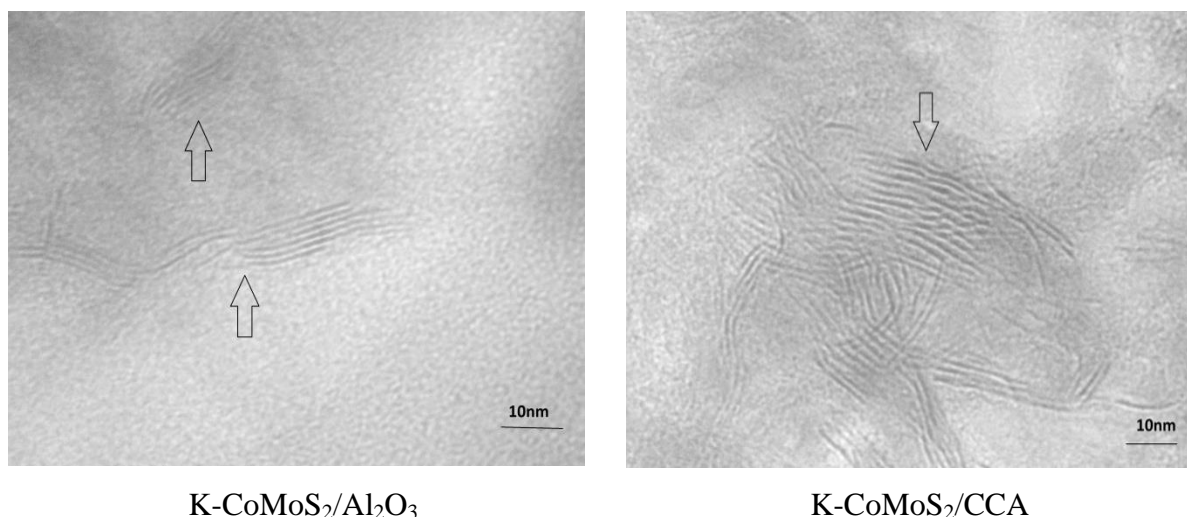
Figure 3.3. TEM images of the K-CoMoS$_2$ catalyst supported on pure alumina and CCA.

Figs. 3.3 and 3.4 show highly dispersed molybdenum disulfide crystallites on various supports clearly visible as threadlike fringes in multilayer particles of the K-CoMoS active phase with different stacking degrees (indicated by arrows and circles in Figs. 3.3 and 3.4). Qualitatively, the stacking degree of Cat-Al_2O_3 increased after coating by amorphous carbon (Fig. 3.3) and graphene nanosheets with different wt. % (Fig. 3.4). Assumingly, the stacking degree of Cat-Al_2O_3 increases because amorphous carbon and graphene are placed between alumina and the K-CoMoS active phase (Fig. 3.5), which weakens the interaction between them. All these factors promote growth of the number of vacancies in the active phase, which decreases adsorption of hydride hydrogen and promotes production of higher alcohols.[12]
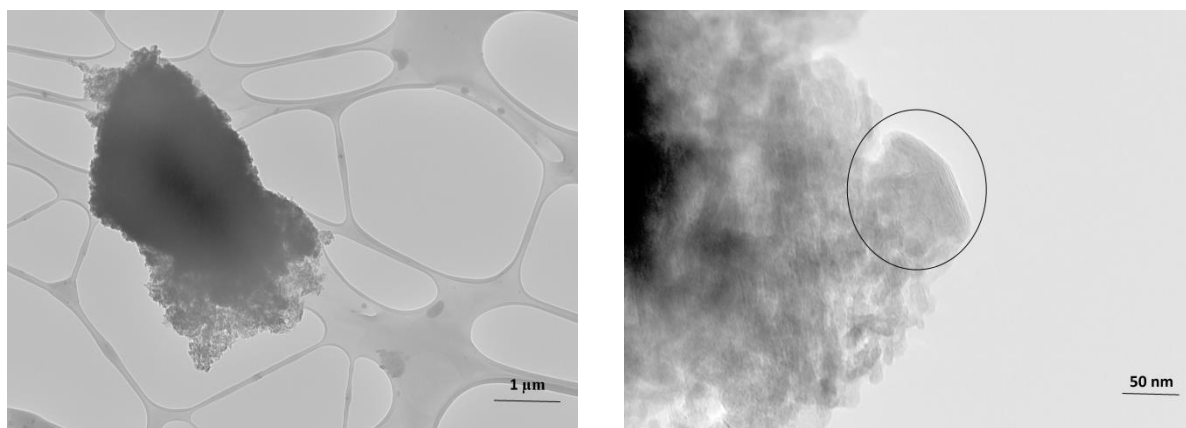
K-CoMoS$_2$-GCA2
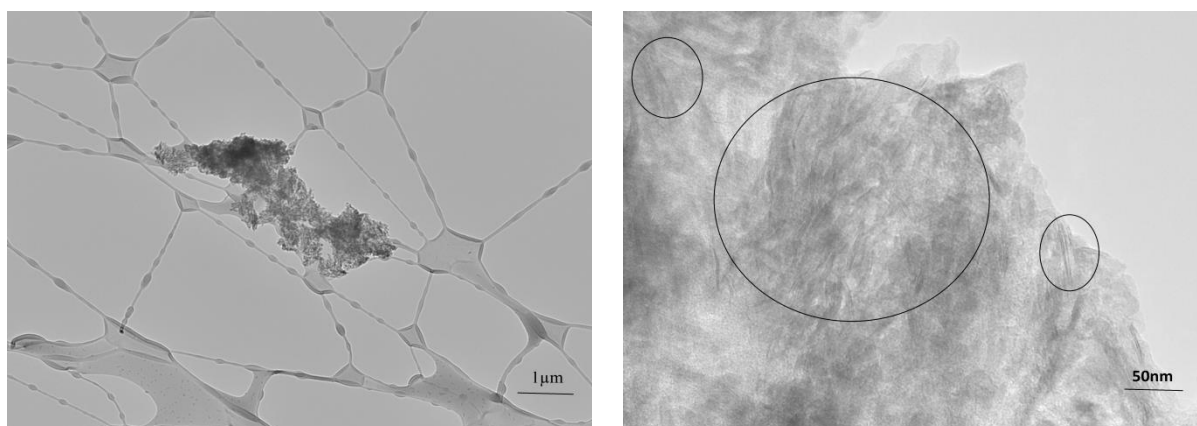
K-CoMoS$_2$-GCA3

Figure 3.4. TEM images of the K-CoMoS$_2$ catalyst supported on GCA1, GCA2 and GCA3 in lower (1µm) and higher magnification (50 nm).
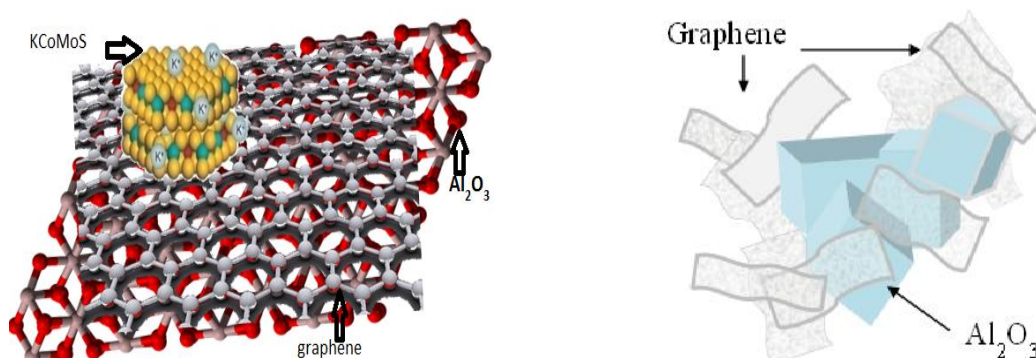
Figure 3.5. Role of graphene in the GCA carrier for conversion of syngas via the K-CoMoS$_2$ catalyst.

We believe that coating of Lewis acid sites of alumina with graphene nanosheets leads to the decrease in the number of the sites favorable for the

production of hydrocarbons. This assumption stems from the fact that acidity of alumina decreased after covering by carbon and graphene (1.7%) (See Fig. 3.6).
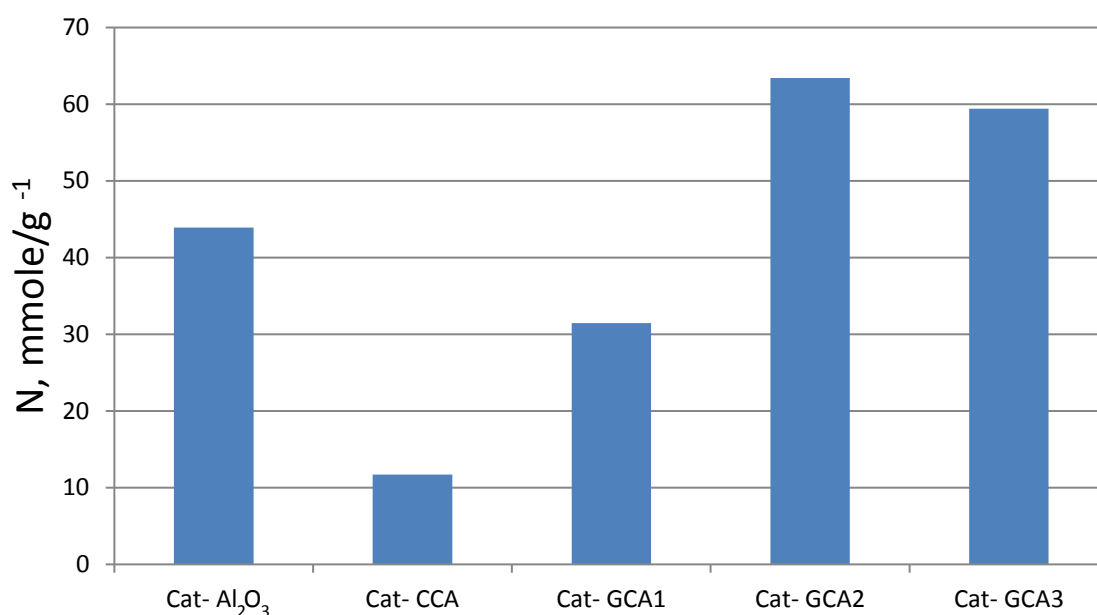
Figure 3.6. Acidity of the catalysts characterized by UV spectra of pyridine adsorption

The TEM images of Cat-GCAs and marked regions at higher magnification (Fig. 3.4) show that graphene layers are ultra-thin. These are similar to the TEM images of pure GCA published by [150]. Moreover, the difference between the TEM images of Cat-GCAs indicates the effect of graphene nanosheets on dispersion of the K-CoMoS active phases. A large black aggregate of species was observed in Cat-GCAs (see the lower magnification images in Fig. 3.4), which may be attributed to the non-homogeneous coating of alumina by graphene nanosheets. The EDX images confirmed uniform dispersion of the K-CoMoS active phase. The observed homogeneously coated catalysts are arranged, depending on results of acidity, in the order: Cat-GCA1 > Cat-GCA2 > Cat-GCA3.

Graphene nano sheets (1.7%) and amorphous carbon (1.7%) covered the Lewis acid sites of alumina (Fig. 3.6). The unexpected increase in the acidity of Cat-GCA2 (1.2 %) and Cat-GCA3 (0.4%) attributed to the acidity of graphene and the heterogeneous coating of alumina that was observed from TEM results. Moreover, the low acidity of Cat-CCA (1.7%) compared with Cat-GCA1 (1.7%) attributes to

the ability of amorphous carbon (CCA) in covering the Lewis acid sites more than graphene nano sheets due to its small thickness.

Catalytic performance of the K-CoMoS$_2$ catalysts supported on Al$_2$O$_3$, CCA (1.7%) and GCA1 (1.7%) at 300, 320, 340, and 360 ^{o}C is illustrated in Figs. 3.7, 3.8, and 3.9. Testing of the catalytic systems used in syngas conversion at 300 - 360 ^{o}C and 5 MPa indicated that amorphous carbon and graphene enhanced catalytic performances of Cat-Al$_2$O$_3$.

All catalysts under study predominantly produced alcohols, especially those containing carbon and graphene, possibly due to the ratio of basal, corner and surface sites of the catalyst, observed in the TEM images, responsible for forming more active sites, which then enhances catalytic activity in HAS. Additionally, the promoter (Co) acts as electron density acceptors on the Sulfur edge of the crystallites, thereby decreasing the hydrogenation reaction and deactivating the sulfur edge, as well as leading to the increased selectivity towards alcohols owing to hydrocarbon. K metals in the active phase also suppress the hydrogenation reaction and increase activity of active sites in charge of alcohol synthesis because they are inserted between the layers of the MoS$_2$ crystallite and increase the stacking number (Maximov et al. 2020; Wang et al. 2017; Badwal et al. 2015).[6, 13, 151] However, the obtained results (Fig. 3.7 a) illustrate a positive correlation between syngas conversion and temperatures (300-360 ^{o}C).
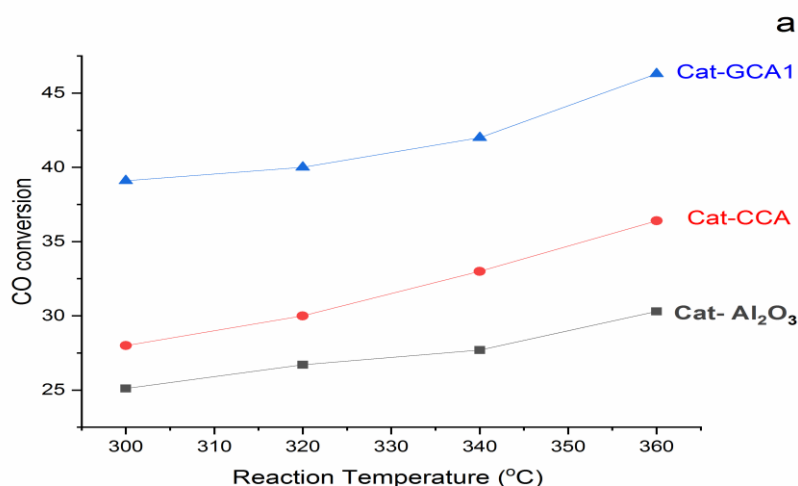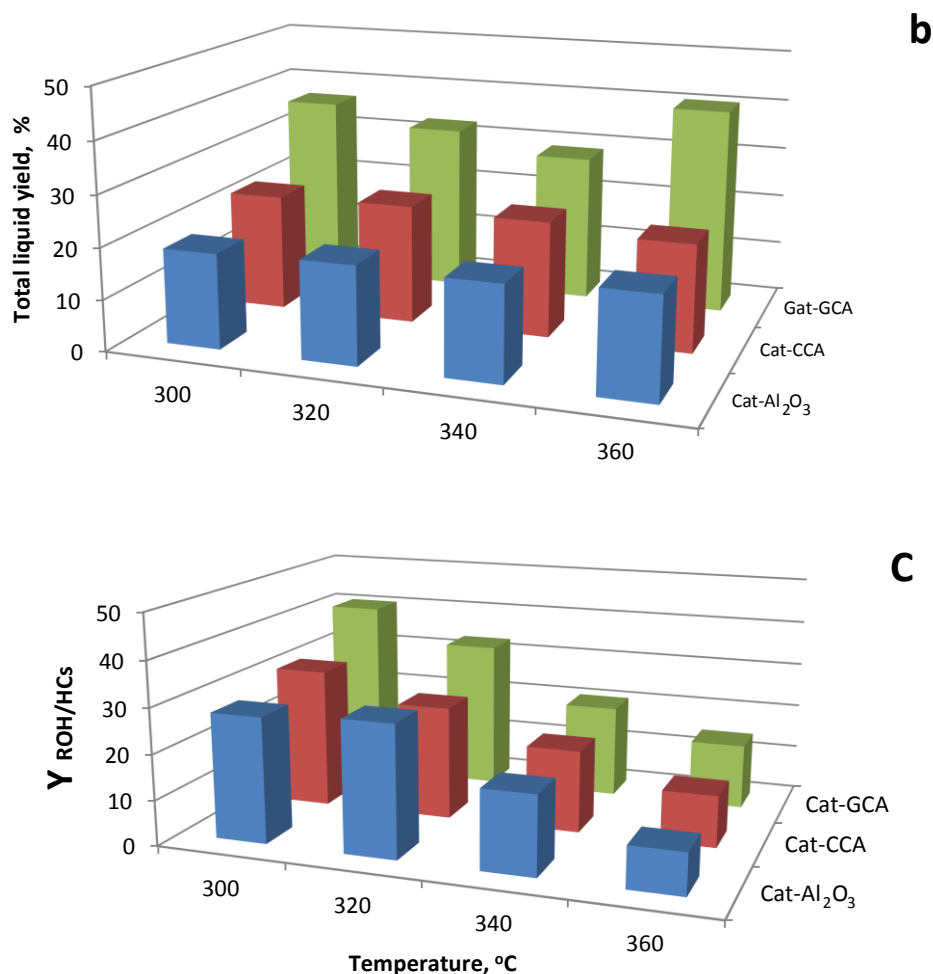
Figure 3.7. Catalytic performance over K-CoMoS$_2$ catalysts supported on Al$_2$O$_3$, CCA (1.7 %) and GCA (1.7%) under the same conditions. *a)* CO conversion; *b)* total liquid yield; *c)* yield ratio between alcohols and hydrocarbons. Reaction conditions: T = 300–360 °C, P = 5 MPa, GHSV = 760 L h^{-1} gcat^{-1}, H$_2$/CO = 1.0.

CO conversion over Cat-Al$_2$O$_3$ increased after alumina covering by amorphous carbon (1.7%) and graphene nanosheets (0.4, 1.2, and 1.7%). It could be due to the important role of carbon and graphene in stabilizing the structure of the K-CoMoS active phase, since the spectroscopic results (Fig. 3.4) and literature data confirm this phenomenon.[114,152-153] Carbon materials placed between alumina and the K-CoMoS active phase (Fig. 3.5) decrease the interaction between them by covering the Lewis acid sites. Higher CO conversion over Cat-GCA1 (1.7 %) compared to Cat-CCA (1.7 %) can be attributed to the characteristics of graphene that exhibits high electron mobility, optical transmittance, and high specific surface area because of its two-dimensional and single-layer uniform structure shaped

from carbon atoms (sp^2-hybridized), with a thickness of 5–7 nm.[114,152-153] These properties of graphene supports lead to the highest dispersion of the K-CoMoS active phase and to the lowest metal-support interaction compared to carbon in Cat-CCA and Cat-Al$_2$O$_3$. Fig 3.7 b also shows a positive correlation between catalytic reaction temperatures and the total liquids yield (TLY) for HAS from syngas. Catalytic activity over K-CoMoS$_2$/sup follows the order of Cat-Al$_2$O$_3$ < Cat-CCA (1.7%) < Cat-GCA1 (1.7%). Moreover, the above characteristics of graphene suppress adsorption of hydride hydrogen and increase activity of the active sites responsible for HAS (basal, corner and surface sites). Fig. 3.7 c shows the ratio between yields of alcohols and hydrocarbons (Y$_{ROH/HCs}$) for Cat-Al$_2$O$_3$, Cat-CCA, and Cat-GCA1. A negative correlation was observed between the yield ratio of alcohols to hydrocarbons and reaction temperatures. This result can be attributed to the positive effect of a higher temperature that increases adsorption of hydride hydrogen, which in turn increases production of hydrocarbons.[154] The yield ratio (Y$_{ROH/HCs}$) increases in the order of Cat-Al$_2$O$_3$ < Cat-CCA (1.7%) < Cat-GCA1 (1.7%). The highest Y$_{ROH/HCs}$ for Cat-GCA1 can be explained by the above characteristics of graphene. Effects of graphene wt. % in graphene coated alumina on catalytic performance over Cat-GCAs are presented in Figs. 3.8 a, b, and c.
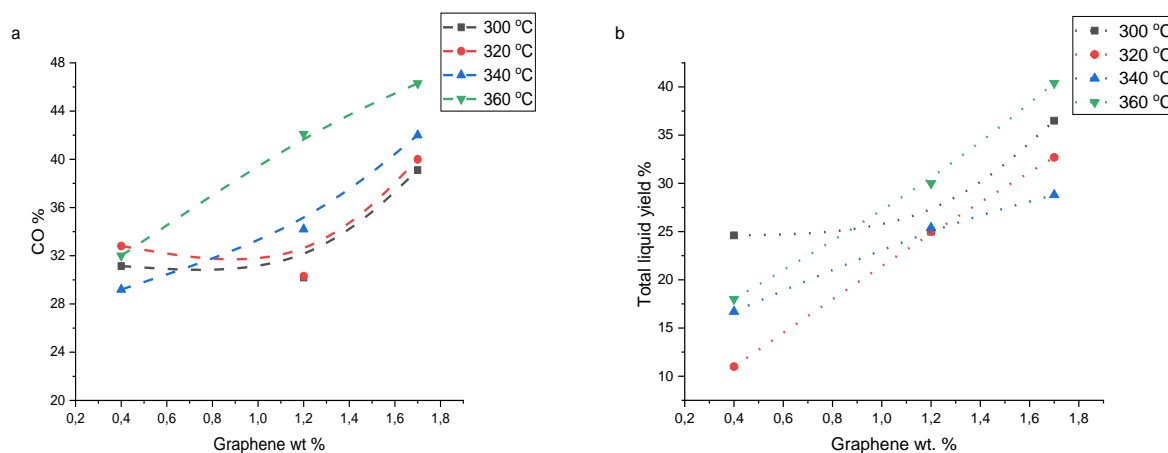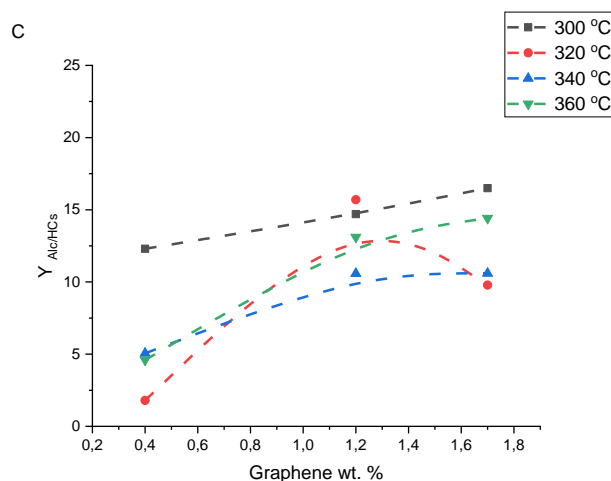
Figure 3.8. Relationship of *a)* CO conversion; *b)* total liquid yield (TLY) and *c)* $Y_{ROH/HCs}$ on wt. % of graphene nanosheets in Cat- GCAs. Reaction conditions: T = 300–360 °C, P = 5 MPa, GHSV = 760 L h^{-1} gcat^{-1}, H_2/CO = 1.0. Catalytic test: Syngas conversion.

The results shown in Fig. 3.8 evidence that the homogeneous coating of alumina by graphene led to the increase in CO conversion: Cat-GCA3 (0.4%) < Cat-GCA2 (1.2%) < Cat-GCA1 (1.7%). Fig. 3.8 b indicates that the highest CO conversion observed over Cat-GCA1 at 360 °C and CO conversion over Cat-GCA2 at 300 and 320 °C are almost the same. TLY % shows a positive correlation with wt. % of graphene at all reaction temperatures, except for 300 °C. TLY % for Cat-GCA2 and Cat-GCA3 is almost the same. The total liquid yield of Cat-GCA1 (Figure 3.7 b) and CO conversion (Figure 3.8 a) decreased at 340 and 320 °C, respectively; this result might be attributed to the slight mutation of active sites during the reactions. This expectation can only be confirmed by tracing the active phase during the reaction by high resolution transmission electron microscopy. The results don't indicate deactivation of the catalysts because the catalysts reactivated again at 360 °C. The yields of alcohols synthesized over Cat-Al$_2$O$_3$, Cat-CCA (1.7%) and Cat-GCA1 (1.7%) are given in Fig. 3.9.
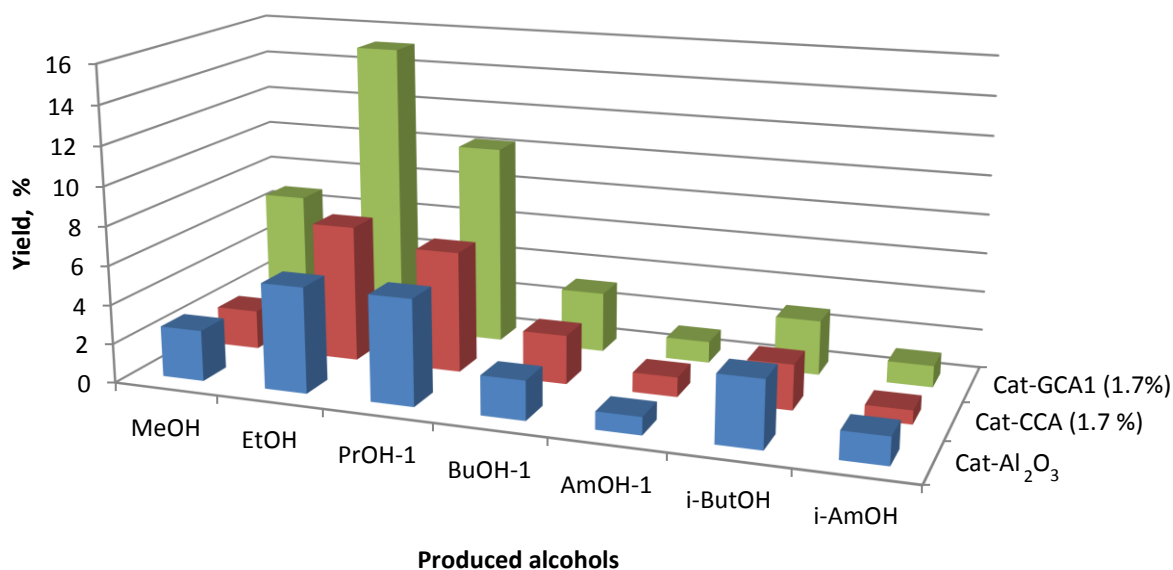
Figure 3.9. Alcohols distribution over the Cat-Al$_2$O$_3$, Cat-CCA (1.7%) and Cat-GCA (1.7%) catalysts at 360 ^{o}C. Time of reaction = 16h.

The extent of distribution of the synthesized alcohols from syngas over the supported-K-CoMoS$_2$ catalysts is important and depends on various factors: (i) ratios between K, Co, and Mo; (ii) nature of carriers; (iii) reaction conditions; (iv) type of HAS bed reactor, including the height and radius. From Fig. 7, it is quite obvious that the liquid products generated by Cat-Al$_2$O$_3$, Cat-CCA and Cat-GCAs consist mostly of methanol, ethanol, propanol-1, butanol-1, amylalcohol-1, iso-butanol, and iso-amylalcohol. Ethanol, propanol-1, methanol, and iso-butanol were predominant alcohols in the collected liquids and the byproducts comprised mainly amylalcohol-1 and iso-amylalcohol. Propanol-2 and butanol-2 were not produced over all the supported catalysts under study in all reaction conditions. Coating of alumina by graphene nanosheets improved the yield of all synthesized linear alcohols. Also, the yield of ethanol, propanol-1 and amylalcohol-1 increased after coating of alumina by amorphous carbon. In contrast, coating of alumina by amorphous carbon (1.7%) decreased the yield of methanol, iso-butanol, and iso-amylalcohol. The behavior of Cat-CCA towards iso-butanol and iso-amylalcohol is related to the lowest acidity of Cat-CCA (see Fig.3.6) because the isomerization occurs on the acid sites of the catalyst. Increasing the yield of ethanol and

propanol-1 with a small amount of methanol (toxic) is considered as an important result and has commercial benefits since this mixture can be used directly as a fuel or octane number improver. Nowadays, the majority of engines can run with at least 10% ethanol added into the fuel (E10).[2, 4, 88] In many regions of the world, it is permitted to use a blend of a mixture of alcohols (C1 - C10) (BP < 210°C) with gasoline. The methanol content must be low due to its toxicity. The dependence of alcohols distribution over Cat-GCAs catalysts on the weight percentage of graphene nanosheets is shown in Fig. 3.10.
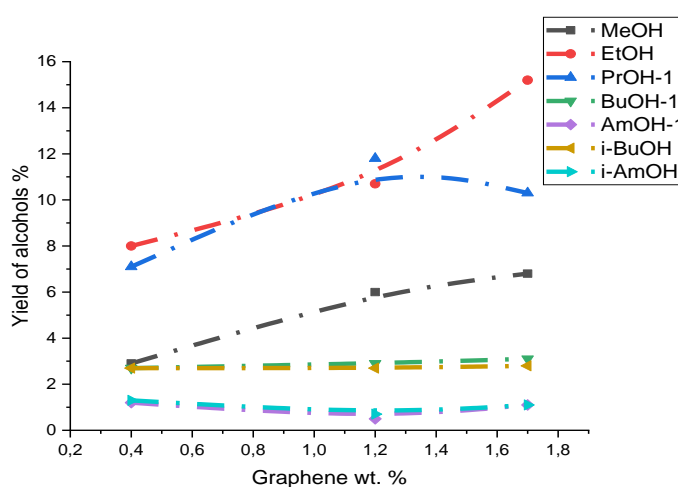
Figure 3.10. Dependence of alcohols distribution on wt. % of graphene in Cat-GCAs at 360 °C. Time of reaction = 16h.

The yield of ethanol from syngas shows a positive correlation with graphene wt. % in GCA (Fig. 3.10). Cat-GCA2 (1.2 %) has optimum wt. % of graphene for producing all alcohols, except for ethanol. This result can be explained by the micropore structures of GCA2 compared to counterparts. Such characteristics contribute to the formation of sites favorable for HAS (this phenomenon with more details will be discussed in section 3.2). Over Cat-GCA2, the yield of propanol-1 was found to be higher than that of ethanol. Yields of $C_{4+}OH$ (butanol-1 and iso-butanol) and $C_{5+}OH$ were not affected by the increase in wt. % of graphene in GCA. The methanol yield slightly increased between 1.2 and 1.7% of graphene. There is a controversy in the enhancement of the $C_{3+}OH$ yield from synthesis gas over K-modified $CoMoS_2$ catalysts. A series of unsupported K-modified $CoMoS_2$

catalysts with various Cobalt content to investigate the role of Co in the synthesis of $C_{3+}OH$ from syngas were studied.[102] The highest alcohol selectivity (47.1%) was found with a Co/(Co+Mo) molar ratio of 0.13. We expect the yield of C_{3+} alcohol to improve if the same molar ratio of cobalt supported on GCA2 (1.2 %) is used. The selectivity (Free CO_2) towards C_{1+}, C_{2+} and alcohols from syngas test is presented in Fig. 3.11.
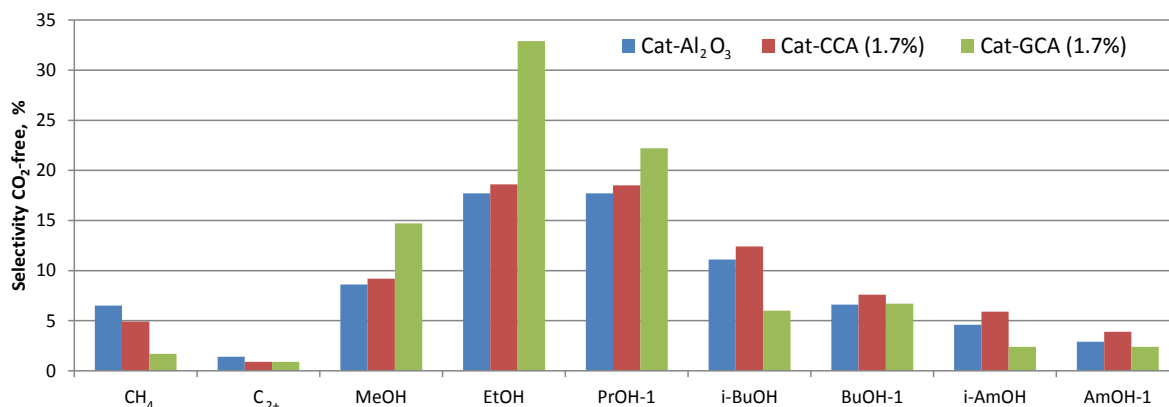
Figure 3.11 Selectivity of C_{1+}, C_{2+} and different alcohols (CO_2 excluded) for Cat-Al₂O₃, Cat-CCA (1.7%), and Cat-GCA (1.7%). Reaction conditions: T = 360 °C, P = 5.0 MPa, CO: H₂: Ar = 45:45:10 gas at 760 L h⁻¹·g cat⁻¹, catalyst loading 3 grams. Time of reaction = 16h.

The selectivity was calculated in the CO_2-free basis approximation since the CO_2 byproduct is mainly formed by the WGS.[6] In the present study, the selectivity for linear primary alcohols over Cat-Al₂O₃ enhanced when alumina was coated by carbon and graphene nanosheets (Fig. 3.11) and, otherwise, the selectivity of C_{1+} and C_{2+} over Cat-Al₂O₃ decreased. These results can be explained by the decrease of the interaction between alumina and the K-CoMoS active phase due to the intermediate carbon layer inhibiting hydride hydrogen adsorption. GCAs were found to act better than CCA in increasing the selectivity for linear primary alcohols and decreasing the selectivity for light hydrocarbons. Linear primary alcohols are synthesized by carbon monoxide insertion,[102] whereas branched alcohols are prepared by CHx β-addition and CO insertion. The selectivity of supported K-CoMoS₂ catalysts for iso-alcohol follows the order of Cat-GCA < Cat-Al₂O₃ < Cat-CCA. Graphene nanosheets exhibited opposite behavior with respect to iso-alcohols because graphene nanosheet supported catalysts did not

form a surface favorable for CHx β-addition compared to CCA and Al_2O_3. Furthermore, the selectivity for n-propanol ranks directly after ethanol over all supported catalysts because it was formed by both routes (CHx β-addition and CO insertion). From Fig. 3.11, the selectivity for C_{1+} was found to be higher than for C_{2+} over supported-$CoMoS_2$ catalysts because $C_2H_5^+$ species tend to follow the pathway of alcohol more than CH_3^+. Linear secondary alcohols such as propanol-2 and butanol-2 were not observed in contrast to the literature results.[6,9,114] The dependences of selectivity of linear and branched alcohols, as well as light hydrocarbons on graphene weight % are shown in Fig. 3.12.
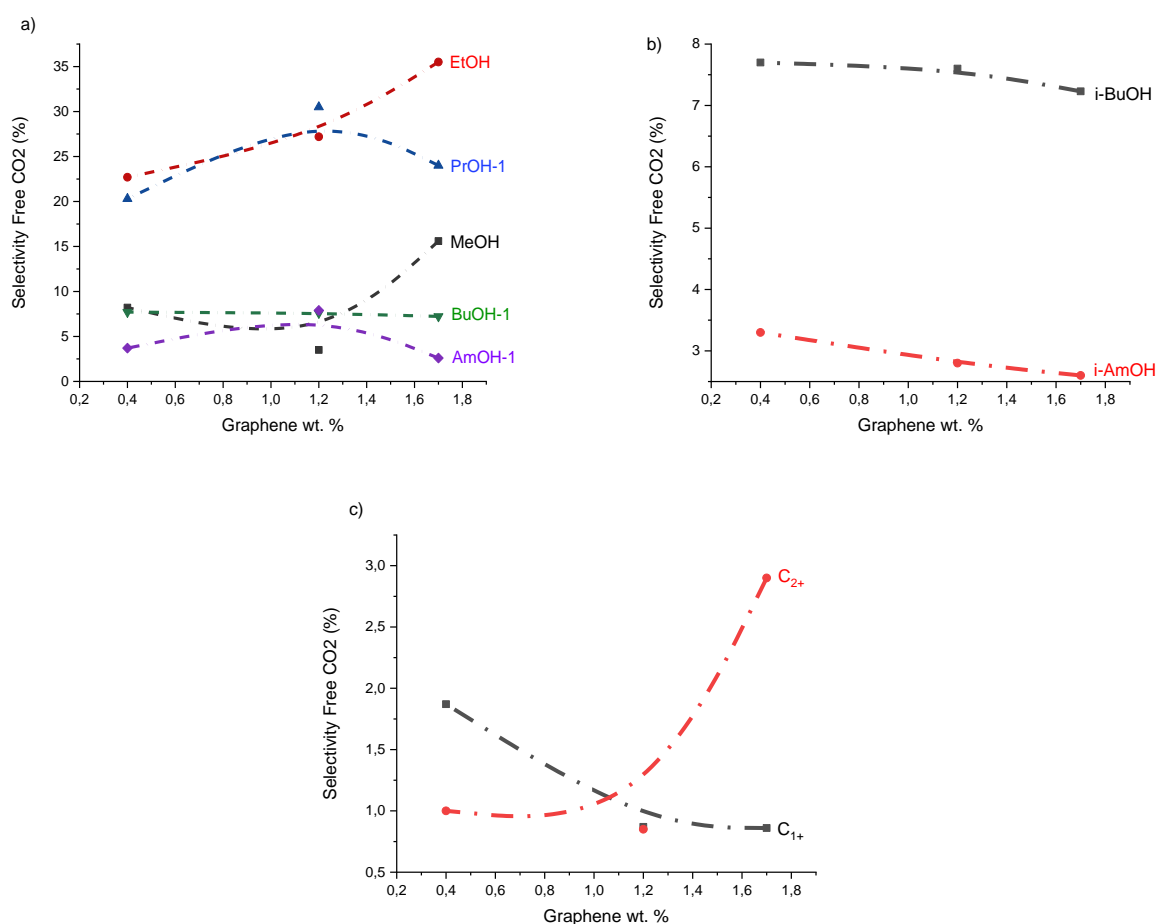
Figure 3.12. Dependence of the selectivity (CO_2 excluded) for *a)* linear alcohols; *b)* iso-alcohols; *c)* light hydrocarbons on wt. % of graphene in GCA. Reaction conditions: T = 360 °C, P = 5.0 MPa, CO: H_2: Ar = 45:45:10 gas at 760 L ·h^{-1}·$gcat^{-1}$, catalyst loading 3 grams. Time of reaction = 16h.

The selectivity for low chain linear alcohols (methanol and ethanol) dramatically increased with the increase in graphene weight %, whereas propanol-1 and amyl alcohol-1 showed the opposite trend (Fig. 3.12 a). The selectivity for butanol-1 did not change as function of graphene wt. %. A negative correlation between graphene wt. % and selectivity for the detected iso-alcohols (iso-butanol and isoamyl alcohol) was observed (Fig. 3.12 b). Nonetheless, the selectivity for C_{1+} showed a negative correlation with graphene wt. % contrary to C_{2+} (Fig. 12 c). The selectivity towards ethanol decreased in the order of Cat-GCA1 > Cat-GCA2 > Cat-GCA3. Cat-GCA2 exhibited the highest selectivity for propanol-1. whereas the abnormal selectivity of Cat-GCA2 towards propanol-1 and amyl alcohol-1 (Fig. 3.12) can be explained by the micropore structures on the surface of the catalyst. The results confirm the validity of our unusual finding in section 3.2: microporous supported K-CoMoS$_2$ catalysts are more active than mesoporous ones. A few published studies reported the benefits of the coating of alumina by carbons as a catalyst support for molybdenum oxide[102,155-156] and sulfided forms[114,157] in syngas conversion, Fischer-Tropsch and hydrodesulfurization reactions. The authors suggest that a combination of physical and chemical properties of both supports will produce higher quality supports since alumina retains its advantage as the main carrier for commercial heterogeneous catalytic systems due to several characteristics: (i) high packed density; (ii) developed surface, (iii) stability at high temperature and pressure; (iv) durability. So, it is advisable to combine the positive properties of both supports. That is why graphene-coated alumina was synthesized as a carrier for K-CoMoS$_2$ catalysts with a view to find a solution to the large thickness of amorphous carbon, which may fail to form a homogenous uniform coating of Lewis acid sites of alumina and accelerate hydrogenation. It is notable to mention that carbon coated alumina materials were studied previously for several applications as catalysts or catalyst supports. However, graphene nanosheets used as intermediate carbon supports to improve HAS from syngas have not been studied yet.

The GCA1 catalysts are characterized by a higher stacking number and slab length compared to the Al_2O_3 and CCA samples (Table 3.3 and 3.4). These results attribute to the weak interaction between active phase and GCA1 support. The relative content of mono- and bi-layered crystallites increases in order Cat-Al_2O_3 < Cat-CCA < Cat- GCA1. Whereas, the content of 3, 4, 5, and 6, and 7 stacked slabs of Cat-GCA1 were found to be higher comparing with the counterparts.

Table 3.3. Distributions of stacking number of MoS_2 particles

Stacking Number		1	2	3	4	5	6	7	8
Relative content, %	Cat-Al_2O_3	43.5	43.5	10.9	1.7	0.3	0.0	0.0	0.0
	Cat-CCA	39.2	36.9	18.4	1.7	1.1	1.8	0.7	0.3
	Cat-GCA1	37.6	35.0	20.0	2.4	0.8	2.0	1.4	0.8

Table 3.4. Distribution of MoS_2 slabs by length

Particle length		<2	2…4	4…6	6…8	8…10	> 10
Relative content, %	Cat-Al_2O_3	1.0	29.8	45.7	17.2	4.6	1.7
	Cat-CCA	0.5	23.6	38.4	20.4	9.5	7.7
	Cat-GCA1	0.3	18.2	39.4	22.8	10.8	8.5

The Cat-CCA and Cat-GCA1 show high content of 8-stacked slabs. The highest content of particle length more than 10 nm has been observed for Cat-GCA1. The observed catalytic performance of Cat-GCA1 explains by "Rim-Edge" model.[158] According to the model, changing the height/diameter ratio of the crystallite controls the relative quantity of active sites and consequently affects catalytic performance. Carbon and graphene coated alumina based catalysts contained a higher proportion of multilayered (CoMoS-II) phase comparing with Cat-Al_2O_3 that attributed to active support-phase interaction. Thus, increasing the crystallites' linear dimension and stacking number resulted in an increase in catalytic performance because this morphologies contain higher ratio of basal, corner and surface sites of the catalyst which are promote HAS as well as ethanol conversion to other oxygenates.

3.2. Effect of textural characteristics on the catalytic performance of supported-K-CoMoS$_2$ in higher alcohols synthesis from syngas

The influence of textural characteristics on the catalytic performance of sup-K-CoMoS$_2$ catalysts was studied using four types of supports: mesoporous materials (Al$_2$O$_3$ and CCA) and microporous powder activated carbons (AG-3 and BAW) to provide essential information for the design of better catalysts for higher alcohols synthesis (C1 - C5) from syngas.

Elemental analysis data are presented in Table 3.5. The molybdenum content in the samples varies from 14 to 16 % wt.

Table 3.5. Composition of prepared catalysts

Catalyst	Content (wt. %)			Molar ratio	
	Mo	K	Co	r*	t**
K-CoMoS$_2$/Al$_2$O$_3$	15.8	10.2	5.1	0.34	1.03
K-CoMoS$_2$/CCA	14.4	11.6	4.7	0.34	1.30
K-CoMoS$_2$/AG-3	14.9	12.3	5.7	0.39	1.24
K-CoMoS$_2$/BAW	14.8	12.0	5.2	0.36	1.27
r* = Me/(Me+Mo) molar ratio t** = K/(Me+Mo) molar ratio					

The promotion degree r = Me/(Mo+Me) [molar ratio] ranges from 0.34 to 0.39. The modification degree t = K/(Me+Mo) [molar ratio] ranges from 1.03 to 1.30. The detected ratios between Co and Mo were found to be similar to the optimum ratio for HAS in literature under the same reaction conditions and very closed to the targeted contents. Textural characteristics of supports and supported catalysts are shown in Table 3.6.

Table 3.6. Textural characteristics of supports and catalysts

Sample	S_{total}	S_{micro}	S_{meso}*	V_{total}	V_{micro}	V_{meso}**
	m^2/g	m^2/g	m^2/g	cm^3/g	cm^3/g	cm^3/g
Al_2O_3	161	0	161	0.65	0.00	0.65
$K-CoMoS_2/Al_2O_3$	91	0	91	0.29	0.00	0.29
CCA	156	13	143	0.63	0.01	0.63
$K-CoMoS_2/CCA$	73	0	73	0.26	0.00	0.26
AG-3	854	753	101	0.45	0.35	0.10
$K-CoMoS_2/AG-3$	164	137	27	0.09	0.06	0.03
BAW	753	642	111	0.39	0.26	0.13
$K-CoMoS_2/BAW$	404	365	40	0.23	0.16	0.07
S_{meso}* = S_{total} - S_{micro};						
V_{meso}** = V_{total} - V_{micro}						

Table 3.6 shows the specific surface area (S_{total}) of the support materials increases in the order CCA < Al_2O_3 < BAW < AG-3 and total pore volume decreases in the order $Al_2O_3 \geq$ CCA > AG-3 > BAW. Alumina does not contain micropores at all, and the specific surface area for the micropores of the other supports increases in the order Al_2O_3 < CCA < BAW < AG-3. The micropore volume increases in the order CCA < AG-3 < BAW. The Al_2O_3 and CCA contain almost only mesopores (pore diameter: 4 - 50 nm), whereas AG-3 and BAW mainly contain micropores. Loading the sulfides onto the support materials leads to a significant decrease in pore surface and volume for all catalysts. The N_2 adsorption/desorption isotherms for the support materials and the supported K-$CoMoS_2$ are shown in Fig. 3.13.
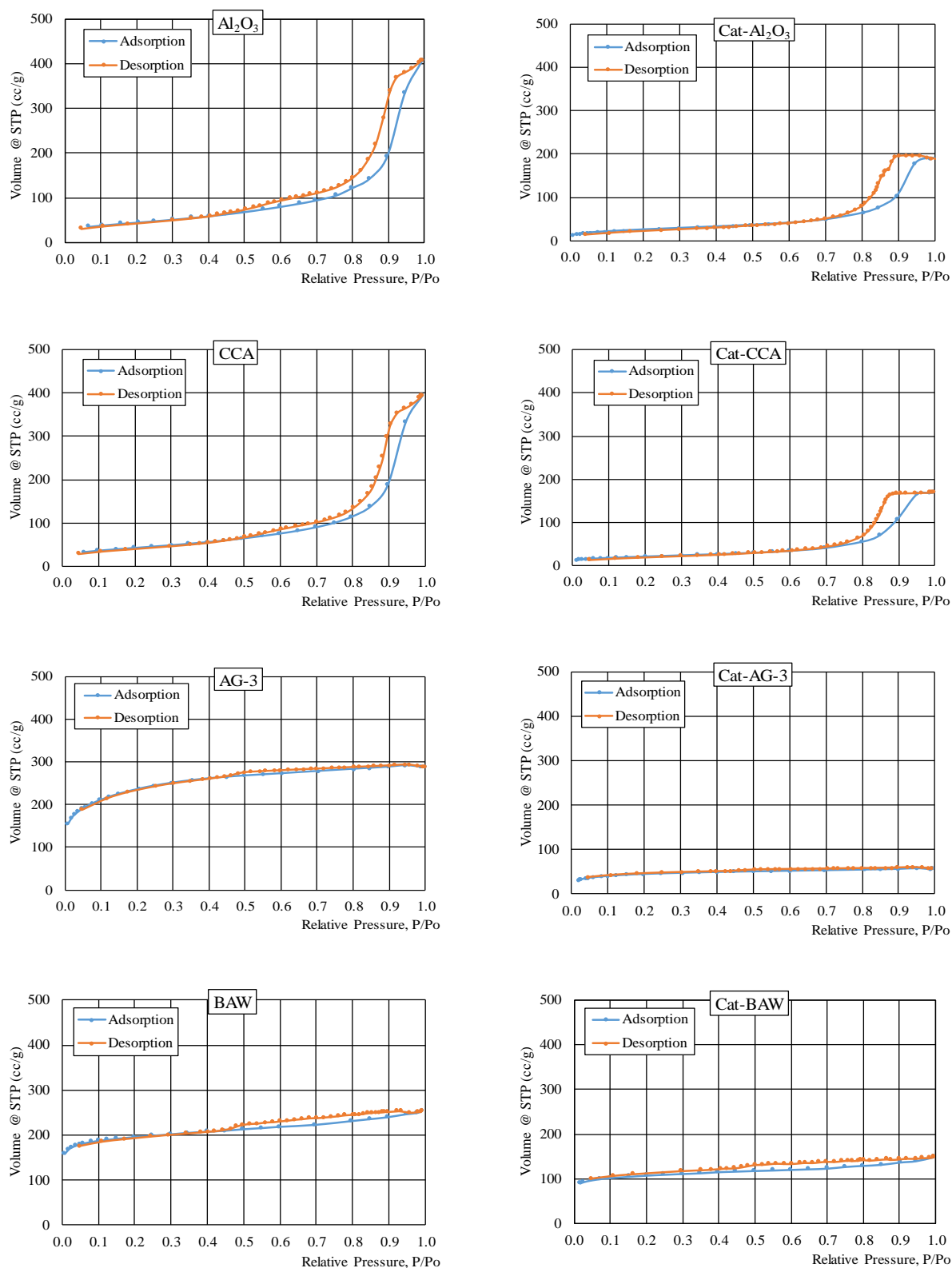
**Figure 3.13.** N$_2$ adsorption-desorption isotherms for Al$_2$O$_3$, CCA, AG-3, BAW carriers and corresponding K-CoMoS$_2$ supported catalysts. Catalytic samples abbreviated as Cat-carrier (Carrier = Al$_2$O$_3$, CCA, AG-3, BAW).

The alumina-based supports (Al_2O_3 and CCA) showed N_2 uptake limitation at high values of relative pressures (P/P_0) and typical curves for type IV adsorption isotherms with H1 type hysteresis.[146] This type of isotherm is typical for mesoporous samples with capillary condensation inside the mesopores. H1 type hysteresis is attributed to materials consisting of agglomerates with narrow pore size distribution. Agglomerate is defined as an assemblage of particles rigidly joined together and an aggregate as an assemblage of particles which are loosely coherent. Adsorption isotherms for the activated carbons (AG-3 and BAW) differ significantly from those for the alumina-based support materials. AG-3 exhibited high uptake even at low relative pressures, (P/P_0 0.1-0.2) and a type I isotherm with H4 type hysteresis, typical for microporous material. BAW shows a type II isotherm with H4 type hysteresis. The horizontal plateau at high relative pressure values ($P/P_0 \sim 0.9 - 1$) indicates a large amount of micropores with narrow pore size distribution. H4 type hysteresis is often associated with narrow slit-like pores.

Cat-Al_2O_3 and Cat-CCA showed type H_2 hysteresis. This type of hysteresis is explained by difference of N_2 adsorption/desorption mechanisms that take place in wide pores with a narrow neck ('ink bottle' pores). The observed tails (low pressure hysteresis) in isotherms of the catalysts indicate either interaction of adsorbate molecules (N_2) with the catalyst surface, or existence of pores of the sizes comparable to the adsorbate molecule size. For active carbon supported catalysts, the presence of the active phase affects neither the isotherm nor the hysteresis type, but it does decrease the surface area and pore volume.

Qualitatively, the adsorption isotherms for our activated carbon-based microporous materials and corresponding catalysts, with their typical inflection points, are very similar to those for analogous microporous materials presented in Fig. 1 and 2 of.[10] Loading of the support material with the active phase reduces both specific surface area and pore volume (Fig. 3.14 a, b).
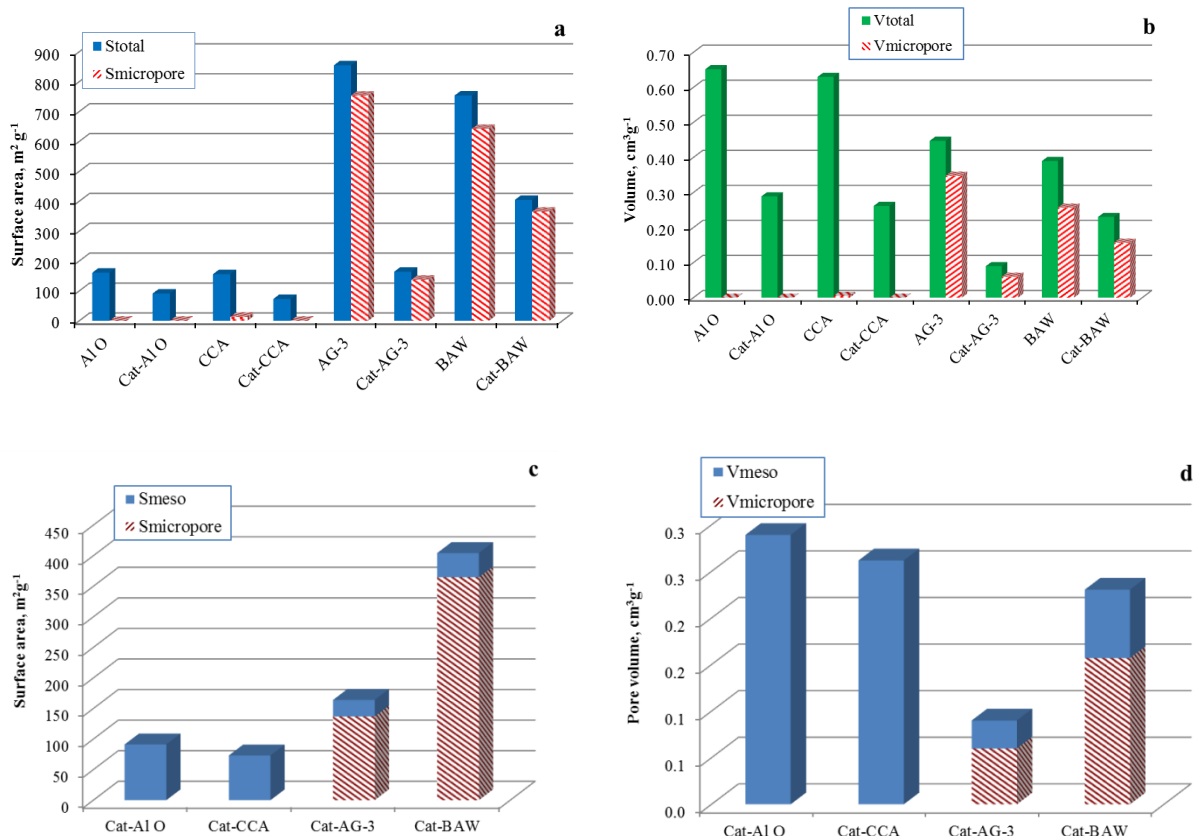
Figure 3.14. Specific surface areas of all the pores (S_{total}) and micropores ($S_{micropore}$) (*a*); total pore volume (V_{total}) and micropores volume ($V_{micropore}$) (*b*); distribution of macro + mesopores and micropores in the K-CoMoS$_2$ catalysts supported on different carriers (Cat-carrier) for specific surface area (S_{meso}, $S_{micropore}$) (*c*) and for pore volume (V_{meso}, $V_{micropore}$) (*d*). The plots are color-coded.

The ratio between micro- and mesopores of the investigated catalysts is clearly seen from Fig. 3.14, where Fig. 3.14 c and d show the surface area and pore volume of micro- and mesopores, respectively.

The SEM images of the supports and supported catalysts are shown in Fig. 3.15 Additional images are show in Figs 3.16, 3.17, and 3.18.

Support name	SEM image of support	SEM image of supported-K-CoMoS$_2$ catalyst
Al$_2$O$_3$		
CCA		
AG-3		
BAW		
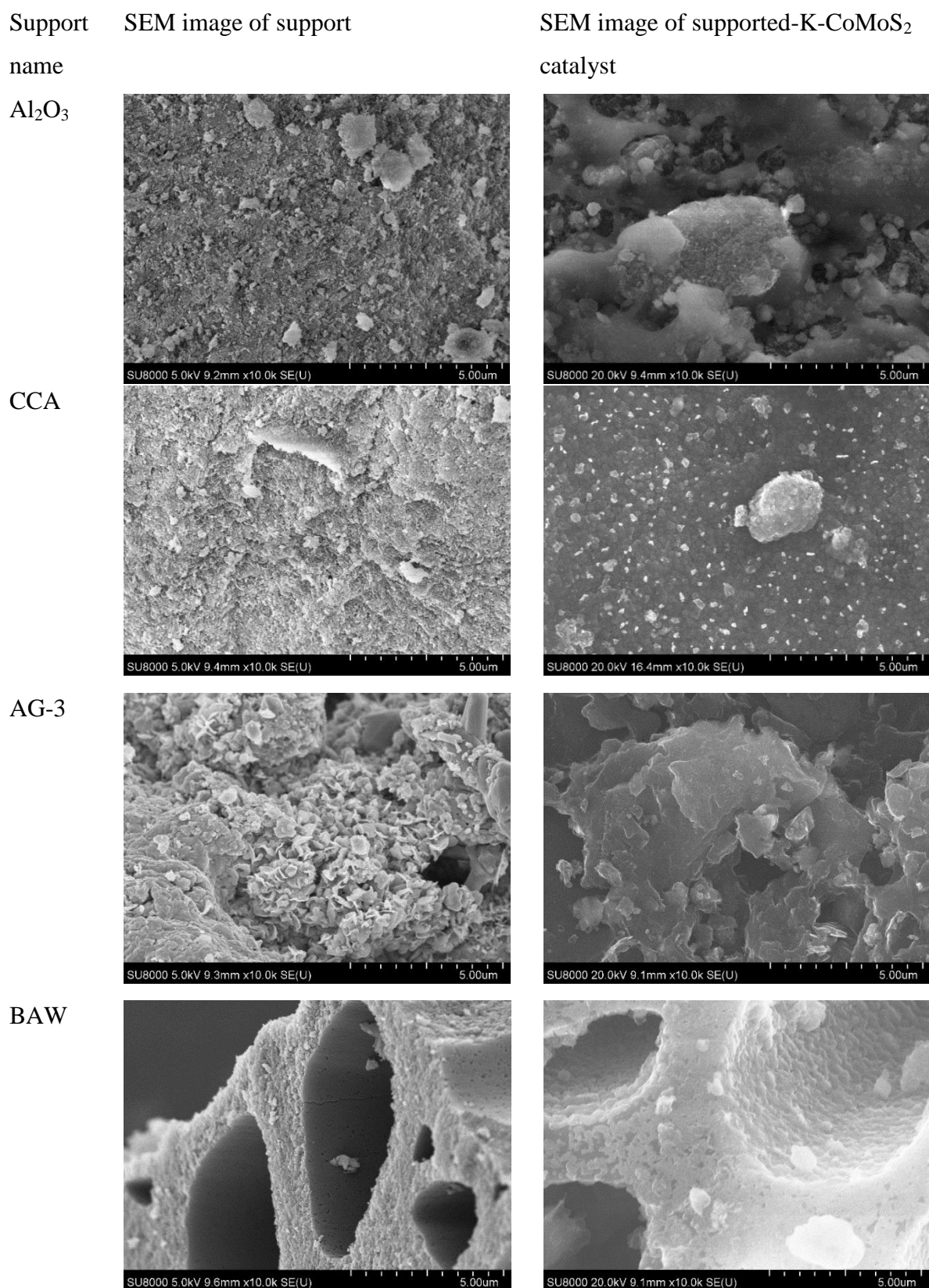
Figure 3.15. SEM images of supports and supported K-CoMoS$_2$ catalysts

Cat-Al₂O₃

Cat-CCA

Cat-CCA
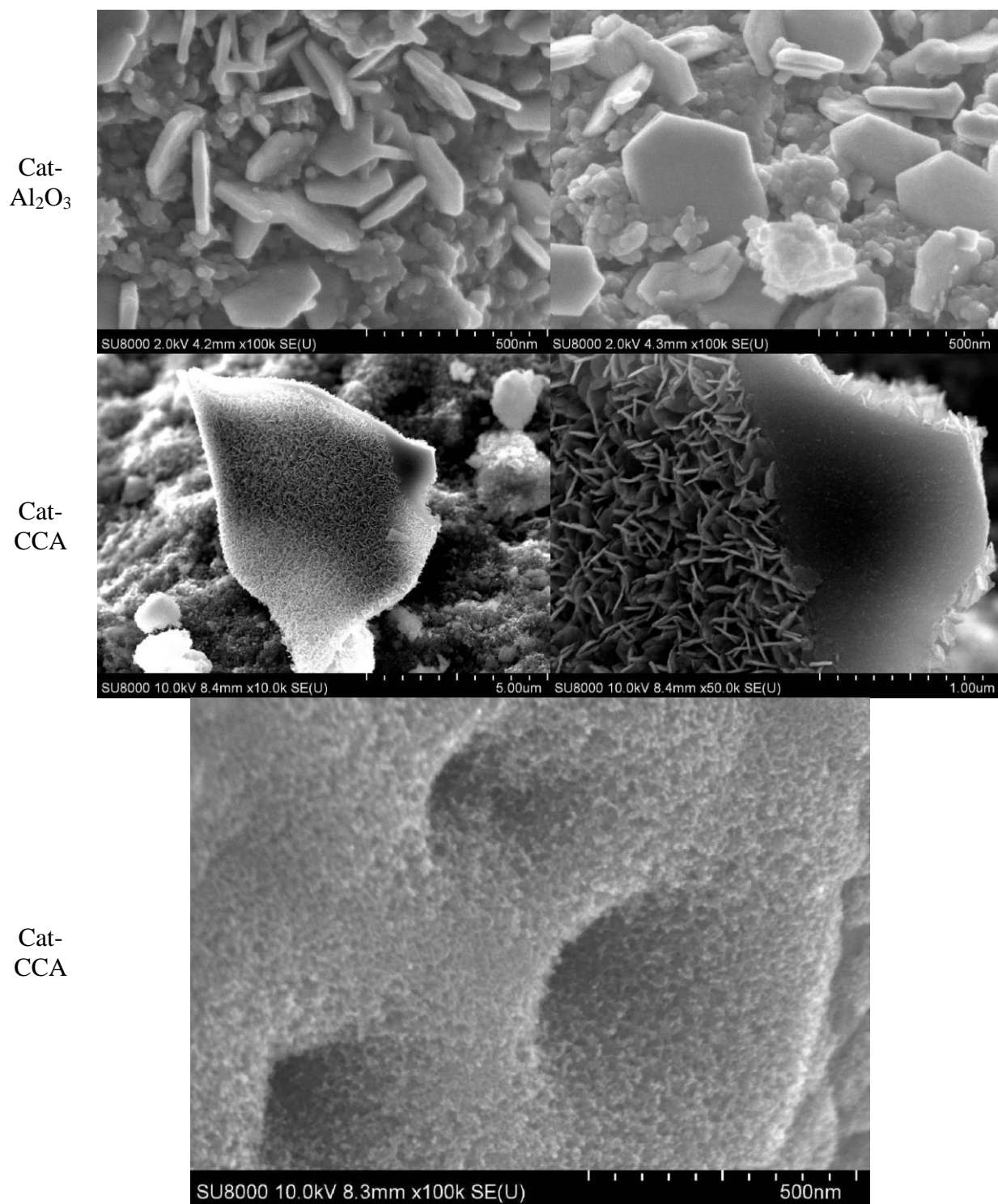
Figure 3.16. SEM images of giant agglomerations of K-CoMoS₂ crystallites supported on mesoporous Al₂O₃ and CCA.
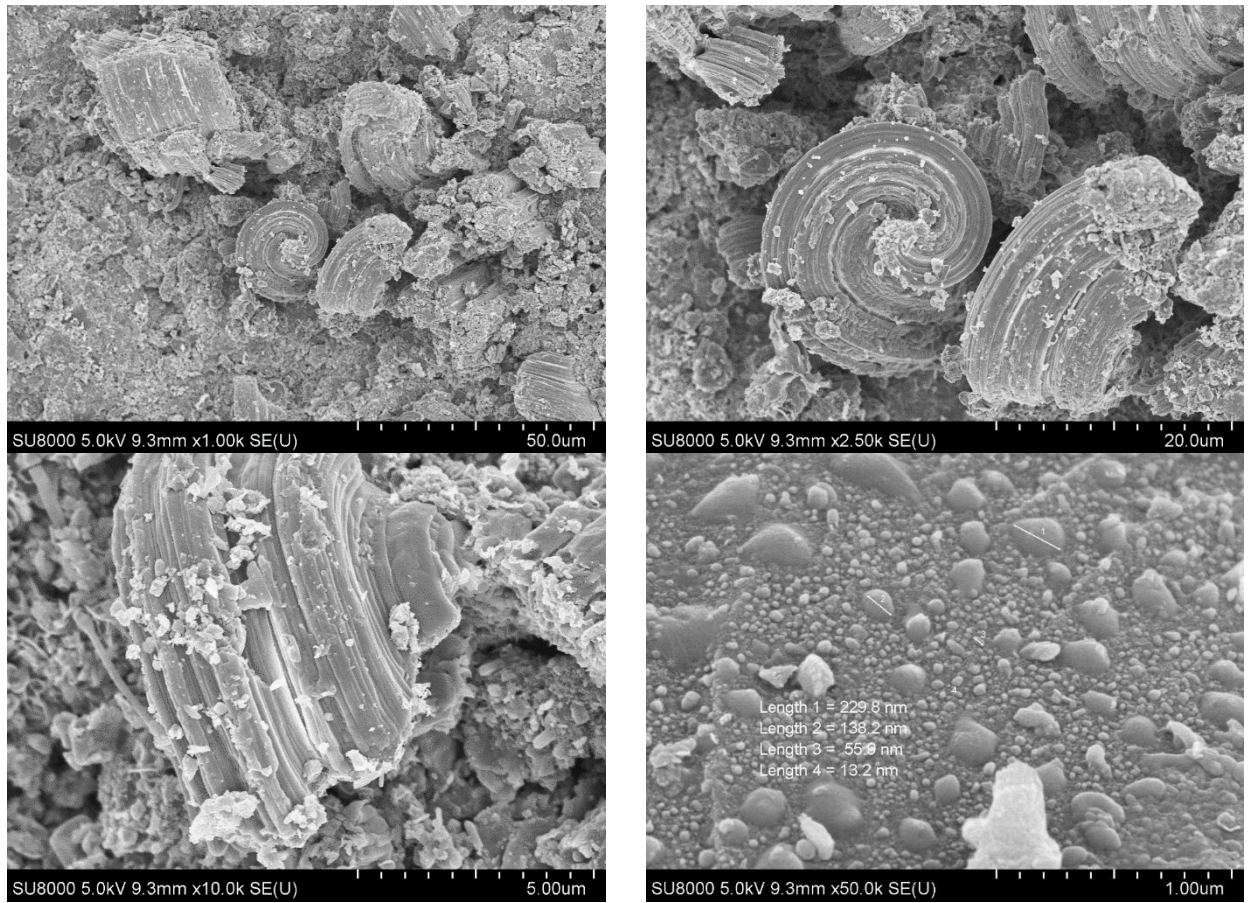
Figure 3.17. SEM images of the AG-3 support.

2.
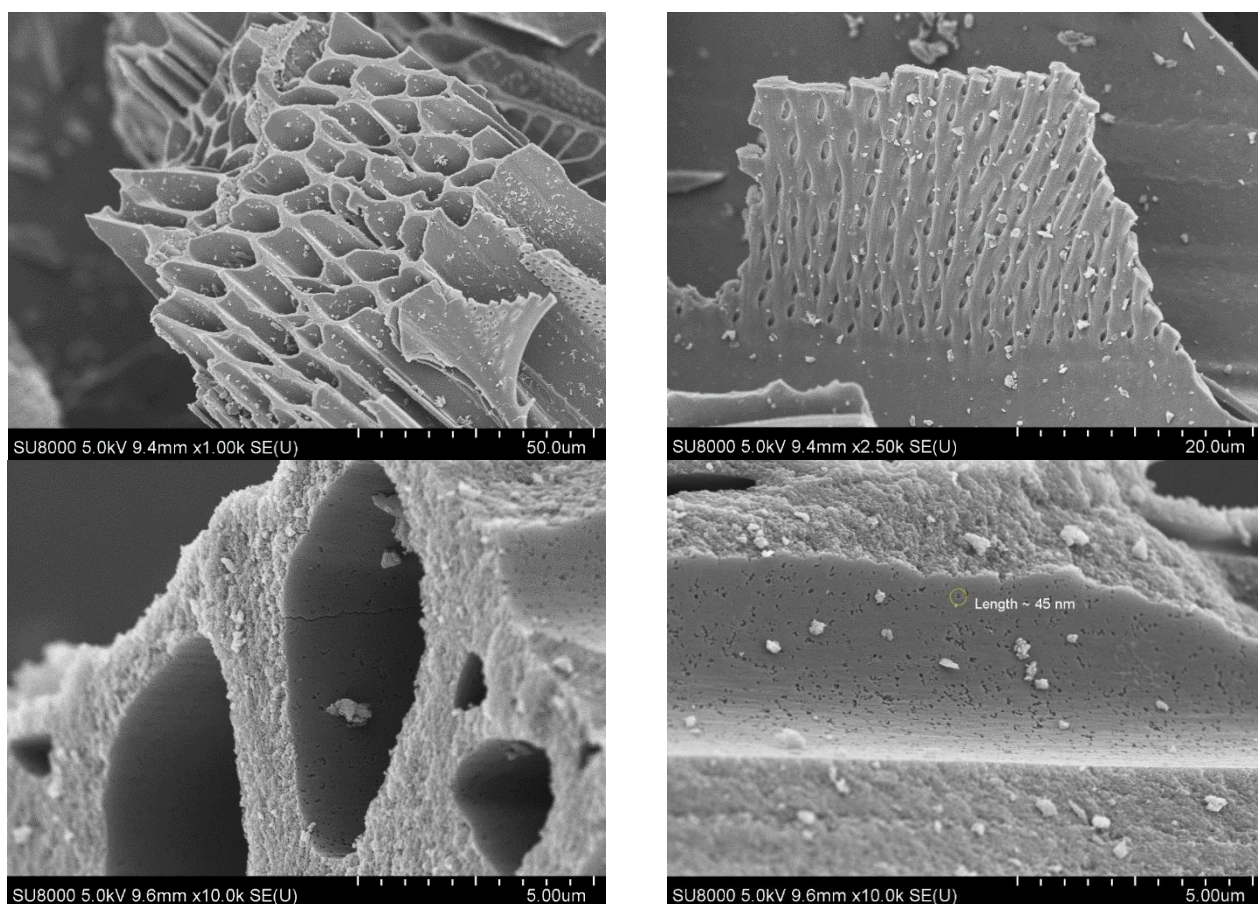
Figure 3.18. SEM images of the BAW support.

The SEM image of the alumina support shows multiple fine particles with some larger agglomerates. During coating with carbon, the surface is smoothed out and larger features become more visible. In both cases, the surface of the prepared catalyst is dominated by a smooth gel-like phase with dotted fine particles and a few large nano crystal agglomerates. The observed particles are significantly larger than in the original alumina. The AG-3 sample consists of numerous small platelets dotted with small holes. The platelets form fairly large agglomerates with pores between them. The platelets in the prepared catalyst are not visible, the surface is smooth, and no crystalline particles are visible. Only larger pores are observed. The BAW support inherited from the parent timber rather large cylindrical pores with relatively smooth walls. The cylinder walls are dotted with small holes. Macropores are embedded in a microporous matrix with an irregular cross-section. During the catalyst preparation, the rough cross-section is replaced by the smooth surface and the walls of the large channel become uneven. In all cases, crystallites

of the active phase are small (normally below 5nm) and can be observed only at high magnification.[91]

The surface morphology of AG-3 is typical for activated carbons,[10,15] showing wide developed surface with pores partially covered by fine layers of carbon. BAW shows a well-ordered macro channel structure. Representative HRTEM images of the catalysts under study are shown in Fig. 3.19.

K-CoMoS$_2$/Al$_2$O$_3$

K-CoMoS$_2$/CCA

K-CoMoS$_2$/AG-3

K-CoMoS$_2$/BAW
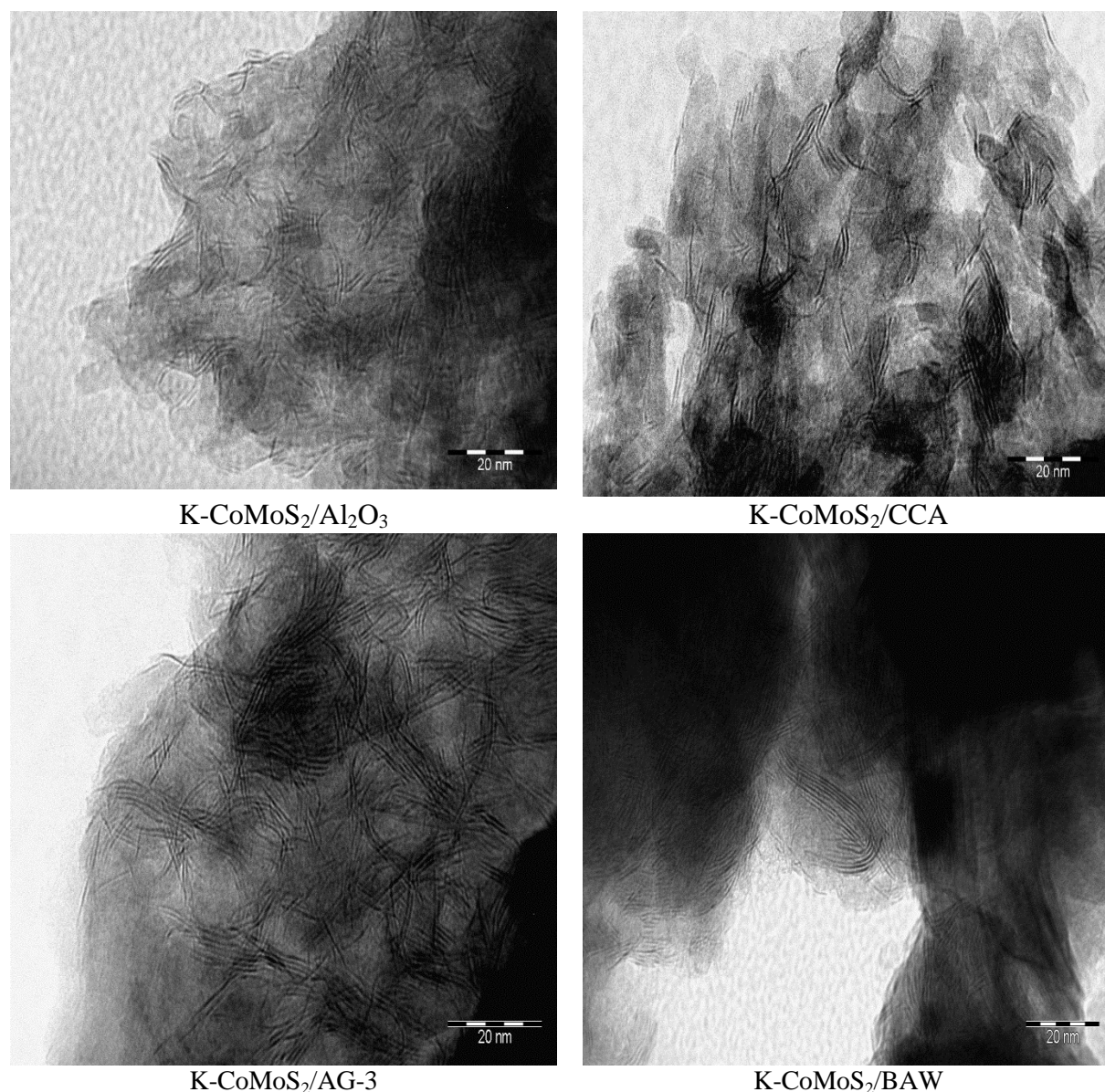
Figure 3.19. HRTEM micrographs of sulfided K-CoMoS$_2$/Sup catalysts

MoS$_2$ dispersion (D) was statistically evaluated by dividing the total number of Mo atoms at the edge surface (Mo$_e$), including corner sites (Mo$_c$), by the total number of Mo atoms (Mo$_T$) using the slab sizes measured from the TEM micrographs according to Eq. 3.1:

$$D = \frac{Mo_e + Mo_c}{Mo_T} = \frac{\sum\limits_{i=1..t} 6n_i - 6}{\sum\limits_{i=1..t} 3n_i^2 - 3n_i + 1} \qquad \text{Eq. 3.1}$$

where n_i is the number of Mo atoms along one side of the MoS_2 slab, as determined by its average slab length (nm), and t is the total number of slabs in the TEM micrographs.

The number of slabs per stack was determined to obtain the average stacking degree ($\overline{N}$), Eq. 3.2:

$$\overline{N} = \frac{\sum\limits_{i=1..t} n_i N_i}{\sum\limits_{i=1..t} n} \qquad \text{Eq. 3.2}$$

where n_i is the number of stacks in N_i layers.

The black, thread-like fringes are the MoS_2 slabs (Fig. 3.19). The fringes observed in the images were approximately 0.65 nm apart, matching the characteristic (0 0 2) basal planes of crystalline MoS_2. To calculate the average dimension of the MoS_2 phase (Table 3.7), the HRTEM statistics were done. From Table 3.4, the average dimension of the MoS_2 phase varied from 6.6 to 24.5 nm, and the average stacking number in the MoS_2 crystallites varied from 1.6 to 3.8. Carbon-contained catalysts are characterized with higher stacking number and average slab length compare to alumina-based sample. CCA shows an increase in stacking as compared to bare Al_2O_3. The number of stacked crystallites on BAW is larger than on AG-3. As was discussed in the introduction, increasing the stacking degree leads to an increase in vacancies and corner sites in the active phase, which decreases adsorption of hydride hydrogen.

Table 3.7. Morphological characteristics of supported-K-$CoMoS_2$ catalysts

Catalyst	Morphological characteristics		
	Average length $\overline{L}$ (nm)	Average stacking number $\overline{N}$	Dispersion of MoS_2 particles D
K-$CoMoS_2$/Al_2O_3	6.6	1.6	0.24
K-$CoMoS_2$/CCA	11.7	3.8	0.21
K-$CoMoS_2$/AG-3	17	2.8	0.18
K-$CoMoS_2$/BAW	24.5	3,2	0.12

The data in Fig. 3.20 were obtained from HRTEM statistics. The ACs supported catalysts are characterized by a higher stacking number and average slab length compared to the alumina and CCA samples, these results attribute to the active phase's interaction with the support being weakened, also forming of MoS_2 crystallites out of pores.
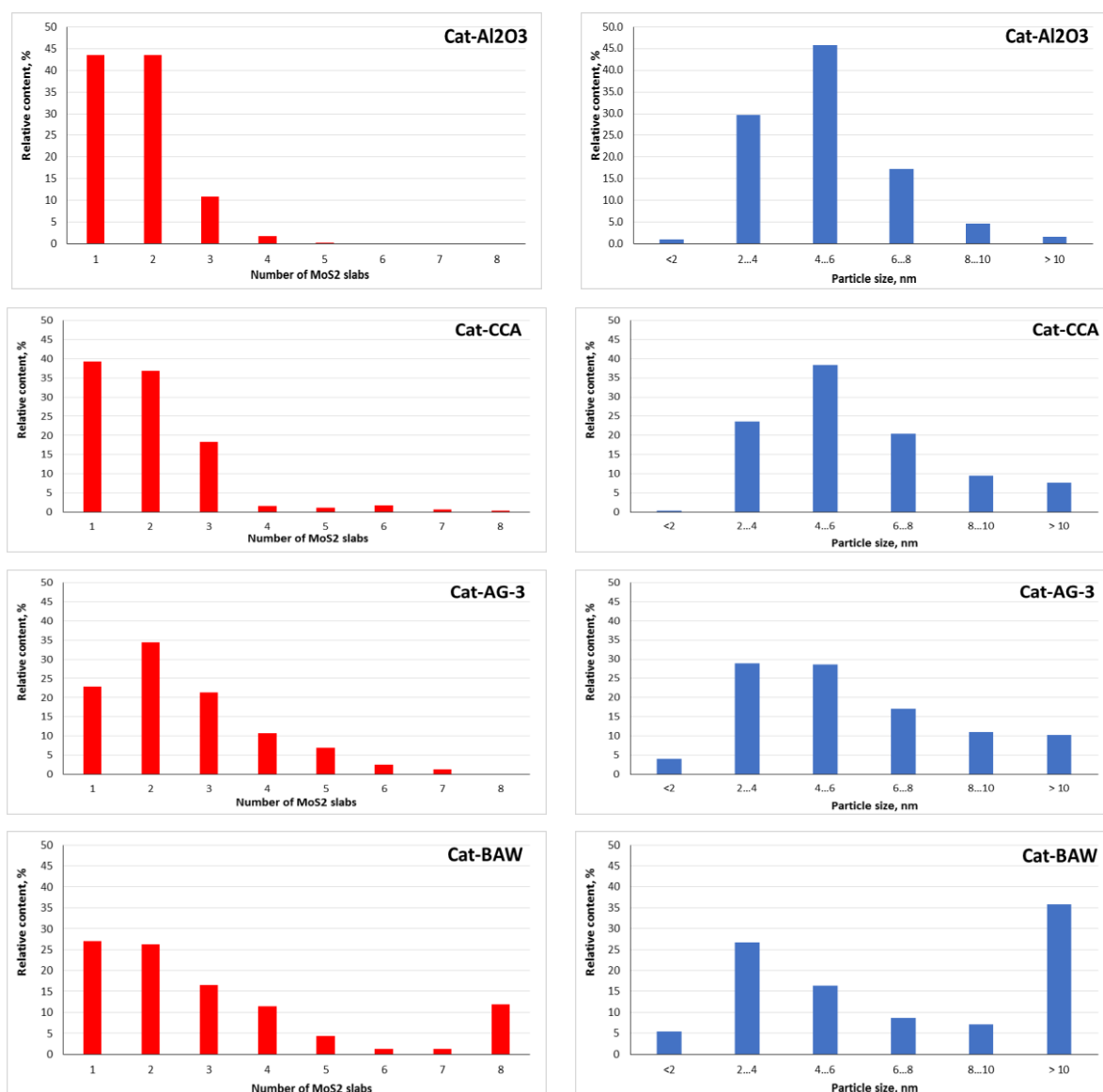
Figure 3.20. Distributions of slab lengths of MoS_2 particles and of stacking number of MoS_2 particles for sulfided catalysts.

The relative content of mono- and bi-layered crystallites of Cat-AG-3 and Cat-BAW were found to be almost half of Cat-Al_2O_3 and Cat-CCA. On the other hand, the content of 3, 4, 5, and 6, and 7 stacked slabs of BAW and AG-3 were found to be higher comparing with the counterparts. Only the Cat-BAW shows high content

of 8-stacked slabs. The highest content has been observed for particle length between 4-6 nm in all catalysts except in Cat-BAW, the highest content has been determined for particles which are lengthier than 10 nm. The dispersion results in Table 3.4. and Fig. 3.20 confirmed the higher agglomeration of BAW and AG-3 that have been characterized by SEM.

The chemical species present on the surface of K-CoMoS$_2$/Sup catalysts were evaluated by XPS. The Mo 3d spectra (Fig. 3.21) contain three Mo 3d doublets.[91]
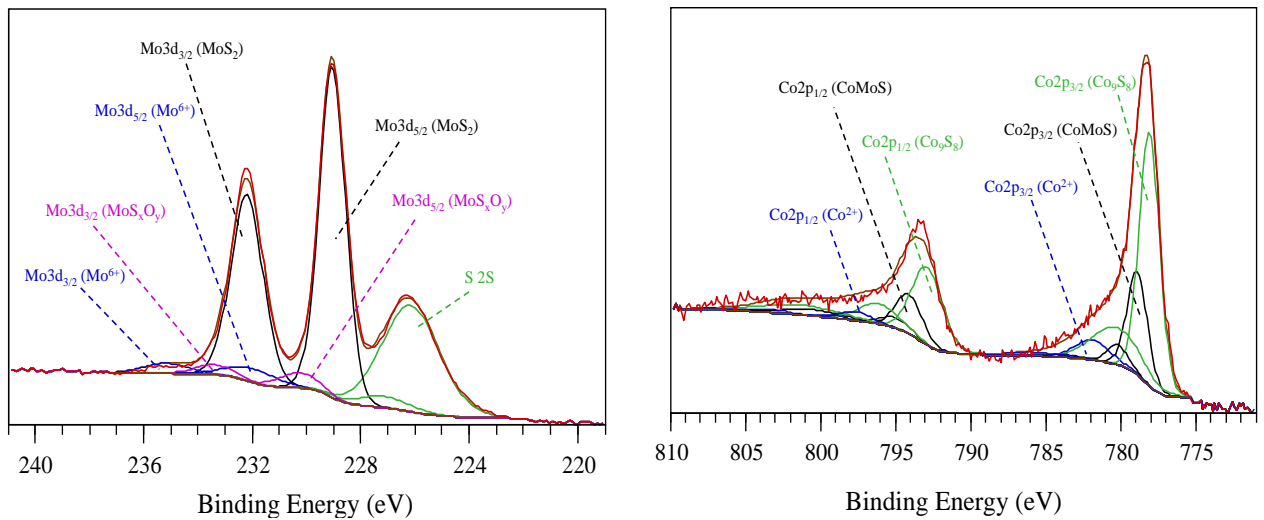
K-CoMoS$_2$/Al$_2$O$_3$
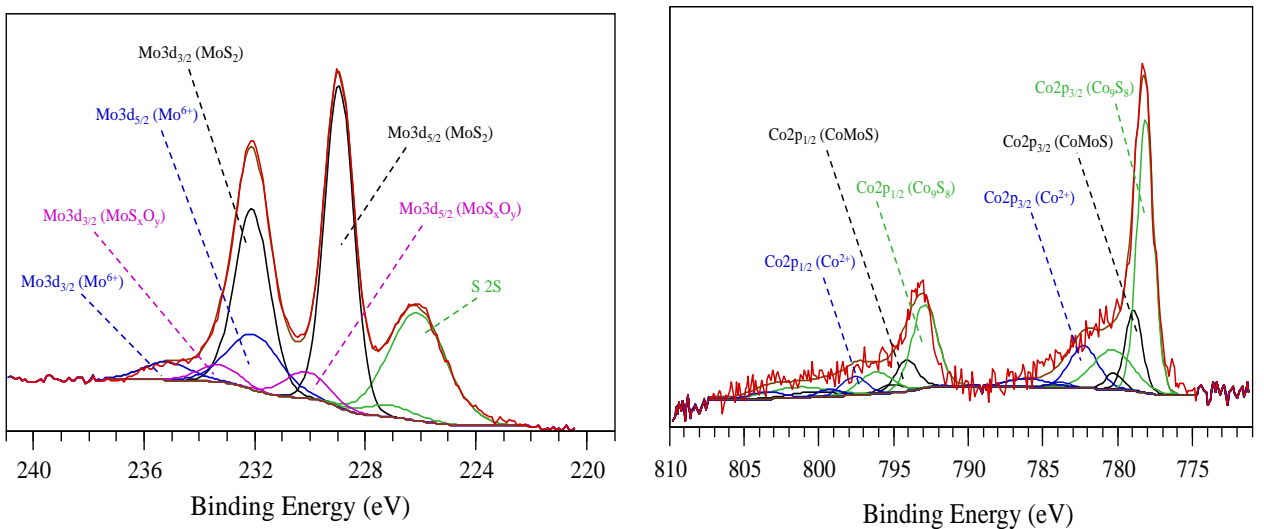
K-CoMoS$_2$/CCA
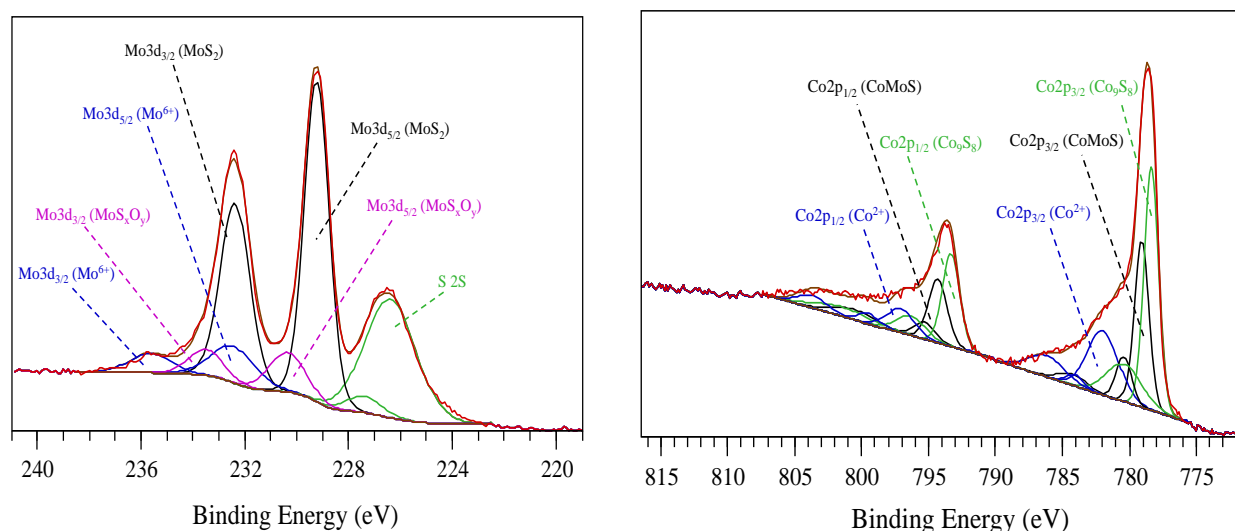
K-CoMoS₂/BAW
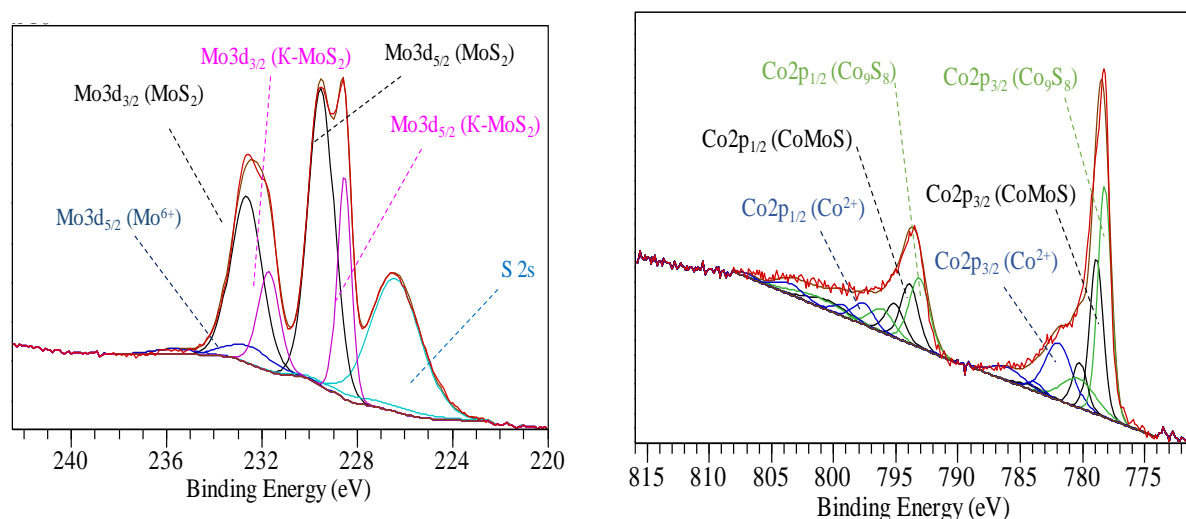
K-CoMoS₂/AG-3

Figure 3.21. XPS Co 2p and Mo 3d spectra recorded for sulfided K-CoMoS₂/Sup catalysts. Sup = Al₂O₃, CCA, BAW, AG-3. for Co 2p spectra in blue: Co^{2+} oxide contributions; in green: Co_9S_8 contributions; in grey: CoMoS phase contributions; for Mo 3d spectra in blue: Mo^{6+} oxide contributions; in pink: MoS_xO_y contributions; in grey: MoS_2 contributions.

The Mo $3d_{5/2}$ and $3d_{3/2}$ doublet with BE at 228.8 and 232.0 eV, respectively, corresponds to the Mo^{4+} in MoS_2 phase species. The doublet with BE equal to 230.0 and 233.2 eV is related to Mo^{5+} in the MoS_xO_y oxysulfide species and, finally, the doublet at 232.1 and 235.3 eV belongs to the Mo^{6+} oxide species. The peak at BE of 226.1 eV is assigned to S 2s. The spectral region of Co $2p_{3/2}$ (Fig. 3.21) contains three peaks with their respective satellites. The peak at BE of 778.6 eV is related to cobalt in the CoMoS species. The signals at 778.1 and 781.5 eV

correspond to the Co_9S_8 particles and to Co^{2+} in an oxidic environment, respectively.[91]

The decomposition of the XPS spectra revealed the metal distribution for Co and Mo species (Table 3.8). K-CoMoS$_2$/Sup catalysts are characterized with a comparable sulfidation degree: the relative amount of cobalt in CoMoS phase was in the range of 19-34 rel. % and molybdenum in MoS$_2$ particles at the level of 73-94 rel. %.

Table 3.8. Metal distribution for Co and Mo species present at the surface of sulfided K-CoMoS$_2$/Sup catalysts

Catalyst	C_{CoMoS} (wt. %)	Co percentage (%)			Mo percentage (%)			Co/Mo ratio	
		CoMoS	Co$_9$S$_8$	Co^{2+}	MoS$_2$	MoS$_x$O$_y$	Mo^{6+}	(Co/Mo)$_{slab}$	(Co/Mo)$_{edge}$
Cat-Al$_2$O$_3$	0.63	26	65	9	88	6	7	0.14	0.58
Cat-CCA	0.22	19	64	17	74	9	18	0.11	0.51
Cat-AG-3	1.67	34	45	22	94	0	6	0.16	0.79
Cat-BAW	1.17	31	44	25	73	13	13	0.22	0.87

As it follows from Fig. 3.22 (a, b, c, d), the acidity of the catalysts decreases with an increase of micropore specific area (Fig. 3.22 a and b) and pore volume grows depending on increasing of mesopore growth (Fig 3.22 c and d).
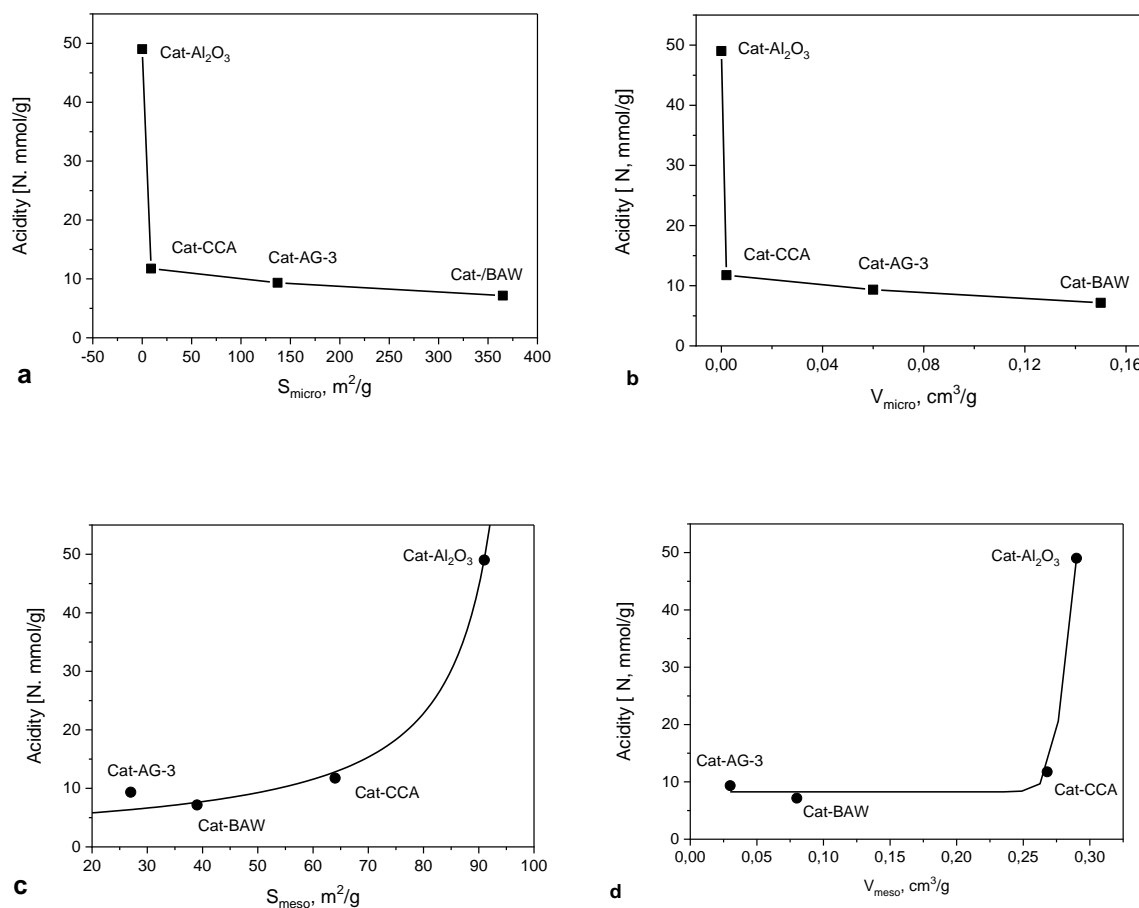
Figure 3.22. Dependences of acidity of catalysts on micropore specific surface area (S_{micro}) (***a***); micropore volume (V_{micro}) (***b***); mesopore specific surface area (S_{meso}) (***c***); and mesopore volume V_{meso} (***d***).

Acidity of the supports and catalysts are given in Fig. 3.23. It was shown that the micropore amount is favorable for catalyst activity, whereas the mesopore amount affects it negatively.
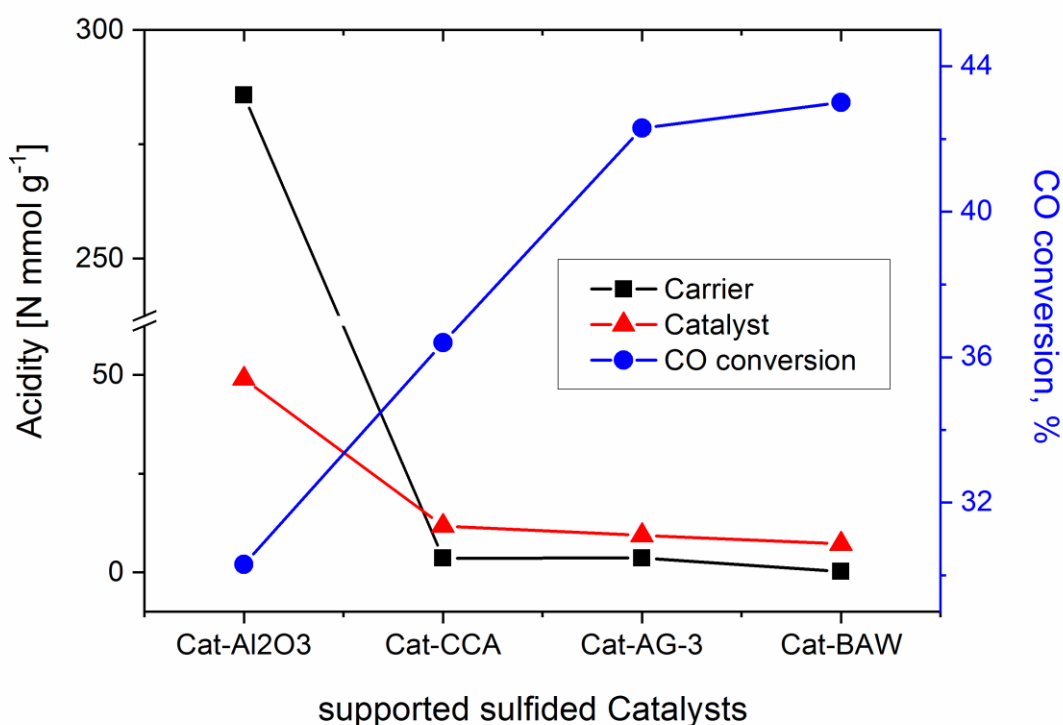
Figure 3. 23. Acidity of supports and catalysts (black and red lines, respectively) and CO conversion dependence on acidity of catalysts (blue line).

From Fig. 3.23, acidity of the supports and catalysts (black and red lines, respectively) increased in the order BAW < AG-3 < CCA < Al_2O_3. Carbon-supported sulfided catalysts show higher acidity than the bare support materials. Only for pure alumina, acidity decreased upon addition of the active phase. Presumably, the active phase K-CoMoS$_2$ possesses its own acidity, much less than that of alumina but higher than of other C-containing materials.

Fig. 3.23 shows that acidity is detrimental for CO conversion: the catalyst that shows the highest acidity (Cat-Al_2O_3) gave the lowest CO conversion (30.3%), whereas the catalyst that shows the lowest acidity (Cat-BAW) showed the highest CO conversion (43%). The carbon on the CCA decreases acidity of Al_2O_3 (Fig 3.23) which promotes CO conversion.

The optimum carbon loading for alcohol production on the CCA support is 1.7%.[114] It was established that carbon does not coat the surface of alumina uniformly if its content is below 5 wt. %, as the organic precusors adsorb

preferably on Lewis sites[114] and block them. The oxidic precursors for the active phase can only adsorb on the remaining carbon-free alumina surface, leading to sulfide crystallites with a higher stacking number.

The reaction network of alcohol formation on $K\text{-CoMoS}_2$ catalysts was investigated both experimentally and computationally,[12] showing that carbon monoxide adsorbs on a surface vacancy via its carbon atom (C-metal interaction) before being partially hydrogenated, leading to the extension of the C=O bond length. As a result, oxygen can coordinate with potassium ions present between MoS_2 layers, as shown by IR-spectroscopy.[10] Oxygen coordinated on K^+ stabilizes the alkoxyl intermediate and protects the sigma C–O bond from hydrogenolysis, in order to form an alcohol group. An alkyl fragment can react to form an alkane or undergo a chain-growth reaction with a new carbon monoxide molecule inserted between the transition metal atom and the adsorbed carbon atom.

Strong interaction between active phase and different types of carriers can lead to different electronic states on potassium and cobalt atoms. Acidic sites on the support also influence the catalytic activity. *Toyoda et al.*[8] and *Morrill et al.*[159] showed that a high content of strong acid sites leads to impeding of alcohol formation and accelerates hydrogenation reactions.

The selectivity for CH_4 was found to be higher than that for C_{2+} for all catalysts (Fig. 3.24). Furthermore, a positive correlation has been noted between the methane selectivity and micropore surface area and volume (see textural results in Table 3.6). EtOH was the main product for all supported-$K\text{-CoMoS}_2$ catalysts (Fig. 3.24).
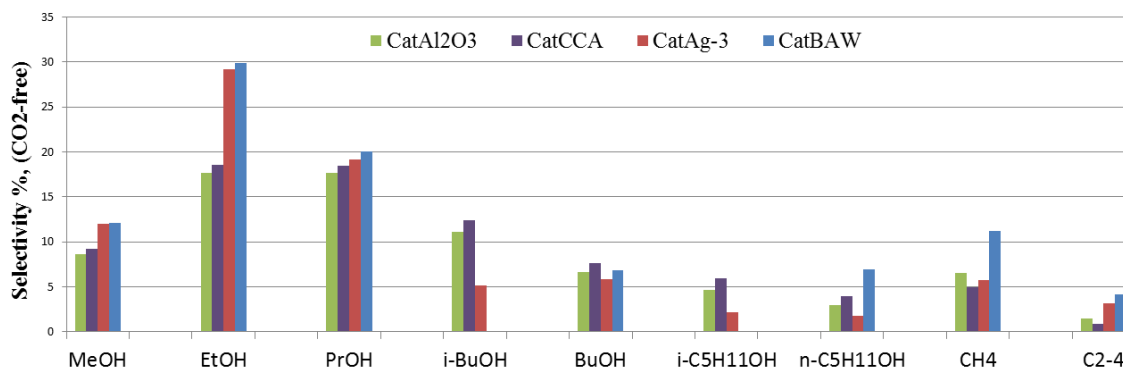
Figure 3.24. Selectivity for different alcohols, CH_4, and C_{2+} HC over the supported K-CoMoS$_2$ catalysts. Reaction conditions: T = 360 °C, P = 5.0 MPa, CO:H$_2$:Ar = 45:45:10 gas at 760 l·h^{-1}·(kg cat)$^{-1}$, catalyst loading 3 grams.

The selectivity towards methanol, ethanol, and propanol-1 decreases in the order Cat-BAW > Cat-AG-3 > Cat-CCA > Cat-Al$_2$O$_3$. Cat-BAW did not produce any i-butanol or i-pentanol, whereas the Cat-CCA supported catalyst showed the highest yield of i-pentanol alcohol. The highest selectivity for CH$_4$ and C$_{2+}$ hydrocarbons was observed at 360 ^{o}C. The methane selectivity depends on the catalyst support nature and increases in the order Cat-CCA < Cat-Al$_2$O$_3$ < Cat-AG-3 < Cat-BAW (Fig. 2.24). The ratio between yields of alcohols and hydrocarbons ($Y_{ROH/HCs}$) for our catalysts is given in Fig. 2.25.
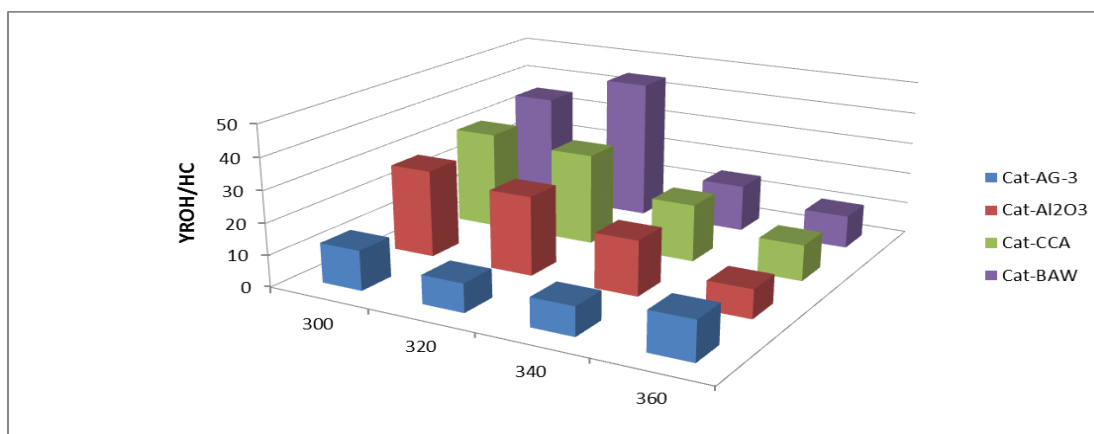
Figure 3.25. Alcohols/hydrocarbons yield ratio ($Y_{ROH/HCs}$) at different temperatures. For reaction conditions see Fig. 3.24.

The yield ratio between alcohols and hydrocarbons increases in the order Cat-AG-3 < Cat-Al$_2$O$_3$ < Cat-CCA < Cat-BAW (Fig 3.25). The highest $Y_{ROH/HCs}$

for Cat-BAW can be attributed to its highest total and micropore surface area, as well as micropore volume (Table 3.3 and Fig. 3.14 a). In general, high surface area (BAW=500 m^2 g^{-1}) increases catalytic performance of AC-supported catalysts, as well as their stability in basic or acidic media and towards severe reaction conditions such as high pressure and temperature. In the case of our $K-CoMoS_2$ catalyst, minimal active phase-support interaction is also beneficial.[25,160] $Y_{ROH/HCs}$ increased when coating alumina with carbon, due to lower active phase-support interaction. The dependence of the HC chain growth coefficient αi on a carbon atom number (i) in the chain of intermediate products is given in Fig 3.26.
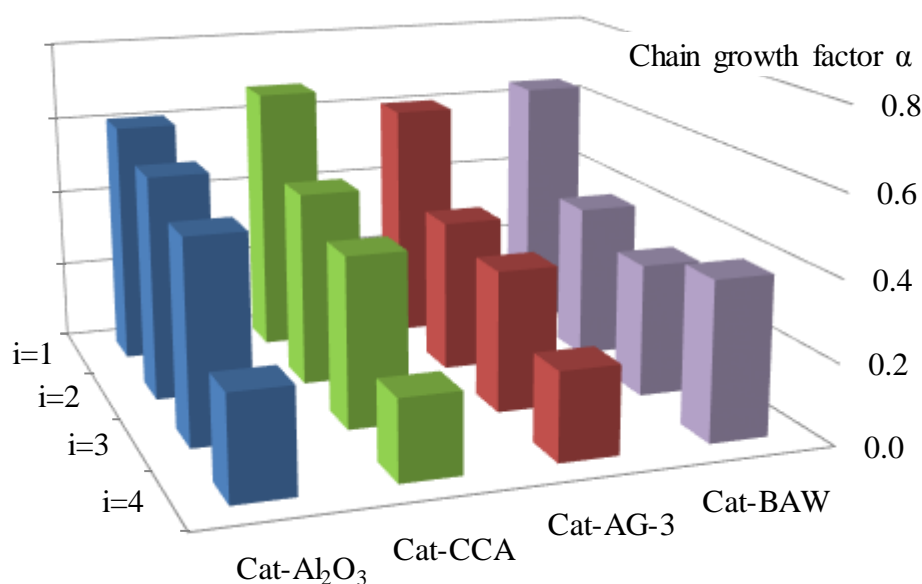
Figure 3.26. Chain growth factors α_i for steps i=1, 2, 3, 4 over the $K-CoMoS_2$ catalysts supported on Al_2O_3, CCA, AG-3 and BAW. For reaction conditions see Figure 3.24.

Cat-CCA shows maximum α_1 for alcohol formation. $Cat-Al_2O_3$ shows maximum α_2 and α_3, and Cat-BAW showed maximum α_4 (Fig. 3.26). It has to be noted that in spite of high values of α_1, α_2 and α_3 for alumina- and CCA-supported catalysts, their alcohol yield was lower than for the AC-supported catalysts. All previously discussed results relate to the textural characteristics of the catalysts, particularly S_{micro}, V_{micro}, S_{meso}, and V_{meso}. Microporous catalysts were found to be more active regarding CO conversion than mesoporous catalysts (see Fig. 3.27).
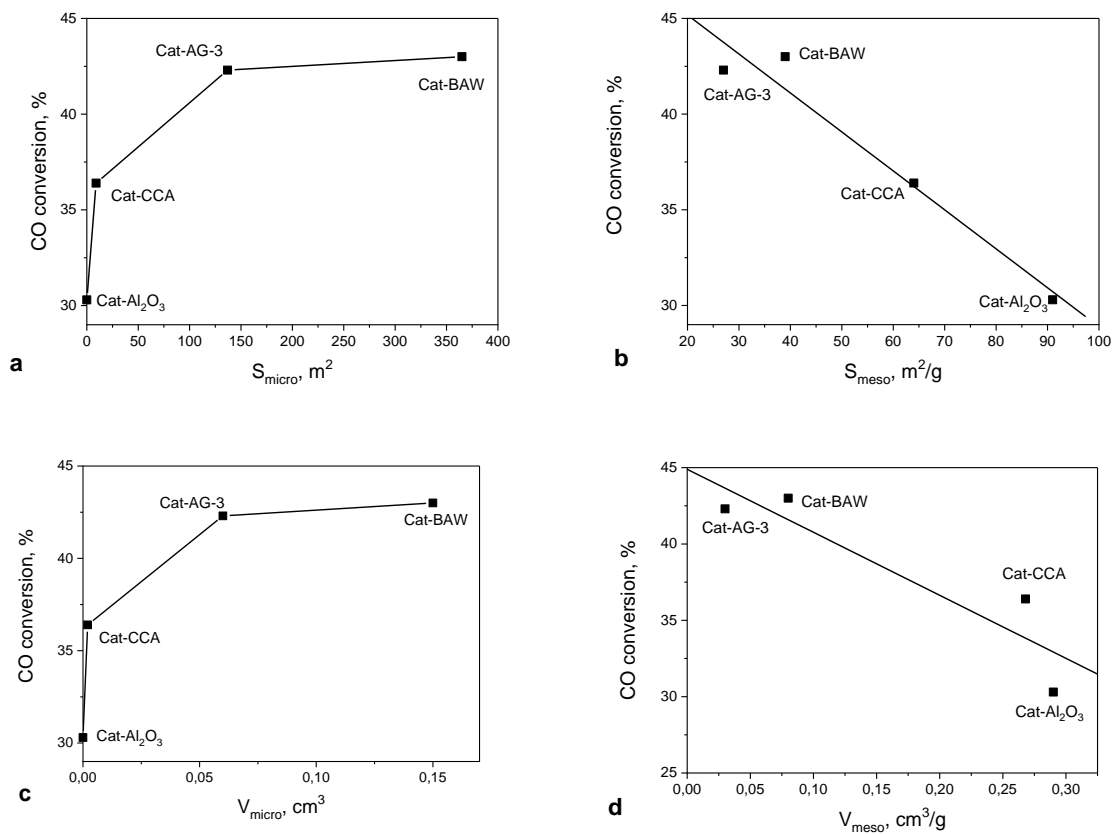
Figure 3.27. Dependences of CO conversion on S_{micro} (*a*), S_{meso} (*b*); V_{micro} (*c*) and V_{meso} (*d*) at 360°C.
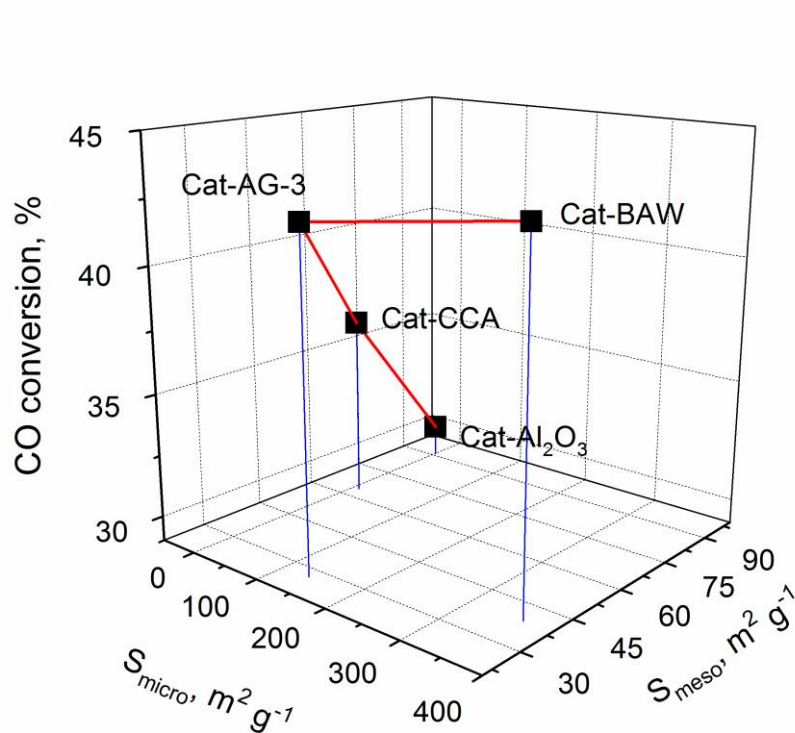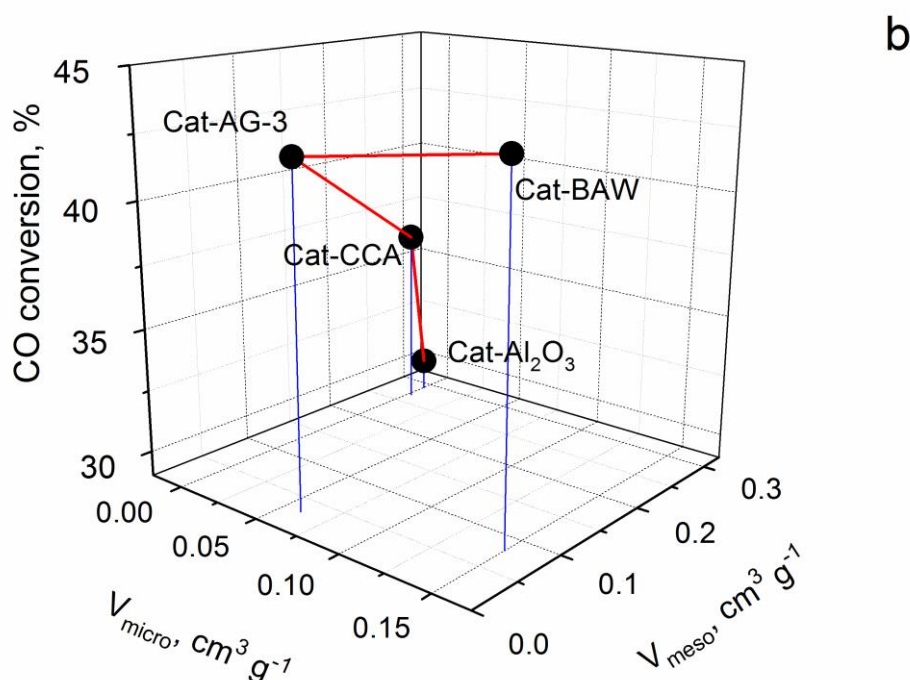
Figure 3.28. 3D plots of CO conversion, %, depending on (*a*) surface area of micro- (S_{micro}) and mesopores (S_{meso}), m^2/g, and (*b*) pore volume of micro- (V_{micro}) and mesopores (V_{meso}), cm^3/g.

Fig. 3.28 (*a* and *b*) shows the relation of CO conversion to total meso- and micropore specific surface area and volume. It is seen that dependence of CO conversion on V_{meso} grows essentially faster than on S_{meso} in the interval from Cat-Al_2O_3 to Cat-CCA. The following changes of CO conversion *vs* micro- and mesopore surface area and volume look similar on (*a*) and (*b*) plots. The observed difference can be explained by amorphous carbon present on the alumina surface of the CCA support as described earlier.

If we assume a simplified cylinder model for a mesopore (Fig. 3.29 *a*) with amorphous carbon covering its internal surface (Fig 3.29 *b*), we can see that a decrease of the pore volume will be less impactful than a reduction of the internal surface (Fig. 3.29 *c*).
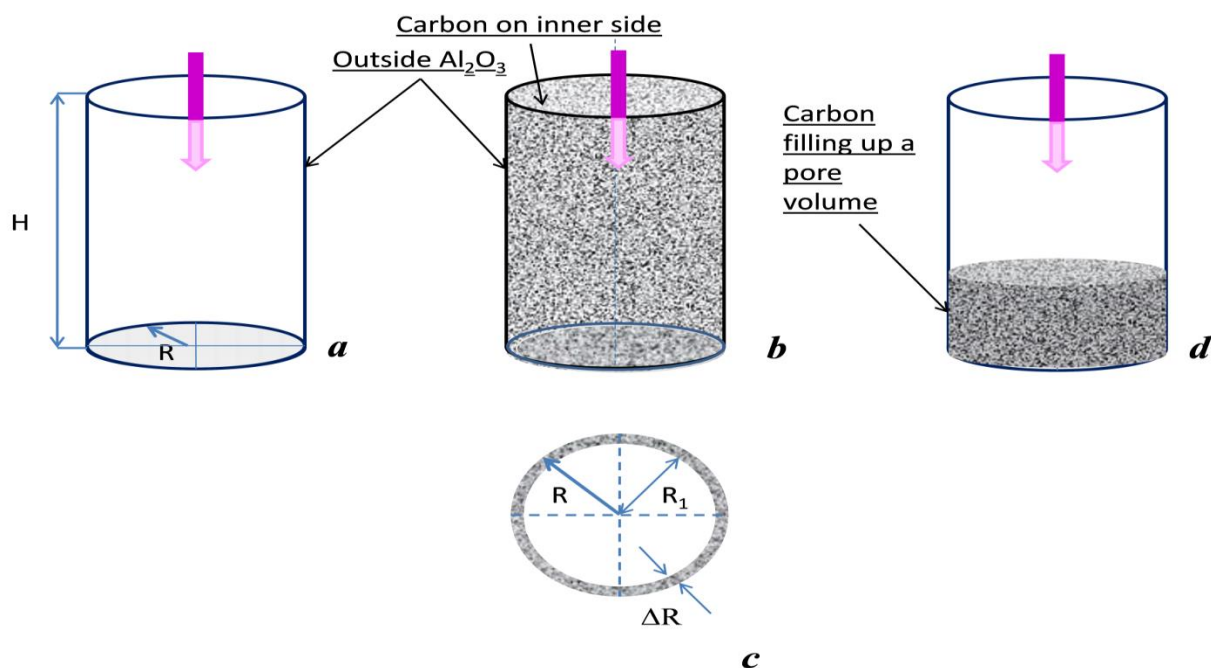
Figure 3.29. Simplified cylinder-type model of a mesopore in Cat-Al_2O_3 and Cat-CCA. (**a**) empty Al_2O_3 mesopore, side view; (**b**) a mesopore with carbon deposited on its internal surface to form CCA, side view; (**c**) a mesopore with carbon deposited on its internal surface to form CCA, top view; (**d**) amorphous carbon filling up part of the mesopore volume in CCA, side view.

As the CO conversion versus the mesopore specific surface increases more than versus the mesopore volume for Cat-CCA compared to Cat-Al_2O_3, carbon cannot fill the entire volume of the mesopores of the Cat-CCA as depicted in Fig 3.29**d**. Covering of a mesopore wall by monolayer (less probable case) or by islands (more probable case) of amorphous carbon results in the decrease of hydroxyl groups of alumina in the CCA carrier and thus decreases the interaction between the active phase and the support material, leading to increased catalyst activity in CO conversion.

Next to the CO conversion, the yield of alcohols also correlates with the micropore surface and volume, as is demonstrated in Fig. 3.30.
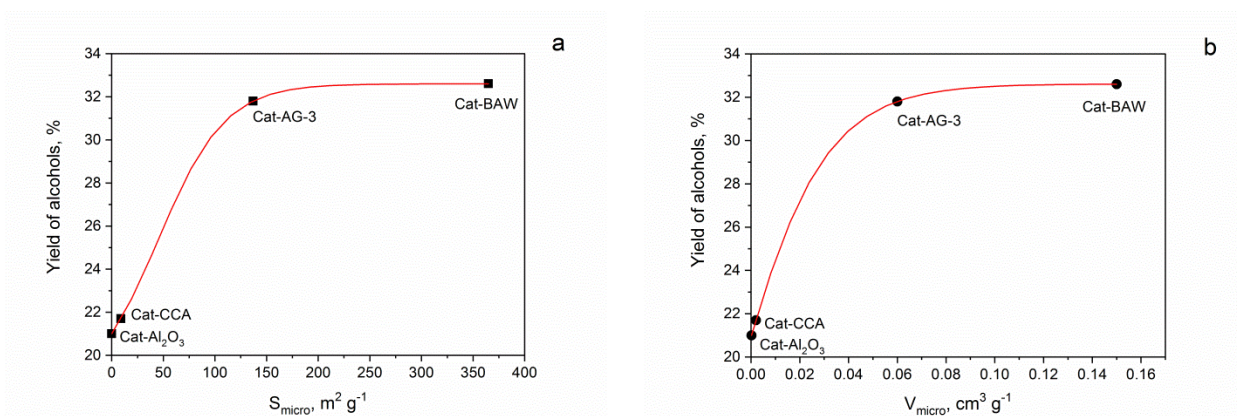
Figure 3.30. Dependences of alcohol yield on micropore specific surface area (S_{micro}) (***a***); and pore volume (V_{micro}) (***b***) at 360°C.

The plateau reached by the alcohol yield in correlation with the micropore structure of Cat-AG-3 and Cat-BAW indicates optimal size of the micropores. In contrast, dependences of catalytic activity on the mesopores specific surface area (S_{meso}) and pore volume (V_{meso}) demonstrate an opposite trend: fewer mesopores result in higher catalytic activity (Fig. 3.31).
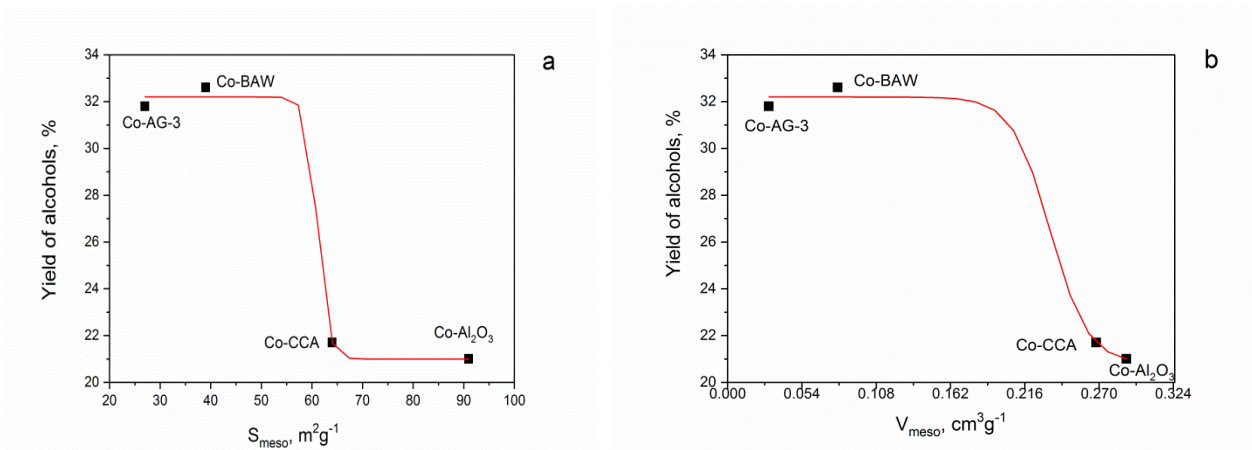
Figure 3.31. Dependences of the alcohol yield on the meso + macropores specific surface area (S_{micro}) (a); and pore volume (V_{micro}) (b) at 360°C.

Surisetty et al. [23] on the contrary, found that mesoporous carbon as a support gives higher activity than microporous carbon. Mesoporous MWCNT as a support for alkali-modified trimetallic Co–Rh–Mo sulfide catalyst gave higher catalytic activity and selectivity for the alcohol formation from syngas than microporous AC. They postulate that the CO conversion and alcohol yield are related to the textural properties of the support such as pore size and mesoporosity

rather than its surface area and pore volume. They also find that dispersion on mesoporous MWCNT is lower than on microporous AC. This corroborates our findings of large $CoMoS_2$ agglomerates formed on mesoporous alumina and CCA (Fig. 3.16). **Surisetty et al.**[4] attribute higher catalytic activity of mesoporous MWCNT as a support to decreased diffusion limitations compared to microporous supports. Their results show that even a small amount of mesopores is better than a large amount of micropores. Our best performing catalysts (Cat-AG-3 and Cat-BAW) contain mainly micropores with some mesopores, whereas Cat-Al_2O_3 and Cat-CCA contain almost only mesopores (Fig. 3.1.) BAW includes wide channels with large amounts of meso- and micropores in its walls (Fig. 3.17 and 3.18). We suggest that the presence of various functional groups on the carbon surface is a crucial factor influencing catalytic activity and alcohol selectivity of carbon-supported materials. Such functional groups may strongly interact with active phase crystallites and also increase acidity of the carrier. Both factors negatively affect catalytic activity. Moreover, the order of acidity from Fig 3.23, (Cat-Al_2O_3 > Cat-CCA > Cat-AG-3 > Cat-BAW) supports our interpretation of the relationship between catalysts' porosity and alcohol selectivity. The MWCNT material used in[4] probably contained less functional groups than activated carbon–based materials. In this connection it may be interesting to consider the contribution of each product into total alcohol yields depending on the pore structure. Fig. 3.32 shows that ethanol, propanol and methanol are main alcohol products for our catalysts. Their yield increases with the micropore surface and volume, and decreases with the mesopore surface and volume. The yield of n-butanol is not related to carrier porosity. n-Pentanol is a minor product. *i*-Butanol and *i*-pentanol exhibit opposite trends comparing to the main products, decreasing with the increasing micropore surface and volume and increasing with the increasing mesopore surface and volume. Microporous carriers inhibit isomerization due to steric constraints. On the other hand, the abnormal selectivity of Cat-GCA2 towards propanol-1 and amyl alcohol-1 can also be explained by microporous cracks formed on the surface of the catalyst. This result corroborates the validity of

the observed unusual finding: microporous supported K-CoMoS$_2$ catalysts are more active than mesoporous ones. We explain this phenomenon by active phase distribution inside the pores and acidity of the catalysts.
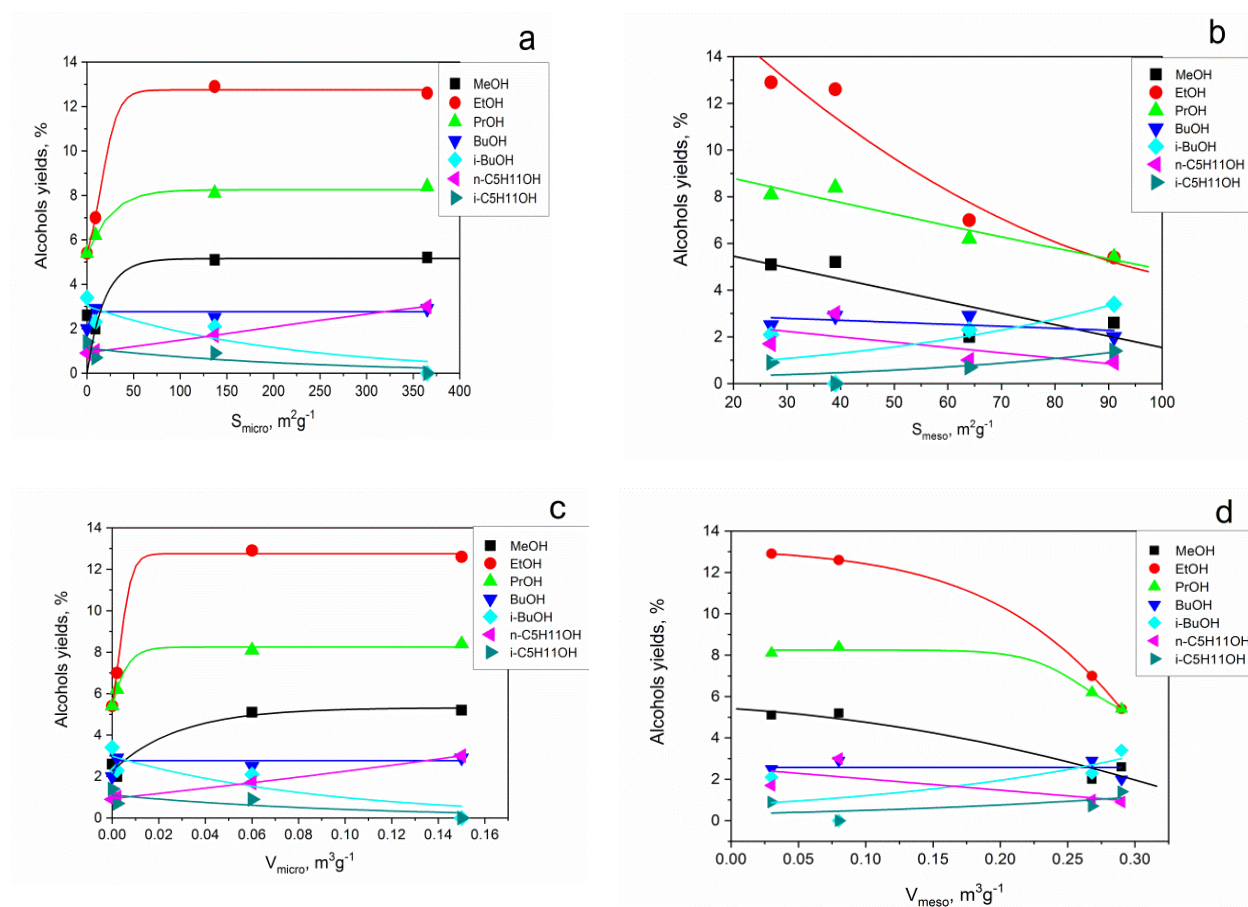
Figure 3.32. Dependences of separate alcohol yields on S$_{micro}$ (**a**), S$_{meso}$ (**b**); V$_{micro}$ (**c**) and V$_{meso}$ (**d**) at 360°C.

Fig 3.32 revealed that the highest yield of methanol, ethanol, propanol-1, *i*-butanol, pentanol alcohol and *i*-pentanol alcohol was achieved at 360 ^{o}C for all catalysts. Propanol-2 and butanol-2 appeared only for Cat-CCA. Linear alcohols decrease in the order of Cat-BAW > Cat-AG-3> Cat-CCA > Cat-Al$_2$O$_3$; *i*-alcohols follow the opposite order CatAl$_2$O$_3$ > Cat-CCA > Cat-AG-3 > Cat-BAW. Besides, an interesting observation can be made if to draw the plots similar to those in Fig. 3.33, but built on the basis of CO conversion dependences on the pore surface and volume (Fig. 3.27: CO conv. as function of S$_{micro}$, S$_{meso}$, V$_{micro}$, V$_{meswo}$) (Fig. 3.34). A similar shape of corresponding dependences in Figs. 3.35 and 3.36 shows that

CO conversion is mostly determined by the alcohol formation. Otherwise the shapes of the plots in Figs. 3.33 and 3.34 would not coincide.
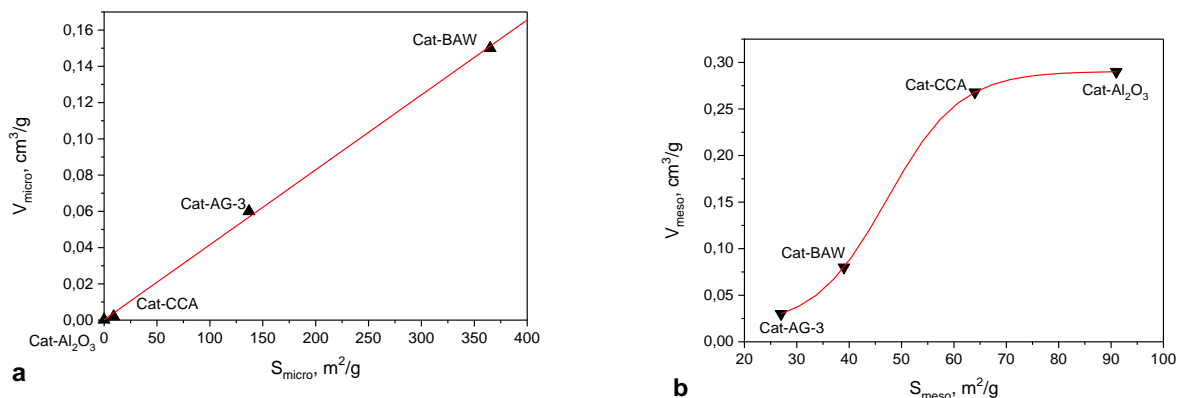
Figure 3.33. Correlations between pore volume and specific surface area for micropores (V_{micro} vs. S_{micro}) (**a**); and for [macro + mesopores] (V_{meso} vs. S_{meso}) (**b**) built on the basis of the dependences of alcohol yield on pore volume and specific surface area from Fig. 3.29 and 3.30.
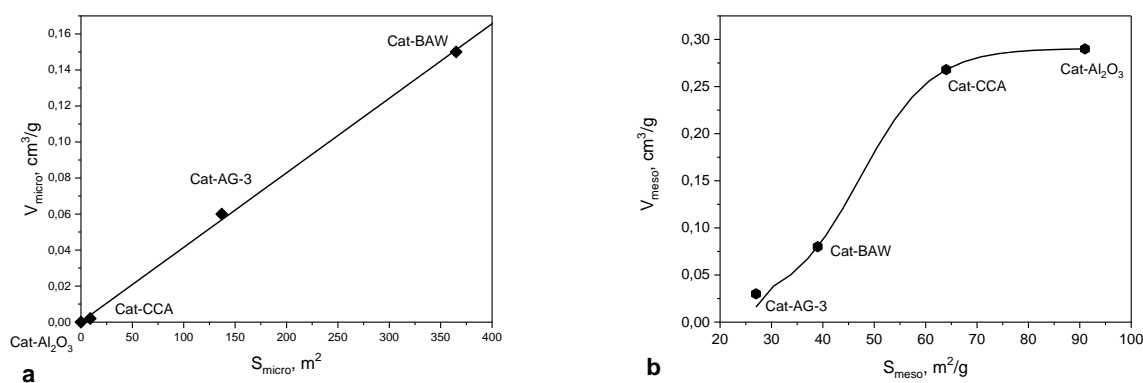
Figure 3.34. Correlations between pore volume and specific surface area for micropores (V_{micro} vs. S_{micro}) (**a**); and for [macro + mesopores] (V_{meso} vs. S_{meso}) (**b**) built on the basis of the dependences of CO conversion on pore volume and specific surface area from Fig. 3.27.

Furthermore, the results shown in Fig. 3.20 corroborate catalytic performance of our catalysts (Cat-Al$_2$O$_3$ < Cat-CCA < Cat-AG-3 < Cat-BAW). The higher average stacking number of Cat-CCA comparing with Cat-Al$_2$O$_3$ attributes to the role of carbon in decreasing the interaction between Al$_2$O$_3$ and the K-CoMoS phase. The observed activity can be explained by "Rim-Edge" model.[158] According to the model, changing of the height/diameter ratio of the crystallite controls the relative quantity of active sites and consequently affects

catalytic performance. On the other hand, AC-based catalysts contained a greater proportion of the multilayered (CoMoS-II) phase, which was attributed to the active phase-support interaction. Thus, increasing of the crystallites' linear dimension and stacking degree (i.e. increased edge sites) resulted in the increase in catalytic activity because such morphologies contain a higher ratio of basal, corner and surface sites of the catalyst which promote HAS. The highest average stacking number and average slab length determine the highest activity of Cat-BAW. The particles distribution also conditions catalytic performance of Cat-Al$_2$O$_3$, Cat-CCA, Cat-AG-3, and Cat-Cat-BAW.

3.3. Comparative Study on the Catalytic Performance of K-Modified CoMoS$_2$ catalyst supported on novel fiber and powder activated carbons in higher alcohols synthesis from syngas.

In this part, series of K-modified CoMoS$_2$ catalysts with compositions 10% K, 3.6% Co, and 12 wt.% Mo supported over novel commercial activated carbons such as powder materials (DAC; OBC-1), and fiber materials (fabric active sorption (TCA) and non-woven activated material (AHM)) were prepared, characterized, and tested in syngas conversion. Aiming to increase the selectivity toward alcohols and compare the catalytic activity.

Table 3.9 shows the targeted and detected composition of K-CoMoS catalysts supported on powder and fiber activated carbons. The composition of the detected elements is close to that of the targeted composition of precursors.

Table 3.9. Elemental compositions of supported catalysts

Catalyst	Targeted composition (wt. %)			Measured composition (wt. %)		
	K	Mo	Co	K	Mo	Co
K-CoMoS$_2$-DAC	10	12	3.7	8.5	11.9	3.7
K-CoMoS$_2$-OBC-1	10	12	3.7	8.4	15.8	3.9
K-CoMoS$_2$-TCA	10	12	3.7	11.3	13.9	4.2
K-CoMoS$_2$-AHM	10	12	3.7	11.1	15.1	4.6

Table 3.10 shows the results for the surface area, total pore volume, average pore diameter, micro- and mesopores surface areas, and micro- and mesopore volumes of the stabilized catalysts in the sulfided form.

Table 3.10. Textural properties of supports and sulfide catalysts supported on powder activated carbons

Sample	S_{total}, m^2/g	S_{micro}, m^2/g	S_{*meso}, m^2/g	V_{total}, cm^3/g	V_{micro}, cm^3/g	V_{**meso}, cm^3/g	Average pore diameter (nm)
DAC	723.577	661.989	61.588	0.3399	0.281	0.0589	3.169
OBC-1	711.287	660.366	50.921	0.3169	0.271	0.0459	3.775
K-CoMoS$_2$/DAC	249.539	242.710	6.829	0.107	0.102	0.005	3.285
K-CoMoS$_2$/OBC-1	177.763	142.282	35.481	0.09348	0.060	0.03348	3.168
$S_{meso}* = S_{total} - S_{micro}$; $V_{meso}** = V_{total} - V_{micro}$							

Powder commercial activated carbons DAC and OBC-1showed the BET surface area of 723.577 and 711.287 m^2/g, and total pore volume of 0.3399 and 0.3169 cm^3/g. Impregnation of the AC supports by the K-CoMoS active phase decreased the surface area to 249.539 and 177.763 m^2/g, and the total pore volumes to 0.107 and 0.09348 cm^3/g. Furthermore, the average pore diameter of DAC increased after having been impregnated by the active phase from 3.169 to 3.285 nm although it decreased from 3.775 to 3.168 nm in the case of OBC-1. The decrease in the BET surface area, pore volume, and pore diameter of the catalysts when compared to pure supports indicates that the added metal particles have blocked the pores. Although both powdered activated carbon supports have almost the same pore characteristics, the K-CoMoS active phase occurred in different places. In the case of Cat-DAC, the metal species fell on the mesopores, which led to the formation of the micropours catalyst with a small mesoporous surface area (6.829 m^2/g) compared to Cat-OBC-1 (35.481 m^2/g).

The surface morphologies which are characterized by SEM of powder commercial activated carbons supports of DAC; OBK-1, and the catalysts Cat-DAC; Cat-OBK-1 are represented on Fig. 3.35, whereas the SEM images of fabric active sorption (TCA), non-woven activated material (AHM) and their catalysts Cat-TCA and Cat-AHM are shown in Fig. 3.36.

Support name	SEM image of support	SEM image of supported-K-CoMoS$_2$ catalyst
DAC		
OBC-1		
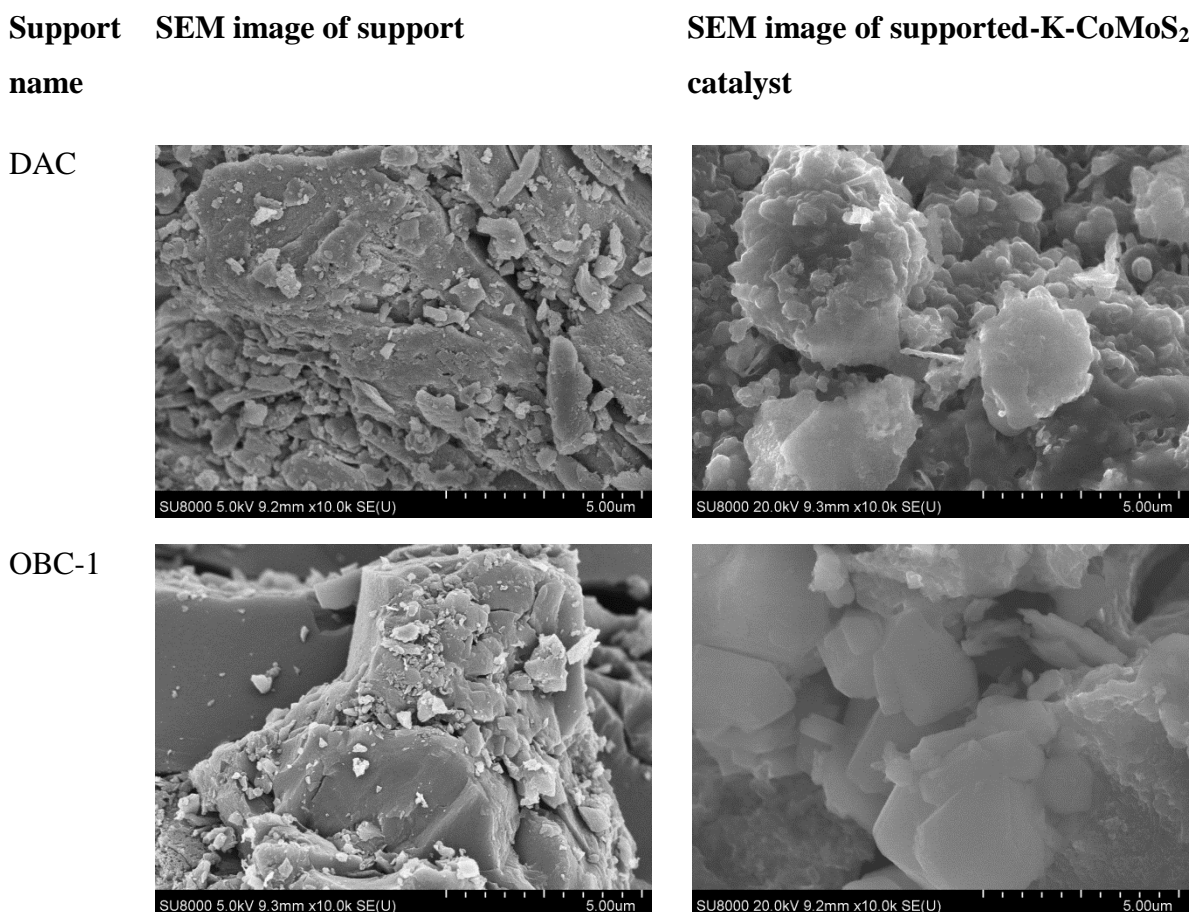
Figure 3.35. SEM images of powder activated carbon supports and supported K-CoMoS$_2$ catalysts

Fig. 3.35 illustrates the surface morphology of the powder activated carbon (DAC and OBK-1) before and after impregnated by K-CoMoS active phase. As seen in Fig. 3.35, before the impregnation, the surface morphology of powder-activated carbons has uneven cavities and fine open pores. An irregular structure and developed pores can be seen after impregnated by the K-CoMoS active phase, which appears a smoother surface of activated carbon. The development of pores

can be due to the effect of the K-CoMoS active phase that has filled the pores. Also, more holes and pits are noted.

TCA   AHM
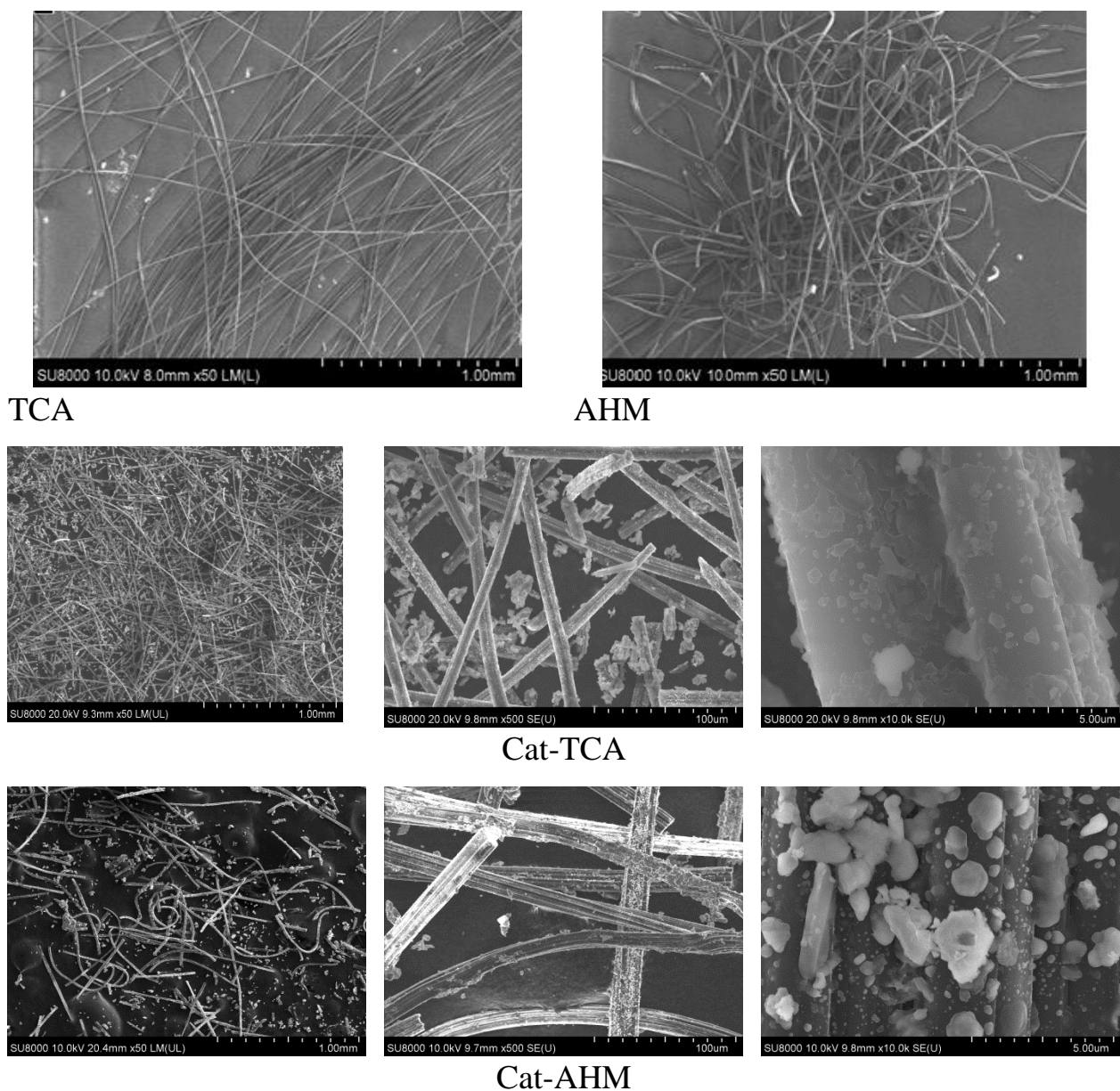
Cat-TCA

Cat-AHM

Figure 3.36. SEM images of fabric active sorption (TCA), non-woven activated material (AHM) and their catalysts Cat-TCA and Cat-AHM at high magnification (5mm) and low magnifications (100um and 1 mm).

From the SEM images shown in Fig. 3.36, it can be observed that the fabric active sorption and non-woven activated material ACs present a filamentous morphology with strip axial arrangement and that a few longitudinal grooves and many irregular particles are distributed on the fiber surfaces. Otherwise, the degree of entanglement of strip axial in AHM was found to be more than TCA. The SEM

images of the catalysts reveal that the surface of fiber activated carbon is smoother after impregnated by K-CoMoS active phase. Some axial wedge fractures are also observed, but the longitudinal texture and porosity of fiber ACs are still retained.

The Energy Dispersive X-ray (EDX) spectra of supported-K-CoMoS$_2$ catalysts are depicted in Fig. 3.37, and the distribution maps of powder and fiber activated carbons are shown in Figs. 3. 38 and 3.39.
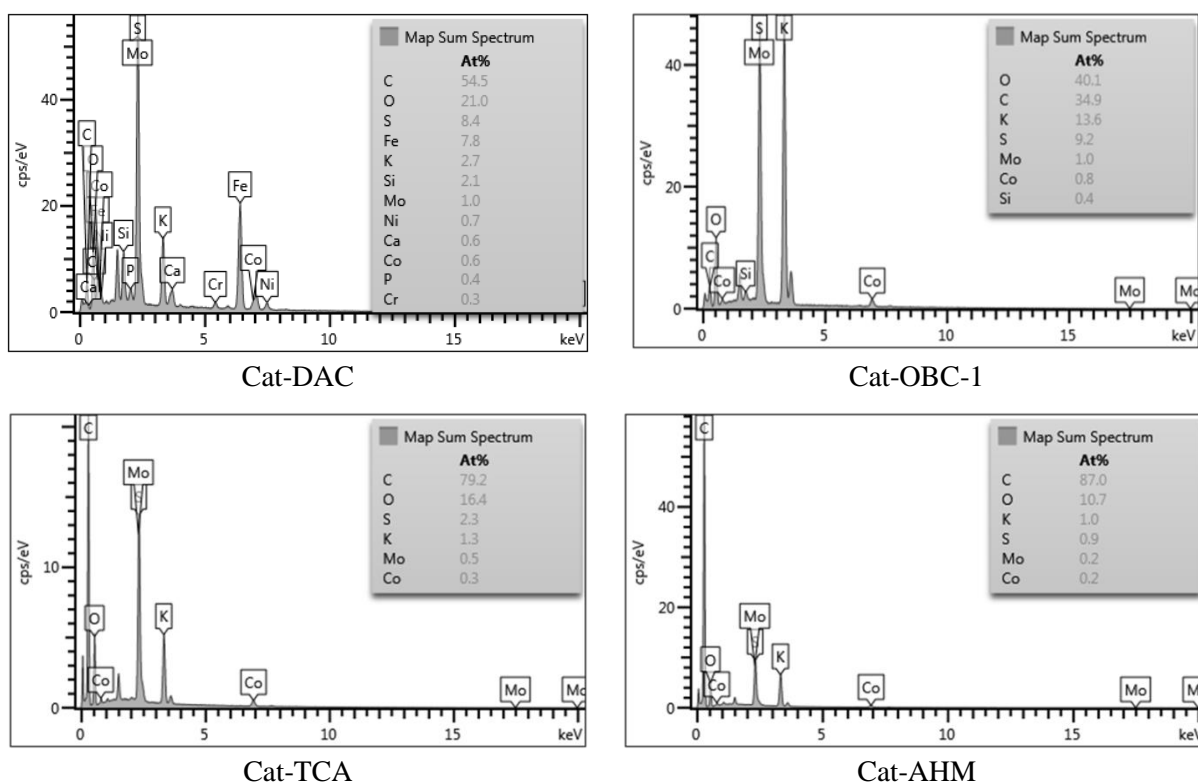
Figure 3.37. The Energy Dispersive X-ray (EDX) map sum spectrum of supported-K-CoMoS$_2$.

The EDX analysis reveals that the composition consists primarily of the K-CoMoS active phase, carbon, and oxygen. According to the results, Cat-DAC has also been found to include trace elements such as Si, Fe, Ni, Cr, and P, which can be attributed to the commercial activated carbon support. There are strong signals around 2.5 keV attributed to the Mo and S elemental distribution, which is similar to the EDX study results of MoS$_2$ catalysts in.[161] Although there are small differences between the targeted percentage of elements and the detected percentage by EDX, this technique is not useful for quantitative analysis because the complete spectrum was obtained very fast and contains both semi-qualitative

and semi-quantitative information.[162, 163] That is why we have adopted the elementary composition results obtained from XRF as real and more accurate data (Table 3.9). The EDX maps of sulfide catalysts supported on powder activated carbon at 2.5 µm are presented in Fig. 3.38.
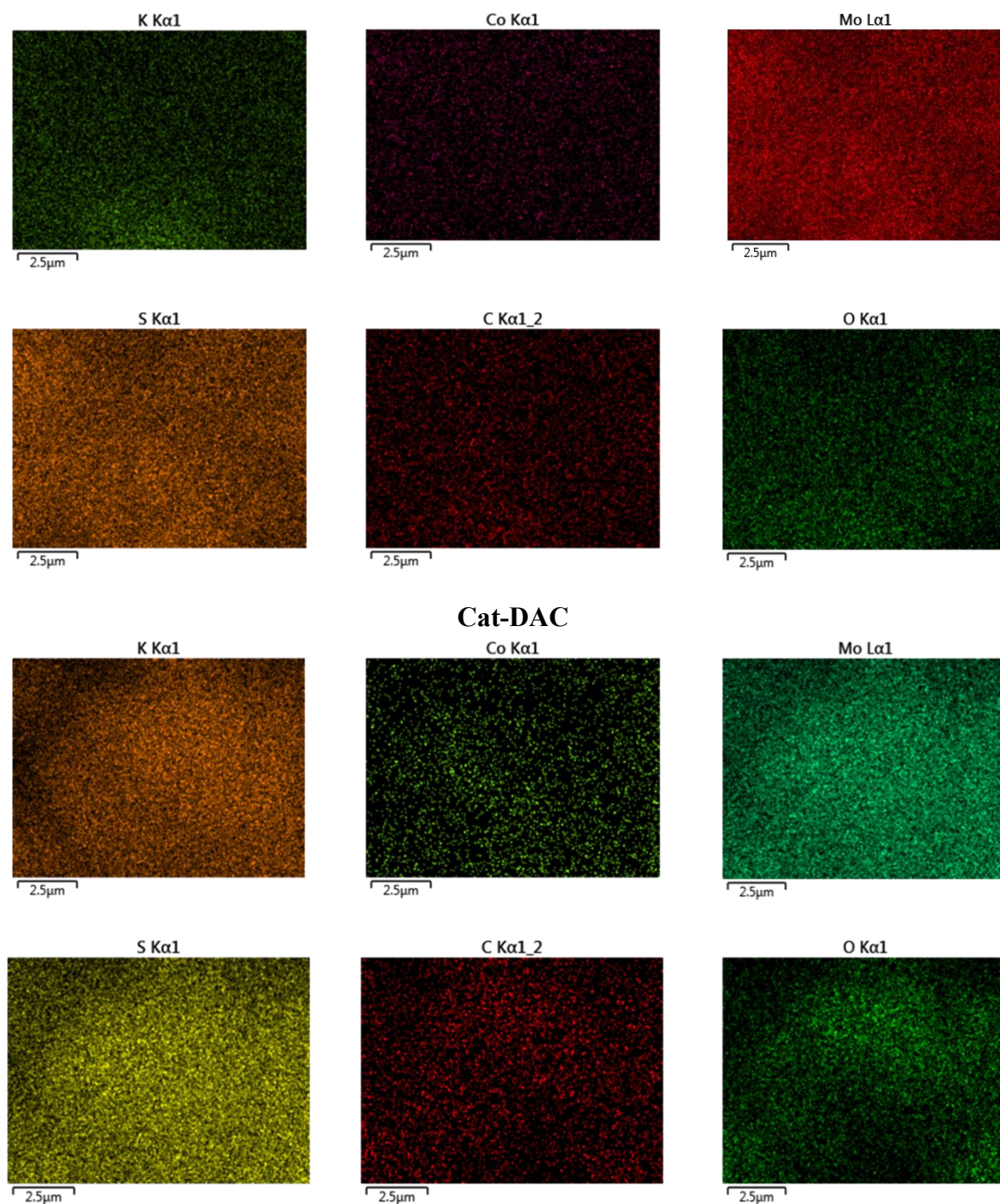
Cat-DAC

Cat-OBC-1

Figure 3.38. The EDX maps of the K-CoMoS$_2$ catalysts supported on powder commercial activated carbons

Cat-DAC and Cat-OBC1 catalysts show slight differences in the EDX maps shown in Fig. 3.38. The distribution maps of S, Co, Mo, and K obtained on the surface of the K-CoMoS$_2$ catalyst coincide completely, indicating that the elements form a unified phase.

The agglomeration of K-CoMoS active phase elements in fiber activated carbons (Fig. 3.36 and 3.39) was found to be more than powder activated carbons (Figs. 3.35 and 3.39). Fig. 3.39 indicates that the components constitute a single phase. Thus, all metals are in close contact with each other, and molybdenum basically acts as a "sulfur protector" with some other phases of CoS$_x$.

Cat-TCA

Cat-AHM
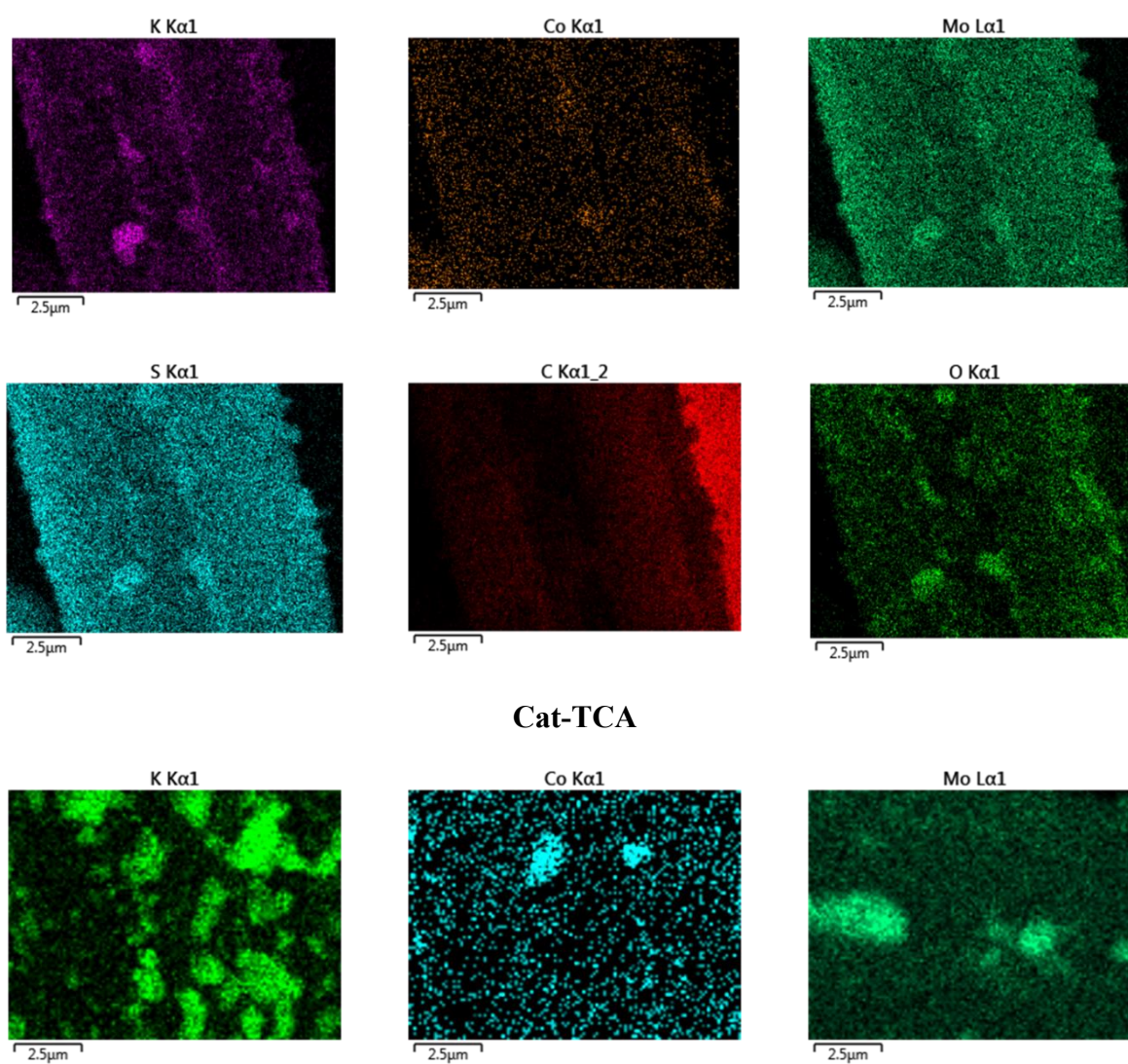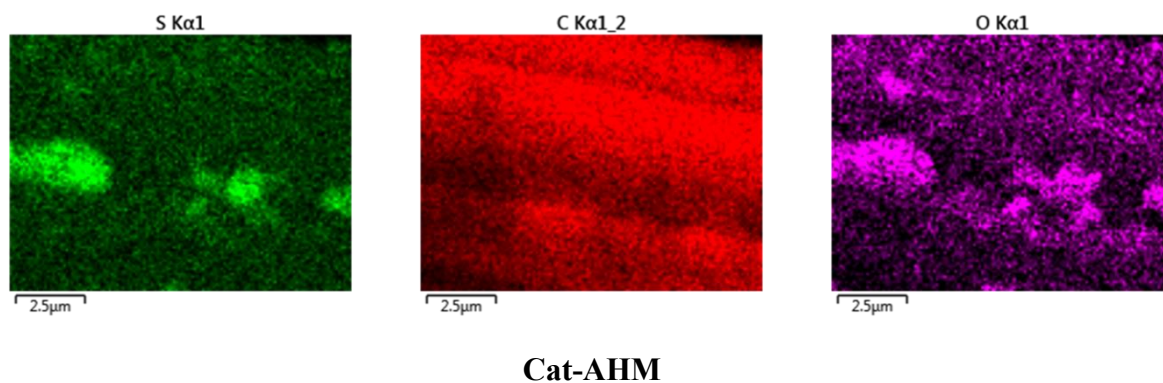
Figure 3.39. The EDX maps of the K-CoMoS$_2$ catalysts supported on fiber commercial activated carbons

Representative TEM micrographs of the supported-K-CoMoS$_2$ catalysts are shown in Fig. 3.40.
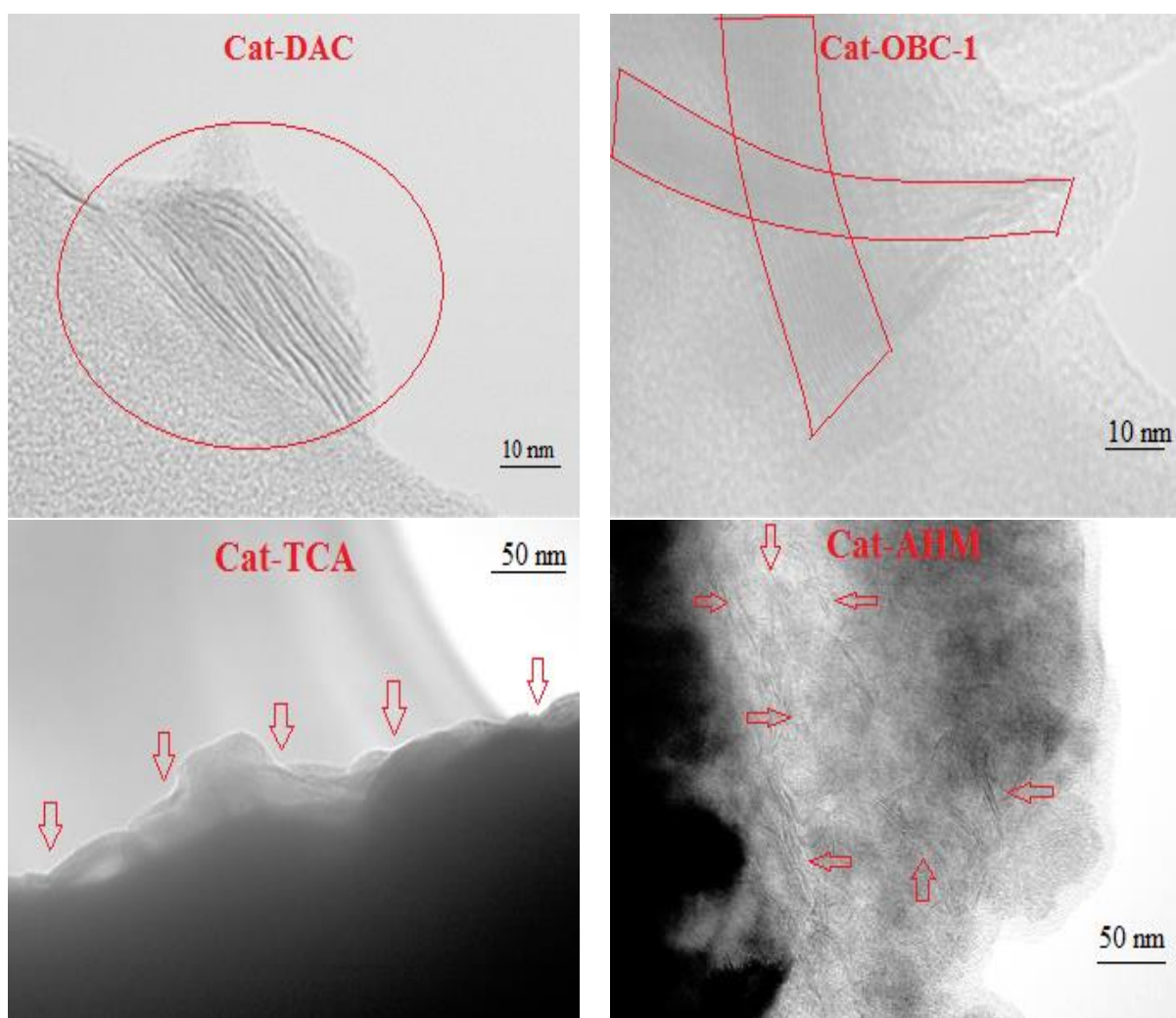
Figure 3.40. TEM images of the supported-K-CoMoS$_2$ catalysts

The MoS$_2$ slabs appear clearly as threadlike fringes in multilayer particles of the K-CoMoS active phase with different stacking degrees. The differences between the catalysts understudy can be attributed to the interaction between the K-CoMoS active phase and activated carbons.[147,160] Moreover, the MoS$_2$ crystallites display filamentous morphology on the surface of fiber activated carbons (TCA and AHM). The surface of AHM is more tangled compared to TCA, thus leading to tangled MoS$_2$ slabs on AHM and long linear slabs on TCA with long rim sites. It is notable to mention that increasing the stacking degree leads to an increase in vacancies and corner sites in the active phase, which decreases adsorption of hydride hydrogen,[150,160] whereas increasing the rime sites of MoS$_2$ slabs promotes the hydrogenation reaction.[91,164-165]

Chemical species present on the surface of the K-CoMoS$_2$ supported catalysts were evaluated by XPS. Fig. 3.41 shows typical XPS spectra for the Mo 3d region. The Mo 3d spectra contain two Mo 3d doublets. The Mo 3d$_{5/2}$ and 3d$_{3/2}$ doublet with BE at 228.7 and 232.0 eV, respectively, corresponds to the Mo^{4+} in MoS$_2$ phase species.[166] The doublet with BE equal to 232.8 and 235.9 eV belongs to the Mo^{6+} oxide species. The peak at BE of 226.0 eV is assigned to S 2s.
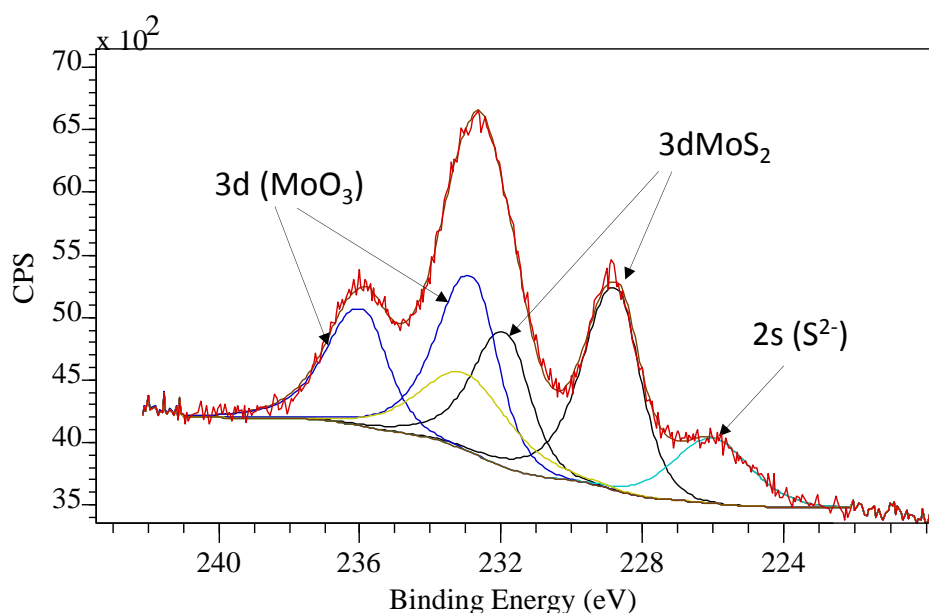
Figure 3.41. XPS Mo 3d spectra for sulfided K-CoMoS$_2$/OBC-1 catalyst.

For all catalysts the contributions of K $2p_{3/2}$ and S $2p_{3/2}$ at the ranges of 292.5–293.0 and 162.0 eV, respectively, were also detected and corresponded to K^+ and S_2- states.[91] In the sulfur spectra there was also observed a contribution of SO_4^{2-}, which is ordinary for K-doped TMS catalysts. The sulfidation degree of the metal (Table 3.11) was equal for all the samples – relative concentrations of MoS_2 and CoS_x (CoMoS) were in the range of 50–55 and 30-35 rel. %.

Table 3.11. Sulfidation degree of Mo and Co on the catalyst surface from XPS

Sample	Sulfidation degree of metal (%)		S/(Mo+K+Co) ratio
	Mo	Co	
K-CoMoS$_2$/DAC	54	32	1.3
K-CoMoS$_2$/OBC-1	52	30	0.9
K-CoMoS$_2$/TCA	56	31	1.0
K-CoMoS$_2$/AHM	55	35	1.5

The catalytic performance of supported K-CoMoS$_2$ catalysts at 300, 320, 340, and 360 ^{o}C are represented on Fig. 3.42.
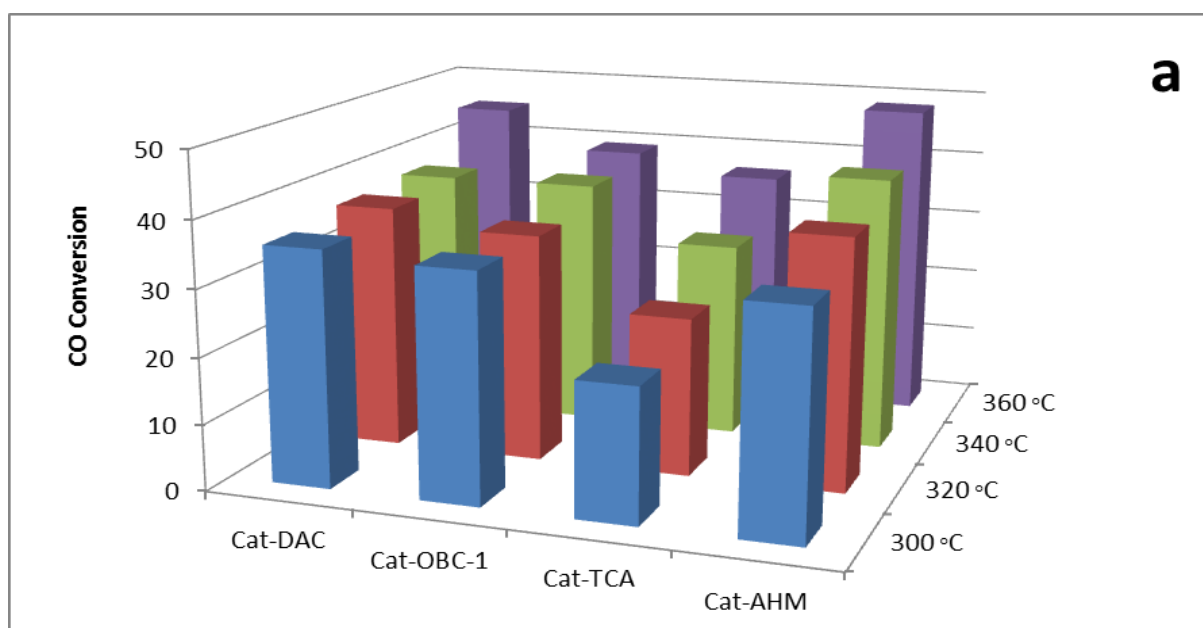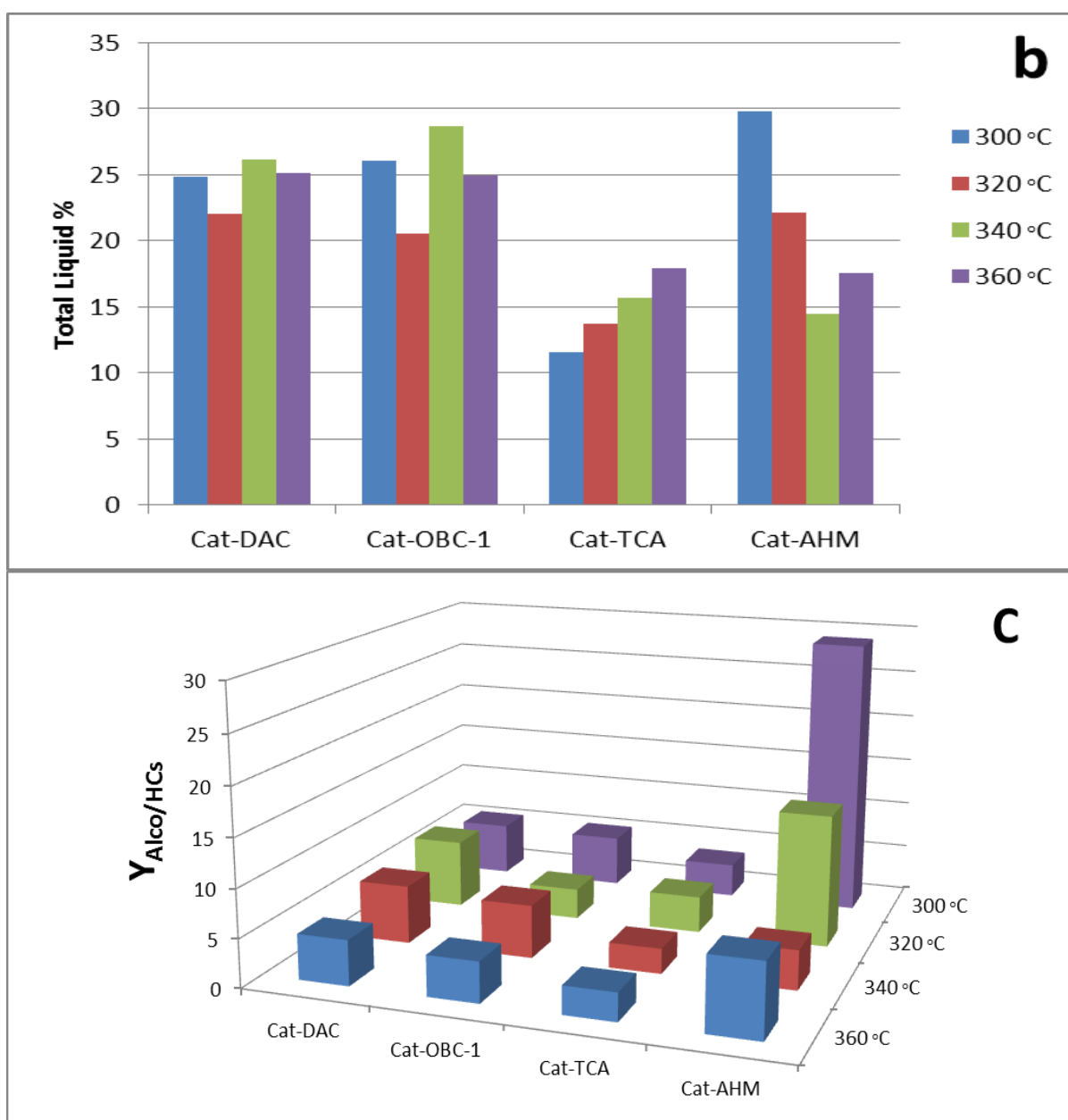
Figure 3.42. The HAS results of supported-K-CoMoS$_2$ catalysts. *a)* CO conversion; *b)* total liquid yield; *c)* yield ratio between alcohols and hydrocarbons. Reaction conditions: T = 300–360 ^{o}C, P = 5 MPa, GHSV = 760 L h^{-1} (kgcat)$^{-1}$, H$_2$/CO = 1.0.

Syngas conversion depends on the differences in surface morphologies of the supports and catalysts and the degree of interaction between the support and active phase. The results in Fig. 3.42 *a* revealed that the positive correlation between CO conversion and temperatures of the catalysts under study. CO conversion increases in the order Cat-TCA < Cat-OBC-1 < Cat-DAC < Cat-AHM. *Claure et al.*[147] and *Niannian et al.*[150] concluded that MoS$_2$ catalysts with short MoS$_2$ layers had higher selectivity for syngas conversion and HAS. Based on these

reports, we believed that these short and thin layers of the Cat-AHM catalyst could increase ratios of basal, corner and edge sites of the catalyst, which is producing more active sites and then improving the catalytic activities, particularly in HAS. In contrast, the lowest catalytic activities of Cat-TCA can be attributed to elongated slabs formed on the strip axial arrangement surface of commercial TCA based on activated carbon. In the previous section (part 3.2), we found an unusual correlation between catalytic performance of supported $K-CoMoS_2$ and the micro- and mesopore structure of the catalyst support. It was found that catalysts supported on microporous materials possessed higher catalytic activity in HAS synthesis from syngas than those supported on mesoporous materials. The catalytic performance results (Figs. 3.42 a, b, c) of powder activated carbons (Cat-DAC and Cat-OBC-1) corroborate the validity of this unusual finding because microporous Cat-DAC with the lower number of smaller mesopores was found to be more active than Cat-OBC-1 characterized by the higher number of mesopores (see Fig. 3.35). *Surisetty et al.*[4] reported that dispersion of K-CoMoS on mesoporous MWCNT is lower than on microporous AC. Lower catalytic activity of Cat-OBC-1 compared to Cat-DAC-1 can be attributed to the agglomeration of the active phase (see Figs. 3.35 and 3.38) that increased the number of rim sites and coupling of the sites important for HAS (basal, corner and edge sites). [5,6,133,158,159] Fig 3.42 b revealed that there is no clear correlation between temperature and total liquid yield. $K-CoMoS_2$ catalysts supported on powder ACs (Cat-DAC; Cat-OBC-1) yielded more total liquids than fiber ACs (Cat-TCA; Cat-AHM). The highest TLY% was observed over Cat-AHM at 300 ^{o}C. From Fig 3.42 c, the highest $Y_{Alco/HCs}$ was achieved at 340 ^{o}C for powder ACs and at 300 ^{o}C for the catalysts supported on fiber ACs. It can be seen that $Y_{Alco/HCs}$ displayed the descending order of Cat-AHM > Cat-DAC > OBC-1 > Cat-TCA. The current results were compared with those in several studies of HAS from syngas over supported and unsupported $CoMoS_2$ catalysts (see Table 3.12). Noteworthy is that the catalyst was not deactivated at the end of the reaction, which indicates its stability and repeatability.

Table 3.12. Comparison of support nature, reaction conditions and catalytic properties in HAS from synthesis based on K-CoMoS$_2$ catalysts taken from literature with current study.

Type of support	Active phase	Preparation Method	Reaction conditions				CO (%)	Total liquid selectivity (%)	Reference
			P, (MPa)	T, (°C)	GHSV (h^{-1})	H$_2$/CO			
unsupported		hydrothermal synthesis					29	30	
unsupported		coprecipitation	6.0	340	2000	2	35	35	[160]
unsupported		reverse microemulsion					39	60	
Al$_2$O$_3$			5.0	340	760	1	23	48	[159]
Al$_2$O$_3$/C (≈1%)			5.0	340	760	1	19.2	65	[114]
MWCNT	K-CoMoS	Wetness impregnation	8.3	320	1200	1	25	40	[6]
AC-Darco[*]							35.6	24.8	
AC-RX3 Extra[**]			8.27	330	1200	2	39.6	25.8	[4]
AC-CGP Super[***]							44.5	27.5	
Current Cat-DAC							45.3	55.3	
Current Cat-OBC-1			5.0	360	760	1	39.3	54	-
Current Cat-TCA							36.36	48.7	
Current Cat-AHM							48.5	63.4	

AC-Darco[*] is activated carbon purchased from Aldrich, Canada.
AC-RX3[**] and AC-CGP[***] Super are commercial ACs were obtained from Norit, USA.

The obtained results in Table 3.8 indicate that the current novel commercial activated carbons are promising supports for HAS because K-CoMoS$_2$ catalysts supported on novel commercial activated carbons (DAC, OBC-1, TCA, AHM) show the best CO conversion and TLY% in the optimum conditions compared to the findings in the relevant published studies (see Table 3.12), except for the results on unsupported K-CoMoS$_2$ prepared by a reverse microemulsion method.[150] However, this method is considered expensive as compared to the wetness impregnation method we used, which is highly feasible and was used in many experiments for catalyst preparation in petrochemical industry and petroleum products treatment. Gaseous and alcohol product yields in syngas conversion are presented in Table 3.13.

Table 3.13. The yield of hydrocarbons, carbon dioxide and each alcohol

T, °C	C1 (%)	CO$_2$ (%)	C2 (%)	C3 (%)	C4 (%)	MeOH (%)	EtOH (%)	PrOH-1 (%)	BuOH-1 (%)	i-BuOH (%)	AmOH-1 (%)	i-AmOH (%)
Cat-DAC												
300	1.5	4.4	1.6	2.0	1.3	4.0	10.6	5.9	1.8	1.3	0.5	0.6
320	0.7	4.5	1.1	2.4	0.4	4.6	12.0	6.7	2.0	1.5	0.6	0.7
340	1.3	7.2	1.3	0.8	0.9	4.3	11.2	6.2	1.9	1.4	0.5	0.7
360	2.4	11.9	2.0	1.0	0.3	4.1	10.7	6.0	1.8	1.4	0.5	0.7
Cat-OBC-1												
300	0.1	4.5	1.1	2.2	0.6	5.9	9.1	5.8	1.6	2.3	0.4	0.8
320	0.5	4.9	1.2	3.1	1.6	4.7	7.2	4.6	1.3	1.8	0.3	0.6
340	0.1	5.3	0.2	3.2	0.3	6.6	10.1	6,4	1.8	2.6	0.5	0.8
360	1.9	8.4	1.3	0.9	1.7	5.7	8.8	5.6	1.5	2.2	0.4	0.7
Cat-TCA												
300	1.0	5.4	1.5	0.4	0.4	2.3	5.2	2.2	0.7	0.6	0.2	0.4
320	1.6	6.6	1.4	0.3	0.3	2.7	6.2	2.6	0.9	0.7	0.2	0.4
340	2,3	8.6	1,9	0.8	0.4	3.1	7.1	3,0	1.0	0.8	0.3	0.5
360	3.7	12.0	0.4	1,8	1.0	3.5	8.0	3,4	1.1	0.9	0.3	0.6
Cat-AHM												
300	0.0	3.2	0.3	0.0	0.0	4.9	11.9	7.3	2.1	2.1	0.5	1.0
320	0.4	3.0	0.8	0,4	0.0	4.0	9.0	5.0	2.0	2.0	0.0	0.1
340	1.7	5.6	1.0	0.6	1.1	3.0	9.1	1.3	0.4	0.4	0.1	0.2
360	0.8	5.7	0.9	0.3	0.3	2.9	8.1	4.3	1.2	1.2	0.3	0.6

The nature of carriers used in the higher alcohol synthesis has a bearing on the extent of alcohol products distribution. Furthermore, the morphology and structure of the support directly affect its porosity and the ease of modifying its surface characteristics by functionalization.[133] As a result, the ability of the supports to disperse active metal species on the support can be influenced by their interaction with the K-CoMoS active phase. It is quite obvious that the products generated by DAC, OBC-1, TCA, and AHM-supported K-CoMoS$_2$ catalysts consisted mostly of light hydrocarbons (C1-C4) and linear alcohols with carbon numbers in the range of C1 to C5 (Table 3.13), a small amount of iso-alcohol, and carbon dioxide produced from the reaction between CO and vapor water. As can be seen, the yield of hydrocarbons and CO$_2$ showed a positive correlation with the temperature, whereas the yield of each alcohol has not displayed any correlation with the temperature. The highest yield for C$_{1+}$ and CO$_2$ was recorded over Cat-TCA, for C$_{2+}$ over Cat-DAC, and for C$_{3+}$ and C$_{4+}$ over OBC-1. Moreover, the total yield of hydrocarbons at 360 ^{o}C followed the trend Cat-TCA (6.9%) > Cat-OBC-1 (5.9%) > Cat-DAC (5.6%) > Cat-AHM (2.3%) (Table 3.13). Ethanol, propanol-1, and methanol were predominant alcohols in the final liquid products and the by-products comprised mainly butanol-1, isobutanol, amyl alcohol, and isoamyl alcohol. Propanol-2 and butanol-2 were not synthesized over supported CoMoS$_2$ catalysts in all reaction conditions. These results look different compared with the other studies that used activated carbon as a support for HAS form syngas over K-modified CoMoS$_2$ catalysts.[4,23] The orders of catalysts for synthesizing each alcohol are: for ethanol, propanol-1, and butanol-1 (Cat-DAC > Cat-AHM> Cat-OBC-1 > Cat-TCA); for methanol (Cat-OBC-1 > Cat-DAC> Cat-AHM > Cat-TCA); for amyl alcohol-1 (Cat-DAC > Cat-OBC-1 > Cat-AHM > Cat-TCA); for isobutanol and isoamyl alcohol (OBC-1 > TCA > DAC > AHM) (see Table 3.13). Values of selectivity towards light hydrocarbons and alcohols are presented in Fig. 3.43.
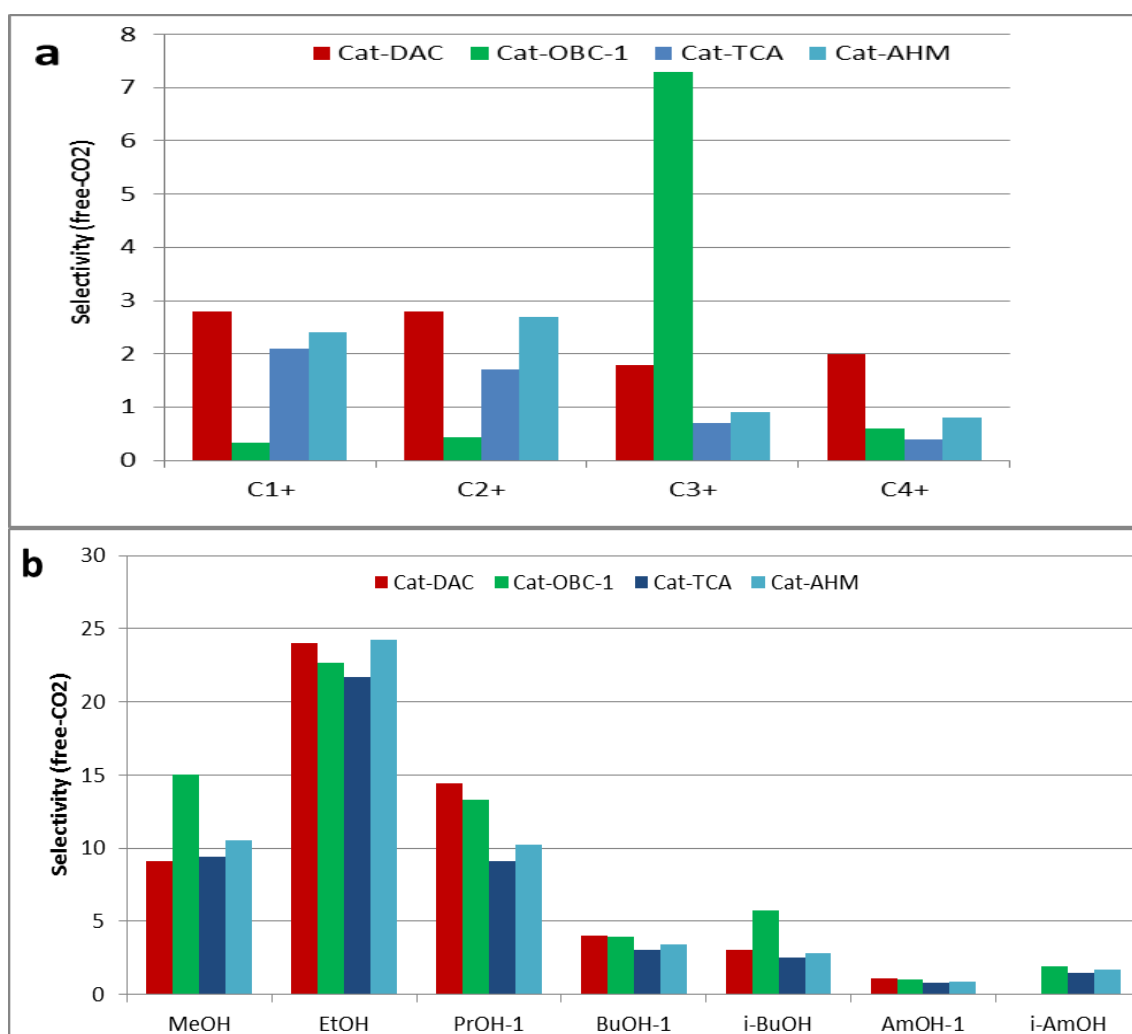
Figure 3.43. Product selectivity of supported catalysts towards a) light hydrocarbons (C1-C4); b) methanol, ethanol, propanol-1, amyl alcohol, butanol-1, Isobutanol, and isoamyl alcohol. Reaction condition: $H_2/CO = 1.0$, GHSV = 760 L h^{-1} (kgcat)$^{-1}$, T = 340 ^{o}C, P = 5 MPa.

This investigation examined the effect of the support on the product selectivity. The selectivity for C_{1+} and C_{2+} was found to be higher than that for C_{3+} and C_{4+} for all catalysts, except the highest selectivity of Cat-OBC-1 towards C_{3+} (Fig. 3.43). The latter may be due to the mesoporosity of the catalyst surface, which involves more acid sites with the partial cover of MoS_2 crystallite edges, as well as the active phase agglomeration, which suggests a somewhat higher hydrogenation ability with more isomerization. The powdered activated carbon supported catalysts (Cat-DAC; Cat-OBC-1) show higher selectivity than fiber activated carbons (Cat-TCA; Cat-AHM) towards C_{3+}, C_{4+}, propanol-1, butanol-1, isobutanol, and amyl alcohol-1 (Fig. 3.43). In contrast, the highest selectivity for

ethanol was found over Cat-AHM, which might be attributed to the higher stacking number of MoS_2 crystallite as a result of the tangled surface morphology of AHM, which led to the formation of considerable amounts of vacancies and corner sites favourable for the higher alcohol selectivity in general and ethanol in particular. For powdered activated carbons, the catalyst that contains the highest number of micropores (Cat-DAC) produced a considerable amount of liner alcohols compared with Cat-OBC-1. Microporous catalysts inhibit isomerization due to steric constraints. The latter finding is consistent with our results discussed in paragraph 3.2. This interpretation does not apply to the methanol synthesis over Cat-OBC-1 because it possessed more mesopores. We presumed that the difference in the porosity of the catalysts did not affect the methanol synthesis due to the small size of CH_3^+ and its stereo structure, which is why it could easily undergo adsorption, as compared to other linear alcohols.

CONCLUSION

1.	The influence of the support in the reaction of higher alcohols synthesis from synthesis gas on supported $K-CoMoS_2$ catalysts was studied. Gamma alumina, gamma alumina coated with carbon (CCA), and two types of activated carbons – of mineral origin (AG-3) and birch wood (BAW) were used as supports. Catalytic activity increased in inverse proportion to the logarithm of the number of acid sites on the catalyst in order Al_2O_3 < CCA < AG-3 < BAW. The observed high selectivity for the formation of alcohols on catalysts supported on activated carbon is due to the large linear size and number of layers of the $K-CoMoS_2$ crystallite compared to the crystallites of the active phase of catalysts supported on acid supports based on alumina.

2.	It was shown that catalysts supported on microporous materials (AG-3 and BAW) are more active in the synthesis of higher alcohols and their further conversion to other oxygenates than similar catalysts supported on mesoporous highly acidic supports (Al_2O_3 and CCA).

3.	A relationship between the pore size and the acidity of the studied carriers has been established. An explanation for this phenomenon is given in terms of differences in the acidity of carriers and the formation of agglomerates consisting of hundreds and thousands of molybdenum sulfide clusters on the surface of microstructured low acid carriers and the formation of highly dispersed single clusters inside the mesopores of high acid carriers. The acidity enhances the strength of the bond between the particles of the active phase and the carrier and, as a result, hinders the formation of new vacancies in the catalytic cycle. Low acidity promotes the weakening of the bond between the particles of the active phase and the support, and thus facilitates the formation of new vacancies.

4.	It is shown that, under certain conditions, large agglomerates of particles of the active phase, weakly bound to the carrier, are more active than highly dispersed single clusters, strongly bound to the carrier.

5. A positive correlation between the selectivity of linear primary alcohols and amount of graphene was observed. Higher catalytic activity of Cat-GCA1 (1.7%) compared to Cat-CCA (1.7%) is attributed to the particle distributions of Cat-GCA1, it shows the highest stacking number and slab length.

6. The results obtained from catalysts supported on fiber activated carbons showed that the short and thin layers of the Cat-AHM catalyst increase corner, basal and edge sites on the catalyst surface that form more active MoS_2 crystallites, which then increases catalytic activity, particularly in HAS. In contrast, the lowest catalytic activity of Cat-TCA can be attributed to long linear slabs formed on the strip axial arrangement surface of TCA based on commercial activated carbon.

RECOMMENDATIONS

The study provides both academic and manufacturing community with a significant insight into the improvement of K-modified $CoMoS_2$ catalysts supported on different carbon containing materials which would be stable, active and selective in higher alcohols synthesis from syngas. Moreover, it explains the correlation between catalytic performance and textural characteristics. However, some recommendations can be suggested for further studies:

➤ Catalytic performance and selectivity depend on preparation methods and precursors. Herein, supported K- modified MoS_2 catalysts were synthesized by wetness impregnation using an organic precursor, and then were sulfided by H_2S. In order to increase activity and selectivity of supported-K-$CoMoS_2$ catalysts, other preparation methods can also be used and compared, such as chemical vapour deposition (CVD) and sol gel techniques. Additionally, other precursors (organic and inorganic) can be used for the synthesis of catalysts.

➤ Several physical and chemical characterizations of the supported-K-$CoMoS_2$ catalysts were carried out using methods such as N_2 physiosorption, SEM,

EDX, TEM, XPS, etc. We suggest analyzing the catalysts during and after the catalytic reaction, since the structure of supported-K-CoMoS$_2$ catalysts can change in the course of the reaction, in order to identify the best catalyst before proceeding to large-scale synthesis.

➢ The extended X-ray absorption fine structure (EXAFS) technique can be used to characterize different metal species existent on the surface of the catalyst and to identify the structure of the catalyst's surface, including slab lengths, coordination numbers, and bond lengths. These parameters can help understand the correlation between catalyst performance and the surface structure.

➢ Carbon on CCA decreases the interaction between the active phase and alumina alongside with the hydrogen spillover. Carbon does not coat the surface of alumina uniformly when its content is below 5 wt%, as organic precursors adsorb preferably on Lewis sites and block them. Oxidic precursors for the active phase can only adsorb on the remaining carbon-free alumina surface, leading to sulfide crystallites with a higher stacking number. The optimum wt. % of graphene can be characterized by applying different wt. % from 0.4 to 7% aiming to increase the selectivity of higher alcohols.

➢ In this study, carbon monoxide (pure) and hydrogen were used as a feed gas for HAS. However, the syngas obtained from brown coal or biomass, may be contaminated with e.g. hydrogen disulfide, carbon dioxide, water, and nitrogen compounds. These impurities can affect catalytic activity and selectivity of higher alcohols or deactivate the catalysts. Therefore, we suggest that the catalytic reaction should be carried out using commercial syngas from biomass or coal gasification before the scale-up.

LIST OF ABBREVIATIONS

BP	British Petroleum Agency
Rosstat	Federal State Statistics Service for the Russian Federation
SPFCs	Solar-Powered Electrochemical Cells
HAS	Higher Alcohol Synthesis
FTS	Fischer-Tropsch Synthesis
BFB	Bubbling Fluidized Bed
CFB	Circulating Fluidized Bed
ICE	Internal Combustion Engine
MON	Motor Octane Number
FFV	Flexible Fuel Vehicles
TMS	Transition metal sulfide catalysts
MS systems	Methanol synthesis systems
DFT	Density-functional theory
CUS	Coordinated Unsaturated Sites
FE-SEM	Field-Emission Scanning Electron Microscopy
EDX	Energy Dispersive X-ray technique
TEM	Transmission Electron Microscopy technique
CCA	Carbon coated alumina
GCA	Graphene coated alumina
CVD	Chemical vapor deposition
EXAFS	Extended X-ray absorption fine structure
BET	Brunauer-Emmett-Teller surface area
BE	Bond energy

RESEARCH OUTCOME

A. Publications from this thesis (Scopus and Web of science):

1. *Osman, M.E.,* Maximov, V.V., Dorokhov, V.S., Mukhin, V.M., Sheshko, T.F., Kooyman, P.J., Kogan, V.M. Carbon-Supported K-CoMoS$_2$ for Alcohol Synthesis from Synthesis Gas // *Catalysts*, **2021**, 11, 1321, https://doi.org/10.3390/catal11111321.

2. *Osman M.E,* Maximov V.V, Dipheko T.D., Sheshko T.F, Cherednichenko A.G., Nikulshin P.A., Kogan V.M. Synthesis of Higher Alcohols from Syngas Over K-modified CoMoS$_2$ Catalyst Supported on Novel Powder and Fiber Commercial Activated Carbons // *Omega ACS*, **2022**, 7, 24, 21346–21356, https://doi.org/10.1021/acsomega.2c03082.

3. *Osman M.E.,* Maximov V.V., Dipheko T.D., Permyakov E.A., Sheshko T.F., Cherednichenko A.G., Kogan V.M. Effect of textural characteristics on the catalytic performance of supported-K-CoMoS$_2$ in higher alcohols synthesis from syngas // *Mendeleev Communications*, **2022**, 32, 4, 510 –513, https://doi.org/10.1016/j.mencom.2022.07.

4. *Osman M.E.,* Dipheko T.D., Maximov V.V., Sheshko T.F., Trusova E.A., Cherednichenko A.G., Kogan V.M. Syngas and ethanol conversion into higher alcohols over K-CoMoS$_2$–catalysts supported on graphene nanosheets // *Chemical Engineering Communications*, 2022, DOI: 10.1080/00986445.2022.2116323.

B. Abstracts and materials presented at international conferences (presenting author*)

 5. *Osman, M.E.,** Maximov, V.V., Dorokhov, V.S., Mukhin, V.M., Sheshko, T.F., Kooyman, P.J., Kogan, V.M. Influence of carbon-containing materials as support for K-CoMoS$_2$ catalyst on synthesis of alcohols from syngas // The 6th International Conference on Chemical Materials and Process (ICCMP 2020), Warsaw, Poland, July 2-4, 2020, (Online).

6. *Osman M.E.,** Maximov V.V., Sheshko T.F., Kooyman P.J., Mukhin V.M., Trusova E.A., and Kogan V.M. The role of carbon-containing materials as supports for K-CoMoS$_2$ catalyst on synthesis of alcohols from syngas // 1st International Electronic Conference on Catalysis Sciences, MDPI, USA, November 10-30, 2020, (online). https://doi.org/10.3390/ECCS2020-08008.

7. *Osman M.E.,** Maximov V.V., Sheshko T.F., Trusova E.A., Kogan V.M. Syngas conversion to higher alcohols: application of K-promoted CoMoS$_2$ catalysts supported over Novel carbon-Containing Materials // 7th Edition of International Conference on Catalysis, Chemical Engineering and Technology– 2021 (CCT 2021), Tokyo, May 17 – 18, 2021, (online).

8. *Osman M.E.,** Maximov V.V., Dorokhov V.S., Popov M.V., Sheshko T.F., Trusova E.A., Kogan V.M. Synthesis of higher alcohols from syngas over K-modified CoMoS2 catalyst supported on carbon-containing material // Catalysis for a Sustainable World Conference, RUDN University, December 22-24, 2020.

9. Kogan V.M.,* *Osman M.E.*, Dipheko T.D., Maximov V.V., Dorokhov V.S., Permyakov E.A., Sheshko T.F., Cherednichenko A.G. Alkali-modified transition matel sulfide catalysts supported on carbon materials for syngas conversion into higher alcohols and other oxygenates: Mechanistic aspects // Catalysis for a Sustainable World Conference, RUDN University, 2020, 35-37.

10. *Osman M.E.,** Maximov V.V., Dipheko T.D., Sheshko T.F., Cherednichenko A.G., Nikulshin P.A., Kogan V.M. Study the role of carbon and nano-composite hybrid materials as a support for transitional metal sulfide-based catalysts for higher alcohols synthesis from syngas // 11th Edition of International Conference on Catalysis, Chemical Engineering and Technology, Japan, May 16-17, 2022, (Online).

11. Кумбатова А.С., Симутина А.С., Маркова Е.Б.,* *Осман М.*, Чередниченко А.Г. Модифицирование оксида алюминия дисульфидом молибдена и атомами кобальта для процесса дегидрирования // XII Российской конференции (с международным участием): Актуальные Проблемы Нефтехимии, ИНХС РАН, Россия, 2021.

12. ***Osman M.E.*,*** Maximov V.V., Dipheko T.D., Sheshko T.F., Cherednichenko A.G., Kogan V.M. Study the role of carbon containing materials as support for K-CoMoS$_2$ catalysts in HAS from syngas // The Sixth International Scientific Conference "Advances in Synthesis and Complexing". RUDN University, September 26-30, 2022. P 401.

13. ***Osman M.E.*,*** Maximov V.V., Dipheko T.D., Sheshko T.F., Cherednichenko A.G., Kogan V.M. HAS from syngas over supported and modified TMS catalysts: Effect of novel fiber and powder commercial activated carbon supports // The Sixth International Scientific Conference "Advances in Synthesis and Complexing". RUDN University, September 26-30, 2022. P 402.

14. ***Osman M.E.*,*** Maximov V.V., Dipheko T.D., Sheshko T.F., Cherednichenko A.G., Kogan V.M. Production of higher alcohols from syngas and ethanol using K-modified TMS–catalysts supported on graphene nanosheets // The Sixth International Scientific Conference "Advances in Synthesis and Complexing". RUDN University, September 26-30, 2022. P 403.

15. Repev N.A.,* ***Osman M.E.*** , Konopatsky A.S., Maximov V.V., Dipheko T.D., Kogan V.M. Catalytic activity of supported-K-CoMoS$_2$ catalysts in HAS from Syngas: Impact of sulfidation method // The Sixth International Scientific Conference "Advances in Synthesis and Complexing". RUDN University, September 26-30, 2022. P 439.

REFERENCES

[1] Subramani V. and Gangwal S. K. A Review of Recent Literature to Search for an Efficient Catalytic Process for the Conversion of Syngas to Ethanol // *Energy & Fuels,* **2008**, 22, 814-839.

[2] Surisetty V.R., Dalai A.K., Kozinski J. Alcohols as alternative fuels: An overview // *Appl. Catal. A Gen*., **2001**, 404, 1–11.

[3] Woo H.C., Nam I. -S., Lee J. S., Chung J. S., Kim Y. G. Structure and distribution of alkali promoter in K/MoS_2 catalysts and their effect on alcohol synthesis from syngas // *J. Catal*., **1993**, 142, 672–690.

[4] Surisetty R., Dalai A. K., Kozinski J. Influence of porous characteristics of the carbon support on alkali-modified trimetallic Co–Rh–Mo sulfided catalysts for higher alcohols synthesis from synthesis gas // *Applied Catalysis A: General*, **2011**, 393, 50–58.

[5] Surisetty V. R., Tavasoli A., Dalai A. K. Synthesis of higher alcohols from syngas over alkali promoted MoS_2 catalysts supported on multi-walled carbon nanotubes // *Applied Catalysis A: General*. **2009**, 365,243–251.

[6] Maximov V. V., Permyakov E., Dorokhov V. A., Wang Y., Kooyman P. J., Kogan V. M. Effect of Promoter Nature on Synthesis Gas Conversion to Alcohols over $(K)MeMoS_2 /Al_2O_3$ Catalysts // *ChemCatChem*, **2020**, 12, 1443– 1452.

[7] Liu Z., Li X., Close M. l. R., Kugler E. L., Petersen J. L., Dadyburjor D. B.; Screening of alkali-promoted vapor-phase-synthesized molybdenum sulfide catalysts for the production of alcohols from synthesis gas // *Ind. Eng. Chem. Res.* **1997**, 36, 3085-3093.

[8] Surisetty V. R, Eswaramoorthi I, Dalai A. K. Comparative study of higher alcohols synthesis over alumina and activated carbon-supported alkali-modified MoS_2 catalysts promoted with group VIII metals // *Fuel*, **2012**, 96, 77–84.

[9] Lva, M.; Xie, W.; Sun, S.; Wu, G.; Zheng, L.; Chu, S.; Gao, C.; Bao, J. Activated-carbon-supported K-Co–Mo catalyst for synthesis of higher alcohols from syngas // *Catal. Sci. Technol.*, **2015**, 5, 2925–2934.

[10]   Iranmahboob J., Hill D. O. Oxidative dimerisation of methane on supported palladium oxide catalysts // *Catal Lett.* **2002**, 4, 1, 49–55.

[11]   Dorokhov V.S., Permyakov E.A., Nikulshin P.A., Maximov V.V., KoganV.M. Experimental and computational study of syngas and ethanol conversion mechanisms over K-modified transition metal sulfide catalysts // *J. Catal.,* **2016**, 344, 841–853.

[12]   Badwal S. P. S., Giddey S., Kulkarni A., Goel J, Basu S. Direct ethanol fuel cells for transport and stationary applications – A comprehensive review // *Appl. Energy*, **2015**, 145, 80–103.

[13]   Kohl A., Linsmeier C., Taglauer E., Knozinger H. Influence of Support and Promotor on the. Catalytic Activity of Rh/VOx/SiO2 Model Catalysts // *Phys. Chem.,* **2001,** 3, 4639–4643.

[14]   Tauster S.J., Fung S. C., Baker R. T. K., Horsley J. A. Strong Interactions in Supported-Metal Catalysts // Science, 1981, 211, 1121–1125.

[15]   Kiennemann R. A. Characterization of Chemisorbed Species in CO/H_2 and CO_2/H_2 Reactions: Evolutive Behaviour of the Species // *Can. J. Chem. Eng.*, **1983**, 61, 21-28.

[16]   Li, D., Li, R., Lu, M., Lin, X., Zhan, Y., Jiang, L. Carbon dioxide reforming of methane over Ru catalysts supported on Mg-Al oxides: A highly dispersed and stable Ru/Mg(Al)O catalyst // *Appl. Catal. B-Environ.* **2017**, 200, 566–577.

[17]   Ma, Z., Dai, S. Development of novel supported gold catalysts: A materials perspective // *Nano Res.* **2011**, 4, 3–32.

[18]   Hosseinia S. A., Taeba A., Feyzia F., Yaripour F. Fischer–Tropsch synthesis over Ru promoted $Co/\gamma\text{-}Al_2O_3$ catalysts in a CSTR // *Catalysis Communications*, **2004**, 5, 137–143.

[19]   Zhang C., Chen L., Cheng H., Zhu X., QiV Z. Atomically dispersed Pd catalysts for the selective hydrogenation of succinic acid to γ-butyrolactone // *Catalysis Today*, **2016**, 276, 55-61.

[20]   Andersson R., Boutonnet M., Jaras S. Correlation patterns and effect of syngas conversion level for product selectivity to alcohols and hydrocarbons over molybdenum sulfide based catalysts // *Appl. Catal., A: Gen.*, **2012**, 417–418, 119–128.

[21]   Zaman S. and Smith K. J. A Review of Molybdenum Catalysts for Synthesis Gas Conversion to Alcohols: Catalysts, Mechanisms and Kinetics // *Catalysis Reviews*, **2012**, 54, 1, 41-132.

[22]   Surisetty V. R, Eswaramoorthi I, Dalai A. K. Comparative study of higher alcohols synthesis over alumina and activated carbon-supported alkali-modified MoS_2 catalysts promoted with group VIII metals // *Fuel*, **2012**, 96, 77–84.

[23] Permyakov E.A., Dorokhov V.S., Maximov V.V., Nikulshin P.A., Pimerzin A.A., Kogan V.M. Computational and experimental study of the second metal effect on the structure and properties of bi-metallic MeMoS-sites in transition metal sulfide catalysts // *Catal. Today*, **2018**, 305: 19-27.

[24] Anashkin Y. A. V., Ishutenko D. I., Maximov V. V., Pimerzin A. A, Kogan V. M., Nikulshin P. A. Effect of carrier properties on the activity of supported K-CoMoS catalysts in the synthesis of alcohol from syngas // *Reaction Kinetics, Mechanisms and Catalysis*, *2019*, 5. 11335-11347.

[25] Key World Energy Statistics // International Energy Agency, Paris, **2016**.

[26] Boman, C., Nordin, A., Boström, D., Öhman, M. Characterization of inorganic particulate matter from residential combustion of pelletized biomass fuels // Energ. *Fuel*, **2004**, 1, 338–348.

[27] Ciferno J. P, Marano J. J. Benchmarking biomass gasification technologies for fuels, chemicals and hydrogen production // *US Dep Energy Natl Energy,* **2002**, 58.

[28] Klass, D. L. Biomass for renewable energy and fuels chemicals // *Encyclopedia of Energy,* **2004**, 1, 193-212.

[29] Kuester, J. L. Conversion of guayule residues into fuel energy products // *Bioresource Technol.* **1991**, 35, 217-222.

[30] Courty, P.; Chaumette, P., Syngas: A Promising Feedstock in the Near Future // *Energy Prog*. **1987**, 23-30.

[31] Sieger, R.; Brady, P. Thermal Oxidation of Sewage Solids: White Paper on Bio-gasification and Other Conversion Technologies, Water Environment Federation // *Residuals and Biosolids Committee*, **2003**.

[32] Radakovits R., Jinkerson R. E., Darzins A., Posewitz M. C. Genetic Engineering of Algae for Enhanced Biofuel Production // *Eukaryotic Cell*. **2010**, 9, 4, 486–501.

[33]   Smith A. M. Whittaker C, Shield I. R, Andrew B. The potential for production of high quality bio-coal from early harvested Miscanthus by hydrothermal carbonization // *Fuel*. **2012**, 220: 546–557.

[34]   Linares-Pastén, J. A., Andersson, M, Nordberg karlsson, E. Thermostable glycoside hydrolases in biorefinery technologies // *Current Biotechnology*, **2014**, 3, 1, 26–44.

[35]   Springsteen B., Christofk, T., Eubanks E., Mason T., Clavin C., Storey B. Emission Reductions from Woody Biomass Waste for Energy as an Alternative to Open Burning // *Journal of the Air & Waste Management Association*, *2011*, 61, 1, 63–68.

[36]   Wyatt T. The Russian Far East's illegal timber trade: an organized crime? // *Crime, Law and Social Change*. **2014**, 61, 1, 15–35.

[37]   Overland I. The Siberian Curse: A Blessing in Disguise for Renewable Energy? // *Sibirica*, **2010**, 9, 2, 1–20.

[38]   Pristupa A. O, Mol A. P. J. Renewable energy in Russia: the take-off in solid bioenergy? // *Renew Sustain Energy Rev*, **2015**, 50, 315–24.

[39]   Valentina S. Geothermal energy use in Russia // International Geothermal Conference, 2003, Retrieved 23 January **2011**.

[40]   Usachev, I. N., Shpolyanskiy, Y. B., Istorik, B. L., Kuznetsev, V. P., Fateev, V. N.; Knyazev, V. A. Приливные электростанции (ПЭС) — источник энергии, запасаемый в водороде [Tidal power plants (TPP) — a source of energy, store-able in hydrogen] // 2nd International Forum "Hydrogen technologies for developing world" (in Russian). Moscow, **2008**.

[41]   Boute, A. Off-grid renewable energy in remote Arctic areas: An analysis of the Russian Far East // *Renewable and Sustainable Energy Reviews*, **2016**, 59, 1029-1037.

[42]   BP, 2016. BP Statistical Review of World Energy, https://www.bp.com/content/dam/bp/pdf/ energy-economics/statistical-review-2016/bp-statistical review of worldenergy, **2016**.

[43]   Rosstat, 2016. Tekhnologicheskoe Razvitie Otraslei Ekonomiki (Technological Development of Industries), Moscow. ⟨http://www.gks.ru/wps/wcm/connect/rosstat_main/rosstat/ru/statistics/economydevelopment/⟩ > (accessed on 22 January 2017, in Russian).

[44]   Steubing B., Zah R., Waeger P., Ludwig C. Bioenergy in Switzerland: assessing the domestic sustainable biomass potential // *Renew Sustain Energy Rev*., **2010**, 14, 8, 2256–65.

[45]   Namsaraev Z. B., Gotovtsev P. M., Omova A.V., Vasilov K. R.G. Current status and potential of bioenergy in the Russian Federation // *Renewable and Sustainable Energy Reviews*, **2018**, 81,625–634.

[46]   Namsaraev Z. B., Gotovtsev P.M., Komova A.V., Borgolov A.V., Sergeeva J. S., Vasilov R. G. Estimation of raw materials sources in the Russian Federation for fuel and energy production from biomass; [In Russian] // *Bull Biotechnol Phys Chem Biol*, **2015**, 11, 4, 5–12, [In Russian].

[47]   Pristupa A. O., Mol A. P. J., Oosterveer P. Stagnating liquid biofuel developments in Russia: present status and future perspectives // *Energy Policy*, **2010**, 38, 7, 3320–8.

[48]   McKendry, P. Energy production from biomass (part 2): conversion technologies // *Bioresource Technol*. **2002**, 83, 47–54.

[49]   Franco, C., Pinto, F., Gulyurtlu, I., Cabrita, I. The study of reactions influencing the biomass steam gasification process // *Fuel*, **2003**, 82, 835–842.

[50]   Bain, R. L. An Introduction to Biomass Thermo-chemical Conversion, Biomass and Solar Energy Workshops // *National renewable Energy Laboratory*, **2004**.

[51]   Farzad S, Mandegari M. A, Görgens J. F. A critical review on biomass gasification, co-gasification, and their environmental assessments // *Biofuel Res J.*, **2016**, 3, 483–495.

[52]   Santos R. G .D, Alencar A. C. Biomass-derived syngas production via gasification process and its catalytic conversion into fuels by Fischer Tropsch synthesis: A review // *Int J Hydrogen Energy*, **2020**, 45, 18114–18132.

[53]   Waldheim L., Nilsson T. Heating value of gases from biomass gasification // IEA Bioenergy Agreement, Task 20 - Therm Gasif Biomass **2001**, 61.

[54]   Tran P. N. U., Vu L. V. K., Nguyen D. Q, et al. Energy balance of small-scale biorefinery system // *Environ Sci,* **2013**, 26, 489–496.

[55]   Mai T. P., Nguyen D. Q. Gasification of Biomass // *Biotechnological Applications of Biomass*, **2020**, DOI: 10.5772/intechopen.93954.

[56]   Rukshan J, Souman R. Numerical and Experimental Investigation of Equivalence Ratio (ER) and Feedstock Particle Size on Birchwood Gasification // *Energies, 2017*, 10, 1232-1236.

[57]   James A. M., Yuan W., Boyette M. D., et al. The effect of air flow rate and biomass type on the performance of an updraft biomass gasifier // *Bio Resources*, **2015**, 10, 3615–3624.

[58]   Cao Y, Wang Q, Du J, et al. Oxygen-enriched air gasification of biomass materials for high-quality syngas production // *Energy Convers Manag,* **2019**, 199, 111628.

[59]   Kumar A, Jones D. D, Hanna M. A. Thermochemical biomass gasification: A review of the current status of the technology // *Energies,* **2009**, 2,556–581.

[60]   Maschio G, Lucchesi A, Stoppato G. Production of syngas from biomass // *Bioresour Technol,* **1994**, 48, 119–126.

[61]   Favas J., Monteiro E., Rouboa A. Hydrogen production using plasma gasification with steam injection // *Int J Hydrogen Energy,* **2017**, 42, 10997–11005.

[62]   Fei Q., Guarnieri M.T.; Tao L., Laurens L. M. L., Dowe N., Pienkos P. T. Bioconversion of Natural Gas to Liquid Fuel: Opportunities and Challenges // *Biotech. Adv.*, **2014**, 32, 596- 614.

[63]   Julian R. H. Catalysis in Biomass Conversion // Ross, in Contemporary Catalysis: Elsevier **2019**.

[64]   Joo-Sik Kim, Gyung-Goo Choi, in Waste Biorefinery: Elsevier, 2018.

[65]   Smith J. L., Workman J. P., Drenth A., Cabot, P. Alcohol for motor fuels // *Service in action*; no. 5.010, **1980**.

[66]   Luk H. T., Mondelli C., Ferre D. C., Stewart J. A., Perez-Ramirez J. Status and prospects in higher alcohols synthesis from syngas // *Chemical Society Reviews*, **2017**, 46, 1358-1426.

[67]   DemİrbaŞ, A. Bioethanol from Cellulosic Materials: A Renewable Motor Fuel from Biomass // *Energy Sources*, **2005**, 27, 327-337.

[68]   Subramani, V., Gangwal, S. K. A Review of Recent Literature to Search for an Efficient Catalytic Process for the Conversion of Syngas to Ethanol // *Energy & Fuels,* **2008**, 22, 814-839.

[69]   Hansen A. C., Zhang Q., Peter W. L. Ethanol–diesel fuel blends - a review // *Bioresource Technol.* **2005**, 96, 277-285.

[70]   Christensen, J. M. Catalytic Synthesis of Long-Chained Alcohols from Syngas // PhD-Thesis, Department of Chemical and Biochemical Engineering, Technical University of Denmark, **2011**.

[71]   Agarwal A. K.. Biofuels (alcohols and biodiesel) applications as fuels for internal combustion engines // *Prog. Energ. Combust. Sci.* **2007**, 33, 233-271.

[72]   Brink A., Jordaan C. F. P., le Roux J. H., Loubser N. H. Carburetor corrosion: the effect of alcohol–petrol blends // In: Proceedings of the VII International Symposium on Alcohol Fuels Technology, Paris, France, **1986.**

[73]   Angelici C., Weckhuysen B. M., Bruijnincx P. C. A. Chemocatalytic Conversion of Ethanol into Butadiene and Other Bulk Chemicals // *ChemSusChem***, 2013**, 6, 1595–1614.

[74]   Mascal M . Chemicals from biobutanol: technologies and markets. Biofuels // *Bioproducts and Biorefining*, **2012**, 6, 483–493.

[75]   Goldemberg J. Ethanol for a sustainable energy future // *Science*, **2007**, 315, 808–810.

[76]   Morschbacker A., Macromol J. Bio-Ethanol Based Ethylene // *Polym. Sci. Rev.*, **2009**, 49, 79–84.

[77]   Thomas V. M., Kwong A. Ethanol as a lead replacement: Phasing out leaded gasoline in Africa // *Energy Policy*, **2001**, 29, 1133–1143.

[78]   Siwale L., Kristo´f L., Adam T., BereczkyA., Penninger A., Mbarawa M. Andrei K. Performance Characteristics of n-Butanol-Diesel Fuel Blend Fired in a Turbo-Charged Compression Ignition Engine // *J. Power Energy*, **2013**, 1, 77–83.

[79]   Lamy C., Rousseau S., Belgsir E. M., Coutanceau C., Le´gerJ.-M. Recent progress in the direct ethanol fuel cell: development of new platinum–tin electrocatalysts // *Electrochim. Acta*, **2004**, 49, 3901–3908.

[80]   Devarapalli M., Atiyeh H. K. A review of conversion processes for bioethanol production with a focus on syngas fermentation // *Biofuel Res. J.*, **2015**, 7, 268–280.

[81]   Bengelsdorf F. R. , Straub M., Du¨rre P. Bacterial synthesis gas (syngas) fermentation // *Environ. Technol.*, **2013**, 34, 1639–1651.

[82]   Lan E. I., Liao J. C. Microbial synthesis of n-butanol, isobutanol, and other higher alcohols from diverse resources // *Bioresour. Technol.*, **2013**, 135, 339–349.

[83]   Bai F. W., Anderson W. A., Moo-Young M., Ethanol fermentation technologies from sugar and starch feedstocks // *Biotechnol. Adv.*, **2008**, 26, 89–105.

[84]   Nakagawa Y., Tajima N., K. and Hirao. A theoretical study of catalytic hydration reactions of ethylene // *J. Comput. Chem.,* **2000**, 21, 1292–1304.

[85]   Xiao K, Zhenghong B. A. O, Xingzhen Q. I, Xinxing W., Liangshu Z., Kegong F., Minggui L., Yuhan S. Advances in bifunctional catalysis for higher alcohol synthesis from syngas // *Chinese Journal of Catalysis*, **2013**, 34, Issue 1, 116-129.

[86]   Brown R.C. Thermochemical Processing of Biomass: Conversion into Fuels, Chemicals and Power // Wiley: *Chichester*, UK, **2011**.

[87]   Suarez Paris, R., Lopez, L., Baronet, J., Pardo, F., Botoonet, M., Jaras, S. Catalytic conversion of biomass-derived synthesis gas to fuels // *J Catal*. **2015**, 27, 62–143.

[88]   Klerk D, A. Fischer–Tropsch Refining // Wiley-VCH Verlag GmbH & Co., **2011**.

[89]   Beretta A., Sun Q., Herman, R. G. Klier, K. Production of Methanol and Isobutyl Alcohol Mixtures over Double-Bed Cesium-Promoted $Cu/ZnO/Cr_2O_3$ and ZnO/Cr_2O_3 Catalysts // *Ind. Eng. Chem. Res.*, **1996**, 35, 1534-1542.

[90]   Nikulshin P.A., Salnikov V.A., Mozhaev A.V., Minaev P.P., Kogan V.M., Pimerzin A.A. Relationship between active phase morphology and catalytic properties of the carbon–alumina-supported Co(Ni)Mo catalysts in HDS and HYD reactions // *J. Catal*, **2014**, 309, 386-396.

[91]   Nogueira A., ZnaiguiaR., UzioD., AfanasievP., Berhault G. Curved nanostructures of unsupported and Al_2O_3-supported MoS_2 catalysts: Synthesis and HDS catalytic properties // *Appl*. Catal., A., **2012**, 429–430, 92-105.

[92]   Mills G. A. Summary of the Higher Alcohol synthesis workshop // B. R. Service Corporation, **1992**.

[93]   Smith K. J., Herman R. G., Klier, K. Kinetic modelling of higher alcohol synthesis over alkali-promoted Cu/ZnO and MoS_2 catalysts // *Chem. Eng. Sci.* **1990**, 45, 2639-2646.

[94]   Christensen J.M., Mortensen P.M., Trane R., Jensen P.A., Jensen A.D. Effects of H_2S and process conditions in the synthesis of mixed alcohols from syngas over alkali promoted cobalt-molybdenum sulfide // *Appl. Catal., A: Gen.* **2009**, 366, 29–43.

[95]   Feng M., Review of molybdenum catalysts for direct synthesis of mixed alcohols from synthesis gas // *Recent Patents Catal.,* **2012**, 1, 13–26.

[96]   Liu Z., Li X., Close M. l. R., Kugler E. L., Petersen J. L., Dadyburjor D. B.; Screening of alkali-promoted vapor-phase-synthesized molybdenum sulfide catalysts for the production of alcohols from synthesis gas // *Ind. Eng. Chem. Res.* **1997**, 36, 3085-3093.

[97]   Escobar J., Barrera M. C., Guti´errez A. W., Cort´es- Jacome M. A., Angeles-Ch´avez C., Toledo J. A., Sol´ıs- Casados D. A. Highly active P-doped sulfided NiMo/alumina HDS catalysts from Mo-blueby using saccharose as reducing agents precursor // *Appl. Catal., B*, **2018**, 237, 708–720.

[98]   Tluk H., Mondelli C., Ferré D. C., Stewart J., APérez-Ramírez. J. Status and prospects in higher alcohols synthesis from syngas //   *Chem. Soc. Rev.*, **2017**, 46, 1358-1426.

[99]   Li D., Yang C., Zhao N., Qi H., Li W., Sun Y., Zhong B. The performances of higher alcohol synthesis over nickel modified K_2CO_3/MoS_2 catalyst // *Fuel Process. Technol*, **2007**, 88, 125-127.

[100]   Deepak S. T., Delmon B. The role of group VIII metal promoter in MoS_2 and WS_2 hydrotreating catalysts: I. ESR studies of Co/Mo, Ni/Mo, and Ni/W catalysts // *Journal of Catalysis*, **1985**, 91, 2, 308-317.

[101]   Xi X, Zeng F, Cao H, Cannilla C, Bisswanger T, de Graaf S, et al. Enhanced C_{3+} alcohol synthesis from syngas using K-CoMoS$_x$ catalysts: effect of the Co-Mo ratio on catalyst performance // *Appl Catal B-Environ.,* **2020**, 272, 118950.

[102]   Krebs E., Silvi B., Raybaud P. New developments in sulfide catalysis: Linking industrial needs to fundamental challenges // *Catal. Today*, **2008**, 130, 160–169.

[103]   Stewart A., Pérez-Ramírez J. Status and prospects in higher alcohols synthesis from syngas // *Chem. Soc. Rev*. **2017**, 46, 1358–1426.

[104]   Rana M. S., Sámano V., Ancheyta J., Diaz J. A. I. A review of recent advances on process technologies for upgrading of heavy oils and residua // *Fuel*, **2007**, 86, 1216–1231.

[105]   Babich I.V., Moulijn J.A. Science and technology of novel processes for deep desulfurization of oil refinery streams: a review // *Fuel*, *2003*, 82, 607 – 631.

[106]   Salvi B.L., Subramanian K.A., Panwar N.L. Alternative fuels for transportation vehicles: a technical review, Renew. Sustain // *Energy Rev*., **2013**, 25, 404–419.

[107]   Brunet S., Mey D., Pérot G., Bouchy C., Diehl F. On the hydrodesulfurization of FCC gasoline: a review // *Appl. Catal. A Gen*., **2005**, 278, 143–172.

[108]   Samokhvalov A., Tatarchuk B.J. Review of experimental characterization of active sites and determination of molecular mechanisms of adsorption, desorption and regeneration of the deep and ultra-deep desulfurization sorbents for liquid fuels // *Rev.*, **2010**, 52, 381– 410.

[109]   Chianelli R.R., Berhault G., Torres B. Unsupported transition metal sulfide catalysts: 100 years of science and application // *Catal. Today*, **2009** 147, 275–286.

[110]   Li D. Crucial technologies supporting future development of petroleum refining industry // *Chin. J. Catal.*, **2013**, 34, 2013, 48–60.

[111]   Stanislaus A., Marafi A., Rana M.S., Recent advances in the science and technology of ultra-low sulfur diesel (ULSD) production // *Catal. Today*, *2010*, 153, 1–68.

[112]   Luk H.T., Mondelli C., Ferré D.C., Stewart J.A., Pérez-Ramírez J.. Status and prospects in higher alcohols synthesis from syngas // *Chem. Soc. Rev.*, **2017**, 46, 1243–1636.

[113]   Dorokhov V. S., Kamorin M. A., Rozhdestvenskaya N. N., Kogan V.M. Synthesis and conversion of alcohols over modified transition metal sulphides // *Comptes Rendus Chim.*, **2016**, 19, 1184–1193.

[114]   Santos V.P., van der Linden B., Chojecki A., Budroni G., Corthals S., ShibataH., Meima G.R., Kapteijn F., Makkee M., Gascon J. Mechanistic insight into the synthesis of higher alcohols from syngas: the role of K promotion on MoS2 catalysts // *ACS Catal.,* **2013**, 3, 1634–1637.

[115]   Andersen A., Kathmann S. M., Lilga M. A., Albrecht K. O., Hallen R. T., Mei D. Adsorption of potassium on MoS_2 (100) surface: a first-principles investigation // *J. Phys. Chem. C,* **2011**, 115, 9025–9040.

[116]   Chen Y.-Y., Zhao X., Wen X.-D., Shi X.-R., Dong M., Wang J., et al. Mechanistic aspect of ethanol synthesis from methanol under CO hydrogenation condition on MoSx cluster model catalysts // *J. Mol. Catal. A: Chem.*, **2010**, 329, 77–85.

[117]   Chen Y.-Y., Dong M., QinZ., Wen X.-D., Fan W., Wang J. A DFT study on the adsorption and dissociation of methanol over MoS_2 surface // *J. Mol. Catal. A:Chem.*, **2011**, 338, 44–50.

[118]   Shi X.-R., Jiao H., HermannK., WangJ. CO hydrogenation reaction on sulfided molybdenum catalysts // *J. Mol. Catal. A: Chem.*, **2009**, 312, 7–17.

[119]   Santiesteban J.G., Bogdan C.E., Herman R.G., KlierK.Mechanism of C1–C4 alcohol synthesis over alkali/MoS_2 and alkali/Co/MoS_2 catalysts // 9th Int. Congr. Catal., Calgary, **1988**, 561–568.

[120]   Fang K., Li D., Lin M., Xiang M., Wei W., Sun Y. A short review of heterogeneous catalytic process for mixed alcohols synthesis via syngas // *Catal. Today*, **2009**, 147,133–138.

[121]   Lee S., Kim S., Lee K. H., Nam I. -S., Chung J. S., Kim Y. G., et al., Role of alkali promoters in K/MoS2 catalysts for CO–H$_2$ reactions // *Appl. Catal.*, *A: Gen*., **1994**, 110,11–25.

[122]   Andersen A., Kathmann S. M., Lilga M. A., Albrecht K.O., Hallen R.T., Mei D. First principles characterization of potassium intercalation in hexagonal 2H-MoS$_2$ // *J. Phys. Chem. C*, **2012**, 116, 1826–1832.

[123]   Benavente E., Santa Ana M. A., Mendizabal F., Gonzalez G. Intercalation chemistry of molybdenum disulfide // *Coord. Chem. Rev.,* **2002**, 224, 87–109.

[124]   Wypych F., WeberT., Prins R. Scanning tunneling microscopic investigation of 1T-MoS$_2$ // *Chem. Mater*., **1998**, 10, 723–727.

[125]   Andersen A., Kathmann S. M., Lilga M. A., Albrecht K. O., Hallen R. T., Mei D. Effects of potassium doping on CO hydrogenation over MoS2 catalysts: a firstprinciples investigation // *Catal. Commun.*, **2014**, 52, 92–9.

[126]   Filikov A. V, Myasoedov N. F. Hydrogen spillover and the rate of heterogeneous catalytic hydrogenation. Quantitative model // *J Phys Chem.* **1986**, 90, 21, 4915–4916

[127]   Bazula P. A, Lu A. H, Nitz J. J, Schüth F. Surface and pore structure modification of ordered mesoporous carbons via a chemical oxidation approach // *Micro & Meso Mater.,* **2008**, 108(1–3), 266–275.

[128]   Lazaro M. J, Calvillo L, Bordeje E. G, Moliner R., Juan R., Ruiz C.R. Functionalization of ordered mesoporous carbons synthesized with SBA–15 silica as template // *Micropor Mesoporous Mat.,* **2007**, 103(1–3), 158–165.

[129]   Serp P, Machado B. Carbon Nano materials for Catalysis, in Nano structured Carbon Materials for Catalysis // *Catalysis Series, RSC*, **2015**; 1–45.

[130]   Otake Y, Jenkins R. G. Characterization of oxygen–containing surface complexes created on a microporous carbon by air and nitric acid treatment // *Carbon,* **1993**, 31, 1, 109–121.

[131]   Marsh H., Rodriguez-Reinoso, F. Activated Carbon // Elsevier: Amsterdam, The Netherlands, **2006**; pp. 1–554.

[132]   Boahene P. E, Sammynaiken R, Dalai A. K. Syngas conversion to higher alcohols: application of novel K-promoted coRhMo catalysts supported over carbon nanohorns and its by-products // *Int J Petrochem Sci Eng.* **2017**, 2, 1, 1–10.

[133]   Vissers J. P. R., Mercx F. P. M., Bouwens S. M. A. M., de Beer V. H., Prins R. Carbon-covered alumina as a support for sulfide catalysts // *J. Catal.* **1988,** 114, 291.

[134]   Butterworth S.L., Scaroni A.W. Carbon-coated alumina as a catalyst support: 1. Preparation via liquid and vapor phase pyrolysis // *Appl. Catal.* **1985**, 16, 375.

[135]   Cui F., Li G., Li X., Lu M., Li M. Enhancement of hydrodesulfurization of 4,6-dimethyldibenzothiophene catalyzed by CoMo catalysts supported on carbon-covered γ-Al_2O_3 // *Catal. Sci. Technol.*, 2015, 5, 549-555.

[136]   Shahil Otake, K. M. F., Balandin A. A. Graphene–Multilayer Graphene Nanocomposites as Highly Efficient Thermal Interface Materials // *Nano Lett.,* **2012**, 12, 861-867.

[137]   Yu A., Ramesh P., Itkis M. E., Bekyarova E., Haddon R.C. Graphite Nanoplatelet−Epoxy Composite Thermal Interface Materials // *J. Phys. Chem. C.,* **2007**, 111, 7565-7569.

[138]   Yang S.-Y., Lin W.-N., Huang Y.-L., Tien H.-W., Wang J.-Y., Ma C.-C.M., Li S.-M., Wang Y.-S. Synergetic effects of graphene platelets and carbon nanotubes on the mechanical and thermal properties of epoxy composites // *Carbon*, *2011*, 49, 793-803.

[139]   Pietrzyk B, Miszczak S, Sun Y, Szyman´ski M. Al2O3 + Graphene Low-Friction Composite Coatings Prepared By Sol–Gel Method // *Coatings* **2020**, 10, 858:2-15.

[140]   Brinker, C. J., Scherer, G. W. Sol.-Gel Science: The Physics and Chemistry of Sol.-Gel Processing // Academic Press Inc.: San Diego, CA, USA, **1990**; ISBN 978-0-12-134970-7. 51.

[141]   Levy D., Zayat M. The Sol.-Gel Handbook: Synthesis, Characterization and Applications // 1st ed.; Wiley-VCH Verlag GmbH & Co. KGaA: Weindheim, Germany, **2015**; ISBN 978-3-527-67084-0. 52.

[142]   Brinker C. J., Hurd A. J., Schunk P. R., Frye, G. C., Ashley C. S., Review of Sol-Gel Thin-Film Formation // *Journal of Non-Crystalline Solids*, **1992**, 147, 424-436.

[143]   Trusova E. A., Kotsareva K. V., Kirichenko A. N., Abramchuk S. S., Perezhogin I. A. Sonochemical Preparation and Subsequent Fixation of Oxygen-Free Graphene Sheets at N,N-Dimethyloctylamine-Aqua Boundary // Adv. *Mater. Sci. Eng.*, **2018**, 2018, 6026437.

[144]   Mukhin V. M., Klushin V. N. Production and application of carbon adsopbents. Text book. Editor N.F. Zhodyakina // Russian Mendeleev University of Chemical Technology of Russia, Moscow, **2012** (in Russian)].

[145]   Sing K. S. W., Moscou L.; Pierotti R. A., Rouquerol J., Siemieniewska T. Reporting Physisorption Data for Gas/Solid Systems with Special Reference to the Determination of Surface Area and Porosity // *Pure Appl. Chem.*, **1985**, 57, 603–619.

[146]   Claure M. T, Chai S. H, Dai S, Unocic K. A, Alamgir F. M, Agrawal P. K, Jones C. W. Tuning of higher alcohol selectivity and productivity in CO hydrogenation reactions over K/MoS$_2$ domains supported on mesoporous activated carbon and mixed MgAl oxide // *J Catal., 2015,* 97, 324-88.

[147]   Trusova E. A, Kirichenko A. N, Afzal A. M, Perezhogin I. A., Konovalov A. A,. Abramchuk S. S, Ashmarin A. A, Alpatov A. V. Graphene-alumina nanostructured hybrid: synthesis with use dodecylamine and physicochemical properties, Fullerenes // *Nanotubes and Carbon Nanostructures*, **2021**, 29: 6, 431-441.

[148]   Kobayashi Y., Ishizaka T., Kurokawa Y. Preparation of alumina films by the sol-gel method // *J. Mater. Sci.* **2005**, 40, 263–283.

[149]   Niannian Q., Xiaoliang M., Lu Z., Kegong F. Effect of K-CoMoS2 Catalyst Structures on the Catalytic Performance of Higher Alcohols Synthesis via CO Hydrogenation // *Catalysts*, **2020**, 10, 151-163.

[150]   Wang N., Hu R., Li J., Bai F., Zhang Y., Su H., Gu X. Insight into the promotion mechanism of K and Ni in sulfide molybdenum-based catalysts for higher alcohols synthesis from syngas // *Catalysis Communication*, **2017**, 91, 57-61.

[151]   Klimenko I. V., Lobanov A. V., Trusova E. A., Schegolikhin A. N., New Hybrid Oxygen-Free Graphene and Phthalocyanine Aluiminum Structures: Preparation and aphysicochemical Properties // *Russ, J. Phys. Chem. B, 2019*, 13, 964–968.

[152]   Gazzi A., Fusco L., Khan A., Bedognetti D., Zavan B., Vitale F., Yilmazer A., Delogu L. G. Photodynamic Therapy Based on Graphene and MXene in Cancer Theranostics // *Front. Bioeng. Biotechnol*. **2019**, 7, 295.

[153]   Escobar J., Barrera M. C., Guti´errez A. W., Cort´es- Jacome M. A., Angeles-Ch´avez C., Toledo J. A., Sol´ıs- Casados D. A. Highly active P-doped sulfided NiMo/alumina HDS catalysts from Mo-blueby using saccharose as reducing agents precursor // *Appl. Catal., B,* **2018**, 237, 708–720.

[154]   Bergthorsona J. M., Thomsonb M. J. A review of the combustion and emissions properties of advanced transportation biofuels and their impact on existing and future engines // *Renewable and Sustainable Energy Reviews,* **2015**, 42, 1393–1417.

[155]   Magnusson R. and Nilsson C. The influence of oxygenated fuels on emissions of aldehydes and ketones from a two-stroke spark ignition engine // *Fuel*, **2011**, 90, 1145–1154.

[156]   Xu Y., Li P., Yuan S., Sui B., Lai W., Yi X., and Fang W. Sacrificial carbonaceous coating over alumina supported Ni–MoS$_2$ catalyst for hydrodesulfurization // *RSC Adv*., **2019**, 9, 11951–11959.

[157]   Daage M., Chianelli M. R. R. Structure-Function Relations in Molybdenum Sulfide Catalysts: The "Rim-Edge" Model // *J. Catal*., **1994** 149, 414–427.

[158]   Morrill M. R, Thao N. T, Shou H, Davis R. J, Barton D. J.; Ferrari D.; Agrawal PK.; Jones CW. Origins of unusual alcohol selectivities over mixed MgAl oxide supported K/MoS2 catalysts for higher alcohol synthesis from syngas // *ACS Catal*, **2016**, 3, 1665–1675.

[159]   Lee J. J., Han S., Kim H., Koh J. H., Hyeon T., Moon S. H. Performance of CoMoS catalysts supported on nanoporous carbon in the hydrodesulfurization of dibenzothiophene and 4,6-dimethyldibenzothiophene // *Catal Today*, **2003**, 194, 86-141.

[160]   Xiaoquan Z., Xiaoyu L., Xiaobin F., Xintai S. Fabrication of flower-like MoS2/TiO2 hybrid as an anode material for lithium ion batteries. *Royal Society of Chemistry* // **2017**, 7, 38119–38124.

[161]   Taheraslani, Mohammadreza, and Han Gardeniers. High-Resolution SEM and EDX Characterization of Deposits Formed by CH$_4$+Ar DBD Plasma Processing in a Packed Bed Reactor. Nanomaterials, 2019, 9, 4 589.

[162]   Reed, S.J.B. Electron Microprobe Analysis // 2nd ed. Cambridge University Press, *Cambridge*. **1993.**

[163]   Luan, X.; Yong, J.; Dai, X.; Zhang, X.; Qiao, H.; Yang, Y.; Huang, X. Tungsten-doped molybdenum sulfide with dominant double-layer structure on mixed MgAl oxide for higher alcohol synthesis in CO hydrogenation // *Ind. Eng. Chem. Res.* **2018**, 57, 10170–10179.

[164]   Kogan V. M., Nikulshin P. A., Rozhdestvenskaya N. N. Evolution and interlayer dynamics of active sites of promoted transition metal sulfide catalysts under hydrodesulfurization conditions // *Fuel*, **2012**, 100, 2–16.

[165]   Ishutenko D., Anashkin Y., Nikulshin P. The effect of carrier in K-CoMoS-supported catalysts for hydro-upgrading of model FCC gasoline // *Appl. Catal., B*. **2019**, 259, 118041.